Multi-Wavelength Distributed Feedback Lasers

by

Andrew M. Sarangan

A thesis
presented to the University of Waterloo
in fulfilment of the
thesis requirement for the degree of
Doctor of Philosophy
in
Electrical Engineering

Waterloo, Ontario, Canada, 1996

The University of Waterloo requires the signatures of all persons using or photocopying this thesis. Please sign below, and give address and date.

Abstract

Wavelength Division Multiplexing (WDM) can be an attractive alternative over Time Division Multiplexing (TDM) in fiber communications both within the inter-office links as well as in the subscriber network. As a result, components capable of multi-wavelength operation have become increasingly important. For the realization of multi-wavelength laser sources, the arrayed approach has been particularly attractive. Since the Distributed Feedback (DFB) laser is the laser diode of choice for long-haul high-speed fiber links, DFB laser arrays have received much attention in the literature recently. Nevertheless, these components have been slow to materialize due to the complexity in their design and fabrication. Hence, the theme of this thesis is to demonstrate practical and simple methods of wavelength control in Ridge Waveguide DFB laser arrays via modeling, analysis and experimental demonstration.

In the first part of this thesis, a quasi-three-dimensional model of the DFB laser is developed. In addition to the longitudinal description, a two-dimensional transverse description of the laser has been incorporated. This enables one to carry out a detailed study of the transverse ridge waveguide structure identifying its effects on the lasing performance.

In the second part of this thesis, DFB laser arrays capable of emission at multiple wavelengths are studied and experimentally demonstrated. The techniques demonstrated here are simple, inexpensive and practical. A uniform holographic exposure is used for all the lasers in the array which greatly simplifies the fabrication process. Only the final lithographic step is used for defining the wavelength. Wavelength tuning range as high as 8nm is demonstrated for the first time using ridge width and ridge tilt control. Important transverse effects such as tilt-induced

transverse periodicity and their role in transverse mode selection have been identified. Other salient features such as transverse mode stability in multi-mode ridge waveguide structures and their effect on tuning range have been demonstrated.

Acknowledgements

I will forever be in debt to my supervisor Professor Weiping Huang for the enthusiastic support and constant encouragement he provided throughout my graduate career. He has a unique gift for motivating students and for keeping their morale and spirits high. He has shown me many times how complex physical effects can be stripped of their obscuring details by simple intuitive reasoning. This style of reasoning has made a strong impression on me which I will carry with me for many years to come. It is indeed a challenge to maintain the high standards he has demonstrated through his supervision and in his own work.

Much of this work would not have been possible without the assistance from Dr. Chenglin Xu. His help in all aspects of electro-magnetic computation goes a long way back to my Masters degree. It was his software that first helped me understand the rudiments of BPM and FDTD. More recently, his help with the 2D Mode Solver has been extremely useful for me, and is used extensively in this thesis.

I am also greatful for Professor Xun Li for his expert counseling in all aspects of DFB lasers. He has always surprised me with the amount of technical knowledge he carries in him, a fraction of which I always tried to down-load every time I met with him.

I would also like to acknowledge the technical and social interactions I have had with my colleagues in the Waterloo Photonics Group. The interaction with Fred Ma, Rob Singh and Ali Shams will be fondly remembered.

The collaboration with Nortel Technology (Bell-Northern Research) has been a valuable part of this research work. I am thankful not only for their financial support, but also for the in-kind support on fabrication, characterization and technical counseling. Dr. Toshihiko Makino, my manager at Nortel, has spent many hours

with me patiently explaining to me the detailed aspects of DFB lasers. He is an immense store-house of knowledge and has never ceased to impress me. Dr. Guoping Li was my co-supervisor at Nortel at the early stages of this project. It was his enthusiasm which brought this whole project into being. Without his assistance, the experimental aspect of this work would not even exist. He did all the laser fabrication work and helped me understand the basics of laser processing technology. When he left for SDL in January 1996, his absence was greatly felt. Furthermore, the interaction with other scientists and engineers at Nortel has greatly enhanced my understanding of real world engineering. The discussions I have had with Dr. Chi Wu, Dave Adams, Dr. Jin Hong, Dr. Greg Pakulski, Bruce Richardson, Dr. Gary Mak and Dr. Jack Evans have been extremely valuable.

I would also like to acknowledge the financial support from the Telecommunications Research Institute of Ontario. TRIO has given me a unique opportunity to meet and interact with several industrial scientists through annual meetings and retreats. It was TRIO's Research Internship Program which first brought me to realize how University research can be successfully integrated with Industrial interests. This experience has reinstated my confidence in academic research.

I would also like to acknowledge the valuable input I received from my other Ph.D committee members. Prof. Sujeet Chaudhuri, Prof. Marek Wartak, Prof. Arokia Nathan and my external examiner Prof. Peter Smith have all provided valuable guidance in completing this thesis.

Finally, I am greatlful to my father and sister who have been supportive and tolerant of my extended absence from home during my research. Last, but not least, the patience, support and encouragement from my future wife, Nancy, has as much to do with the success of my work as anyone else's.

Contents

1 Introduction **1**

1.1 A Brief Historical Introduction 1

1.2 Towards Higher Bit Rates 2

1.3 Semiconductor Lasers for Wavelength Division Multiplexing 3

1.4 Review of DFB Laser Models 4

1.5 Review of WDM Laser Arrays 6

1.6 Review of Ridge Waveguide DFB Laser Design and Process Flow . 7

1.7 Problem Statement 10

1.8 Original Contributions Claimed in this Thesis 10

1.9 Outline of the Thesis 11

2 Distributed Feedback Lasers: Longitudinal Model **13**

2.1 Introduction 13

2.2 Coupled Wave Theory for Distributed Feedback Structures 14

2.2.1 Unperturbed Solution 14

2.2.2 Perturbed Solution 15
2.2.3 Corrugated Waveguide 17
2.2.4 Coupled Wave Equations 18
2.2.5 Coupled Two-Wave Solution 19
2.2.6 Reflection and Transmission Coefficients in the DFB Structure 20
2.3 Multi-Section Distributed Feedback Laser Model 22
2.3.1 Reflections Through Multi-Sections 22
2.3.2 Feedback Model 24
2.3.3 Transmission Through Subsections 27
2.3.4 Facet Output Power 29
2.4 Material Interaction Models 31
2.4.1 Gain Model 31
2.4.2 Line Width Enhancement Factor 32
2.4.3 Gain Saturation 32
2.5 Method of Solution 33
2.5.1 Formulation 33
2.5.2 Numerical Solution Method 35
2.6 Demonstration of the Model 36
2.6.1 Truncated Quantum Well Gain-Coupled DFB Lasers 37
2.6.2 Mode Selection due to Spatial-Hole Burning in Index-Coupled DFB Lasers 46
2.7 Conclusions 49

3 Distributed Feedback Lasers: Transverse Model **50**

3.1 Introduction 50

3.2 Two-Dimensional Optical Model 50

3.3 Lateral Carrier Model 52

3.3.1 Carrier Transport in the Upper GRINSCH Region 54

3.3.2 Carrier Transport in the Active Region 57

3.3.3 Interaction of Transverse Gain and Optical Profiles 58

3.4 Lateral Leakage Current Model 62

3.4.1 Threshold Current and GRINSCH Layer Properties 63

3.5 Conclusions 63

4 Varying Ridge Width Laser Array **66**

4.1 Introduction 66

4.2 Device Description 67

4.3 Single Transverse Mode Operation 69

4.4 Lasing Wavelength Shift with Ridge Width 75

4.5 Simultaneous Multi-Wavelength Demonstration of the Laser Array . 77

4.6 Conclusions 80

5 Varying Ridge Tilt Laser Array **83**

5.1 Introduction 83

5.2 Coupling Coefficients with a Waveguide Tilt 85

5.3 Single Transverse Mode Tilted Ridge DFB Lasers 91

5.3.1 Thermal Effects 96

5.4 Multi Transverse Mode Tilted Ridge DFB Lasers 99

5.5 Combined Effect of Ridge Tilt and Ridge Width 102

5.6 Conclusions 112

6 Conclusions and Recommendations **114**

6.1 Conclusions 114

6.2 Recommendations for Future Research 115

A DFB Reflection and Transmission Coefficients **117**

A.1 Formulation 117

A.2 Right Reflection Coefficient 118

A.3 Left Reflection Coefficient 118

A.4 Right Transmission Coefficient 119

A.5 Left Transmission Coefficient 119

B Derivation of Photon Rate Equation **121**

Bibliography **123**

List of Figures

1.1 Summary of DFB Laser Modeling Literature 5

1.2 Ridge Waveguide DFB Laser Structure 8

2.1 Reflection and Transmission in a DFB Structure 21

2.2 Laser Cavity Modeled as Several Stacked Subsections 23

2.3 Feedback Model of the DFB Laser 25

2.4 Photon Transmission Between Subsections 28

2.5 Stimulated and Spontaneous Emissions in Each Subsection 30

2.6 Diagrammatic Representation of the Solution Method 34

2.7 Periodically Truncated Quantum Wells Structure 38

2.8 Lasing Spectrum of the Gain-Coupled Laser 39

2.9 Wavelength as a Function of Injection Current for the Gain-Coupled Laser 40

2.10 Spatial Hole Burning of I_{nst} in the Gain-Coupled Laser 41

2.11 L-I Curve of the Gain-Coupled Laser 42

2.12 Optical Power Flow and Gain Distribution in a DFB Cavity 45

2.13 Effect of Spatial Hole Burning on the Lasing Spectrum of Index-Coupled DFB with $\kappa L \approx 2.6$ 47

2.14 Effect of Spatial Hole Burning on the Effective Index of Index-Coupled DFB with $\kappa L \approx 2.6$ 48

3.1 Lateral Carrier Transport Model for the Ridge Waveguide DFB Laser 53

3.2 Lateral Injection/Carrier/Gain/Optical Profiles 60

3.3 Carrier, Gain and Optical Profiles at Threshold for Different Ridge Widths 61

3.4 Threshold Current vs GRINSCH Layer Resistance & Diffusion Coefficient for Different Ridge Widths 64

4.1 Layer Structure of the Index-Coupled DFB Laser 68

4.2 Chip Photograph of the 16-element Varying Ridge Width DFB Laser Array 70

4.3 Calculated Effective Indices in the Varying Ridge Width DFB Laser Array 71

4.4 Calculated Coupling Coefficients in the Varying Ridge Width DFB Laser Array 73

4.5 Calculated Threshold Gain for the Varying Ridge Width DFB Laser Array 74

4.6 Calculated and Measured Wavelength vs Ridge Width 76

4.7 Spectrum of the 4.9μm Wide Ridge Laser Under Small-Signal Modulation 78

4.8 WDM Experimental Setup 79

4.9 Simultaneous Operation of Four Wavelengths into a Single Fiber . . 81

5.1 Tilted Waveguide with Respect to the Gratings 86

5.2 Contour Plot of the 2D Optical Mode and the Tilt Induced Transverse Gratings 88

5.3 Layer Structure of the Loss-Coupled DFB Laser 90

5.4 Calculated $\Re\{\kappa_{mn}\}$ and Threshold Gain vs Tilt Angle for 1.2μm Wide Ridge 92

5.5 Calculated and Measured Wavelength vs Tilt Angle for 1.2μm Wide Ridge 93

5.6 Measured Lasing Spectra at 80mA for the 1.2μm Wide Tilted Structures 95

5.7 Calculated and Measured Threshold Current for the 1.2μm Wide Laser vs Tilt Angle 97

5.8 Contour Plot of the First Order Mode in the 3.0μm Wide Laser . . 100

5.9 Calculated κ_{mm} vs Tilt Angle for the 3.0μm Wide Laser 101

5.10 Calculated Threshold Gain with Tilt Angle for the 3.0μm Wide Laser 103

5.11 Simulated Above Threshold Lasing Spectra for 0° and 8° Tilt Angles for the 3.0μm Wide Laser 104

5.12 Cumulative Lasing Wavelength as a Function of Tilt Angle for the 3.0μm Wide Laser 105

5.13 Calculated κ_{mn} in the Combined Ridge Width/Tilt Angle Array . . 107

5.14 Measured Lasing Spectra of the Combined Ridge Width/Tilt Angle Array 109

5.15 Calculated and Measured Wavelength in the Combined Ridge Width/Tilt Angle Array 110

5.16 Measured Near Field Profiles Demonstrating the Transverse Mode Jumps in the Combined Ridge Width/Tilt Angle Array 111

List of Symbols

$\mathbf{E}$	electric field
c	speed of light
σ	conductivity
η	refractive index
μ_o	permeability
$\mathbf{J}_s$	spontaneous emission current density
β_n	propagation constant of n-th transverse mode
$\eta_{eff,n}$	effective index of the n-th transverse mode
a_n	amplitude of the n-th transverse mode
ω	angular frequency of light
k	wave-vector of light
λ	wavelength of light
κ_{mn}	coupling coefficient between the n-th and m-th transverse mode
ζ_m	coupling of spontaneous emission into the m-th transvers mode
$\hbar$	Plank's constant divided by 2π
P_ω	Photon flux density per angular frequency
K	Grating wave-vector
$\tilde{\kappa}_{mn}$	κ_{mn} for a grated structure
$\tilde{\sigma}_{mn}$	Net ioss or gain in a waveguide
θ_{mn}	Phase of the complex coupling coefficient $\tilde{\kappa}_{mn}$
δ	Detuning from the central bragg frequency
t,r	Transmission and reflection coefficients
n	Electron carrier density
n_{tr}	Transparent electron carrier density

a	Gain coefficient
α	Linewidth enhancement factor
χ_p	Reactivity of the medium
ϵ	Gain compression factor (also used for permittivity)
v_g	Group velocity
I_{nst}	Non-stimulated portion of the injected current
I_{st}	Stimualted portion of the injected current
I_{nr}	Non-radiative portion of the injected current
I_{sp}	Spontaneous portion of the injected current
w	Ridge Width
d_0	GRINSCH layer thickness
d_1	Active layer thickness
ρ_x	Resistivity of the GRINSCH region
J_s	Diode saturation current
V_t	Thermal voltage
A,B,C	Linear, Bimolecular and Auger coefficients
μ_p	Hole mobility
μ_n	Electron mobility
N_A	Acceptor doping
D	Ambipolar diffusion constant
R_s	Diode series resistance
R_T	Thermal resistance
g_{th}	Threshold gain
θ	Tilt angle (in tilted ridge lasers)

Chapter 1

Introduction

1.1 A Brief Historical Introduction

The use of light to transmit information is not a new idea. Alexander Graham Bell invented the "photophone" and filed a patent for it in 1880. This was an instrument that used reflected sunlight to transmit information. Nevertheless, it was the wired telephone that brought great fame for Graham Bell, not the photophone. The forces of technology and economics of that day were in favour of the wired telephone set, and the idea of using optical signals was put to rest until the mid-1900.

The revolutionary developments in science and technology that took place during the post-war era rekindled the interest in optical communications. The invention of the *laser* followed later by the *glass fiber* were two important milestones in the development of photonics. The invention of the laser source made it possible to have a carrier frequency in the tera-hertz frequency range. The invention of glass fibers made it possible to *guide* light within a flexible cable. However even the best fiber of the 1960's had an attenuation of 1dB/m. The breakthrough in fiber technology

occurred at Corning Glass Works in 1970 with the demonstration of the low-loss single-mode silica glass fiber. This had an attenuation of just 20dB/km at the visible wavelength of 632nm. Subsequent development in the technology improved the losses even further. Today it stands at 0.2dB/km at 1.55μm wavelength.

The parallel development in semiconductor electronics also played a key role in photonics. Not only did it lead to the electronic Integrated Circuit (IC), but also to the semiconductor laser. Without semiconductor lasers it is doubtful if optical communications would have evolved to where it is today. Semiconductor lasers provided a cheap, compact and efficient source of light. One important feature that sets it apart from other laser sources was the fact that it could be *directly modulated* at extremely high speeds.

1.2 Towards Higher Bit Rates

Throughout the evolution of fiber transmission systems the trend has been towards higher and higher modulation speeds. The first fiber field-trial conducted by American Telephone and Telegraph (AT&T) in 1977 was at the DS-3 rate of 45 Mbits/s at 1.3μm [1]. The first long distance link was installed in 1980 using multi mode fibers at the DS-4 rate of 270 Mbits/s. A new synchronous multiplexing plan called SONET was later proposed. This was based on a 51.84 Mbits/s signal known as OC-1, and has since been accepted as the international standard [2]. Since the early 1990's the OC-48 system at a bit rate of 2.48 Gbits/s has been commercially available. The OC-192 operating at 10 Gbits/s is presently being actively deployed as the new standard for communication applications.

The wavelength of choice for telecommunications is around 1.3μm and 1.55μm. In the conventional fiber, these correspond to the low-dispersion and the low-loss

windows respectively. The trade-offs between dispersion and loss has always been a point of debate in deciding which wavelength to choose. Although historically the preference has been towards 1.3μm, due to the recent developments in Erbium Doped Fiber Amplifier (EDFA) and Dispersion Compensation Techniques, 1.55μm has emerged as the wavelength of choice.

It is questionable if the speed can be increased beyond 10 Gbits/s, both from a physical and also from a cost stand point. The inherent speed limitation of the laser itself poses one limit, while the expensive and extensive support circuitry required to drive the laser at such high speeds poses another limit. In order to better utilize the fiber and EDFA bandwidths, the technique of Wavelength Division Multiplexing (WDM) has been proposed [3]. This is essentially a multi-channel system with each optical channel separated from one another in the wavelength domain (or equivalently, in the optical frequency domain) and each channel carrying their maximum signal capacity simultaneously. The concept of multi-wavelength systems itself is not all that new. It has been studied extensively in the past twenty years. However, due to the lack of reliable components for transmitters and receivers, commercial application of multi-wavelength systems has not yet emerged.

1.3 Semiconductor Lasers for Wavelength Division Multiplexing

From what has been proposed in the literature for the realization of practical multi-wavelength lasers one can identify two major streams of thought. One approach is to have a set of fully tunable lasers which are capable of fast and dynamic tuning from one channel to another. The second approach is to have an array of lasers each

operating at a fixed but different wavelength. Although the former approach is more appealing at first, lasers which exhibit fast tuning and yet show stable behaviour are difficult to realize in practice. As a result, the second option has been receiving a lot of attention lately. It can be argued that a comb of wavelengths operating at predefined wavelength spacings can be functionally similar to a discretely tunable laser. Further, the fabrication technology of laser arrays is not a fundamental departure from solitary laser technology, but rather an *extension* from it. This is always a favoured characteristic in any emerging technology.

1.4 Review of DFB Laser Models

Distributed Feedback (DFB) lasers are arguably one of the most complicated optoelectronic devices to model. They cover a broad range of areas such as quantum processes, semiconductor carrier transport effects, the interaction of the optical fields with passive and active gratings and optical wave guiding effects. As a result, it is futile to speak of an all-inclusive comprehensive model of the DFB laser. Different models, depending on the author's areas of expertise, tend to describe different features of the DFB laser to different degrees of detail.

The main features that set the DFB laser apart from the conventional Fabry-Perot laser are the *spectral selectivity* and the *spatial-hole burning* effect. The spectral selectivity is provided by the gratings etched along the length of the device. Spatial hole burning refers to the longitudinal variation in carrier density that arises as a result of the longitudinal variation in optical intensity. Most of the modeling efforts in DFB lasers are centered around correctly and efficiently describing these two effects.

The original paper suggesting lasing action in corrugated structures was by

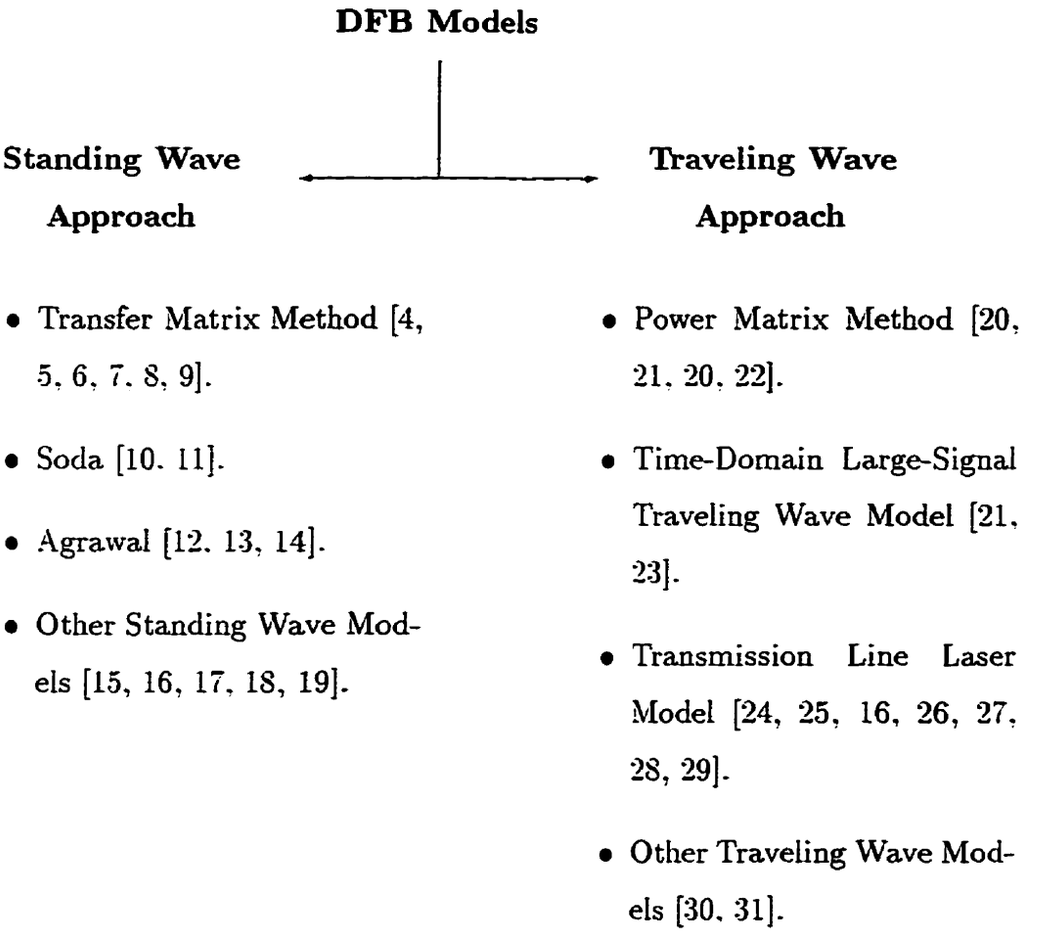

Figure 1.1: Summary DFB laser models and references.

Kogelnik and Shank in 1971 [32]. Although monumental, it only presents a linear model of the laser and does not consider important DFB effects such as spatial hole burning. In later years several approaches to modeling DFB lasers have emerged.

Basically, two approaches to modeling DFB lasers have emerged: the Standing Wave Approach and the Traveling Wave approach. In the Standing Wave Approach the fields inside the cavity are assumed to be at steady state, having gone through many round-trips in the cavity. This leads to the inherent requirement that the modulation time should always less than the round-trip time. In the Traveling Wave approach this assumption is not made, and all of the transient fields are computed. The different contributions to the area of DFB laser modeling is summarized on figure 1.1.

1.5 Review of WDM Laser Arrays

Several techniques have been reported in the literature for the control of wavelength in DFB laser arrays. As early as 1977, laser arrays using stepped holographic exposure to control the grating pitch have been reported [33].

At present, the most popular method of wavelength control is to use direct E-beam writing to create the gratings [34, 35]. This method allows enough flexibility to arbitrarily alter the grating pitch. However, the E-beam spot size variation as well as the excessive time taken to write a single wafer makes this method unsuitable for large scale processing. As a result, other simpler techniques for wavelength control have been sought.

Another new and attractive technique is the use of printed phase-mask gratings. A phase-mask of arbitrary gratings is generated on silica using E-beam writing.

These gratings are then reproduced onto a wafer using contact printing [36, 37, 38].

Alternatively, selective area epitaxy can be used to control the lateral variation in the epitaxial layer composition. By controlling the material composition from one laser to the next the laser wavelength can also be controlled [39, 40, 41]. Other techniques such as synchronous orbital radiation [42], shadow mask growth [43], quantum-well intermixing [44] and multi-stripe array gratings [45, 46] have also been reported. Recently, the use of thermal fine-tuning to control the wavelength has also been demonstrated [47, 48].

The use of tilting the ridge with respect to the gratings to produce a longer effective grating pitch has also been suggested [49], but a detailed understanding of this technique was still lacking until the findings of this thesis were published. In addition, the technique of varying the ridge width to control the modal index has also been mentioned but detailed studies or practical demonstration of this technique have not been reported until the results of this thesis were published.

1.6 Review of Ridge Waveguide DFB Laser Design and Process Flow

In this section a brief outline of the DFB laser structure and the process is described. This should serve as a reference to all subsequent chapters where the structural details of the laser are discussed, and also provide some insight into the design choices made in this work.

The standard ridge waveguide DFB laser structure is shown on figure 1.2. As in any 1.55μm wavelength laser, the starting material is InP. An InGaAsP alloy can be lattice matched to this InP substrate and tailored so that its band-gap is approx-

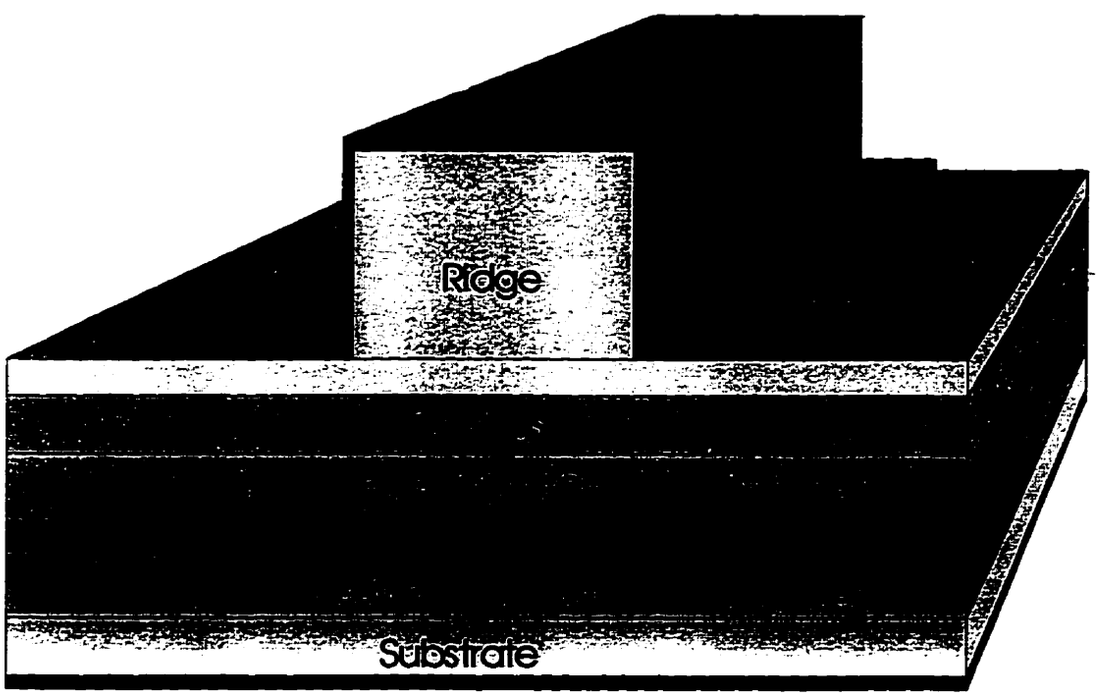

Figure 1.2: The structure of the ridge waveguide DFB laser.

imately 0.8eV (or $\lambda = 1.55\mu m$). Several epitaxial layers with different band-gaps are grown on the InP substrate by MOCVD. The multi-quantum wells (MQW) near the center of the stack is the gain medium. The thickness and depth of the quantum wells define the gain spectrum and the peak gain wavelength. The graded band-gap regions above and below the MQW are referred to as Graded Index Separate Confinement Heterostructure (GRINSCH). The primary purpose of the GRINSCH regions is to enhance the optical confinement along the vertical direction.

The gratings are made using standard holographic exposure and lithography. These are patterned above the top GRINSCH layers and etched using a wet chemical process. Following the grating etch, a layer of InP is *re-grown* by MOCVD. This re-growth phase is the part which introduces most of the complexities in a DFB process. As a result, several alternative processing schemes to eliminate this phase have been proposed [50, 51, 52, 53]. Nevertheless, due to the weak coupling coefficients in the other schemes, the etch and re-growth process is still the most practical scheme used in DFB lasers.

The top most layer is a thick layer of InP. This layer is dry etched to the correct dimension to provide the necessary lateral optical confinement. The etch-stop layer is used as an end-point detection. A layer of metal is deposited at the top and bottom of the structure to enable wire bonding to the p and the n side of the device. The facets are left as-cleaved, AR coated or HR coated depending on the application.

For further fabrication details on ridge waveguide DFB lasers refer to [54, 55, 56, 57, 58, 59, 60].

1.7 Problem Statement

In a broad sense, the focus of this thesis is to theoretically and experimentally investigate various Distributed Feedback Laser Array structures capable of emission at multiple wavelengths. Specifically, the question of how to control the laser wavelength using simple and practical ways are examined in detail. There are conceptually simple (but technologically challenging) methods such as selective area epitaxy and direct E-beam writing. Alternative methods such as ridge width and ridge tilt variation are also possible. These latter methods hold promise because of the expected yield and reliability due to the uniformly etched gratings. For this reason, the emphasis of this dissertation will be on the latter two schemes.

Although the fundamental relationships between laser behaviour and material parameters are fairly well known, very little work has been done to systematically study the role of device geometries. This is especially true with DFB Lasers. Therefore, one of the crucial parts of this research effort has been the development of a realistic physical model of the DFB laser. As a result, the first few chapters of this thesis are devoted to the description of this laser model. The later chapters examine specific laser array structures. The primary intended application of these laser arrays is Wavelength Division Multiplexing in fiber telecommunications.

1.8 Original Contributions Claimed in this Thesis

Original scientific contributions resulting from this Ph.D research can be summarized as follows:

- A quasi-three-dimensional DFB laser model in the spectral domain including transverse carrier and optical effects has been formulated and implemented

(chapters 2 and 3) [61].

- A multi-wavelength DFB laser array using ridge width control has been designed, theoretically modeled and experimentally demonstrated (chapter 4) [62, 63, 64, 65].

- A multi-wavelength DFB laser array using ridge tilt control has been theoretically modeled and experimentally demonstrated (chapter 5) [66, 67].

- The discrimination of transverse oscillation modes in DFB lasers has been identified and explained. It is demonstrated that the laser remains in single mode even for waveguides capable of supporting multiple modes, enabling a larger tuning range (chapter 4) [68].

- New and previously unknown effects of waveguide tilt on the DFB emission characteristics have been theoretically studied. and substantiated by experimental results (chapter 5) [69].

- Simultaneous four-wavelength WDM transmission into a single fiber has been demonstrated for the first time using the varying ridge width approach (chapter 4).

1.9 Outline of the Thesis

For the purpose of clarity, the presentation of the quasi-three-dimensional DFB Laser model is loosely divided into the *longitudinal* and *transverse* models. In the actual implementation the distinction is not that clear cut. In chapter 2 the longitudinal DFB laser model is described. A spectral domain approach is taken

here, and the whole structure is treated as consisting of a series of discrete feedback elements stacked back to back.

In chapter 3 the transverse DFB laser model is presented. The two-dimensional optical mode and the lateral carrier profiles are solved, which are then used to calculate the longitudinal parameters of the laser. An analysis of lateral leakage current is also presented in this chapter.

In chapter 4 the varying ridge width DFB laser array is presented. The laser model developed in the earlier chapters are applied to predict and interpret the measured results from these arrays. It is shown that single mode oscillation can be maintained even for ridges wide enough to support multiple modes. These claims are substantiated with experimental results.

In chapter 5 the varying ridge tilt laser array is presented. Using the model developed in the earlier chapters, important effects which have so far been ignored in the literature are identified. These are shown to lead to significant implications in performance. These claims are substantiated with experimental results.

Finally in chapter 6 conclusions and suggestions for future research are given.

Chapter 2

Distributed Feedback Lasers: Longitudinal Model

2.1 Introduction

In this chapter the longitudinal DFB laser model is presented. The description is based on the coupled wave theory for corrugated optical waveguides. The analysis is carried out in the spectral domain for a continuum of wavelengths. As such, the model is inherently capable of capturing the effects of all the longitudinal lasing and non-lasing modes. The model is developed in this chapter and its applications are demonstrated through a few examples at the end of the chapter.

2.2 Coupled Wave Theory for Distributed Feedback Structures

For an arbitrary dielectric waveguide it is rarely the case that its eigen functions will be known in a closed form expression. In those cases it is often easier to treat this as a perturbation problem. If the unperturbed structure is chosen such that its eigen solutions are known in closed form, then the solution of the perturbed structure can be expressed simply as a linear superposition of the unperturbed structure's solutions. This is the essence of coupled mode theory. The degree of approximation in the theory lies in the magnitude of the perturbation. For larger and larger perturbations, the accuracy of the model diminishes. Coupled mode theory can be successfully applied up to a moderate range of perturbations in grated structures. For larger perturbations, the accuracy of any perturbative approach will be diminished, and other techniques such as the Transfer Matrix Method will be more appropriate.

2.2.1 Unperturbed Solution

The optical wave propagation in an arbitrary medium is governed by Maxwell's wave equation of the form:

$$\nabla^2\mathbf{E} + \nabla\left[\frac{\mathbf{E}\cdot\nabla\eta^2}{\eta^2}\right] - \frac{1}{c^2}\frac{\partial^2\eta^2\mathbf{E}}{\partial t^2} - \mu_o\frac{\partial\sigma\mathbf{E}}{\partial t} = \mu_o\frac{\partial\mathbf{J}_s}{\partial t} \tag{2.1}$$

where $\mathbf{E}$ is the electric field, η is the refractive index. $\mathbf{J}_s$ is a current representing the spontaneous emission source, σ is the conductivity and c is the speed of light. When the refractive index variation is primarily along the transverse x, y plane and

the axial variation along z is slow, this equation can be decoupled into

$$\frac{\partial^2 \mathbf{E}}{\partial z^2} + \hat{H}_t \mathbf{E} - \frac{1}{c^2}\frac{\partial^2 \eta^2 \mathbf{E}}{\partial t^2} - \mu_o \frac{\sigma \partial \mathbf{E}}{\partial t} = \mu_o \frac{\partial \mathbf{J}_s}{\partial t} \tag{2.2}$$

where

$$\hat{H}_t \mathbf{E} = \nabla_t^2 \mathbf{E} + \nabla \left[\frac{\mathbf{E} \cdot \nabla \eta^2}{\eta^2} \right]. \tag{2.3}$$

Assuming a time dependency of the form $\mathbf{E} \sim e^{j\omega t}$ in the absence of $\partial \mathbf{J}_s / \partial t$ and σ the solution of equation (2.2) can be expressed by a sum of transverse fields $\mathbf{E}(x, y)$ with the constants a such as

$$\mathbf{E} = \int_\omega \sum_n a_n \mathbf{E}_n (x, y) e^{j(\omega t - \beta_n z)} d\omega. \tag{2.4}$$

In the above expression $\mathbf{E}_n (x, y)$ and β_n are the eigen function and eigen value solutions of the following equation:

$$\hat{H}_t \mathbf{E}_n (x, y) = \left[\beta_n^2 - k^2 \eta^2 (x, y) \right] \mathbf{E}_n (x, y) \tag{2.5}$$

and

$$\beta_n = \frac{\omega n_{eff,n}}{c}. \tag{2.6}$$

Equation (2.4) is the solution of a waveguide with no purtabation. As such, all the components under the summation will be orthogonal to each other representing non-interacting eigen mode solutions.

2.2.2 Perturbed Solution

Consider a perturbation $\Delta\eta (x, y, z)$, $\partial \mathbf{J}_s (x, y, z, t) / \partial t$ and σ being introduced into the structure. That is, the refractive index becomes:

$$\eta (x, y, z) = \eta_o (x, y, z) + \Delta\eta (x, y, z). \tag{2.7}$$

The solution of equation (2.2) will be assumed to be the same form as in (2.4) except for the time and space dependent coefficients $a(z,t)$. That is,

$$\mathbf{E} = \int_{\omega} \sum_{n} a_n(z,t)\, \mathbf{E}_n(x,y)\, e^{j(\omega t - \beta_n z)} d\omega. \tag{2.8}$$

Substitution of (2.7) and (2.8) into the wave equation (2.2) and making use of the slowly varying approximations (SVA)

$$\left| \frac{\partial^2 a_n(z,t)}{\partial z^2} \right| \ll \left| \beta_n \frac{\partial a_n(z,t)}{\partial z} \right|, \tag{2.9}$$

$$\left| \frac{\partial^2 a_n(z,t)}{\partial t^2} \right| \ll \left| \omega \frac{\partial a_n(z,t)}{\partial t} \right| \tag{2.10}$$

with some further mathematical manipulations results in the following set of coupled equations:

$$\int_{\omega} \left[\frac{\partial a_m(z,t)}{\partial z} - \sum_{n} \kappa_{mn} a_n(z,t) + \sum_{n} \chi_{mn} \frac{\partial a_n(z,t)}{\partial t} \right] d\omega = \int_{\omega} \zeta_m(z,t)\, d\omega. \tag{2.11}$$

This equation describes the evolution of the mode amplitudes due to the perturbation in the system. In an unperturbed system, the mode amplitudes will be invariant at all times. In the presence of a perturbation, however, the various modes become coupled to each other through κ_{mn} and χ_{mn} terms.

Equation (2.11) will be used as the basis for the rest of this chapter. It is general enough at this point to either represent co-directional or contra-directional coupling. In deriving equation (2.11) the eigen functions were assumed to be normalized to unity such that

$$\langle \mathbf{E}_m(x,y) \,|\, \mathbf{E}_m(x,y) \rangle = 1 \tag{2.12}$$

where the $\langle\rangle$ notation stands for integration in the x,y plane. The constants κ_{mn} in equation (2.11) are known as the *coupling coefficients*. These are the terms that

break the orthogonality of the unperturbed solutions in equation (2.4) and produces the coupling terms. This can be written as:

$$\kappa_{mn} = \left\langle \mathbf{E}_m(x,y) \left| \frac{k^2(\eta^2(x,y) - \eta_o^2(x,y)) - j\omega\mu_o\sigma(x,y)}{2j\beta_m} e^{j(\beta_m - \beta_n)z} \right| \mathbf{E}_n(x,y) \right\rangle . \tag{2.13}$$

The χ_{mn} term can be written as

$$\chi_{mn} = \left\langle \mathbf{E}_m(x,y) \left| \frac{k\eta^2(x,y)}{c\beta_m} + \frac{\mu_o\sigma}{2j\beta_m} \right| \mathbf{E}_n(x,y) \right\rangle , \tag{2.14}$$

and the spontaneous emission term as

$$\zeta_m(z,t) = \left\langle \mathbf{E}_m(x,y) \left| \frac{\mu_o e^{-j(\omega t - \beta_m z)}}{-2j\beta_m} \right| \frac{\partial \mathbf{J}_s(x,y,z,t)}{\partial t} \right\rangle . \tag{2.15}$$

The forward flowing photon flux density per angular frequency $P_{\omega,1}$ will be defined as

$$P_{\omega,1} = B_1 a_1 a_1^* \tag{2.16}$$

where the proportionality B_1 is given as [70]:

$$B_1 = \left(\frac{\beta_1}{2\mu_o\omega}\right)\left(\frac{1}{\hbar\omega}\right) . \tag{2.17}$$

Since $P_{\omega,1}$ only one angular frequency component, the total photon flux density is the integral of $P_{1,\omega}(z,t)$ over the entire angular frequency range of interest:

$$P_1(z,t) = \int_\omega P_{1,\omega}(z,t)\, d\omega . \tag{2.18}$$

2.2.3 Corrugated Waveguide

In a periodically corrugated structure, the perturbation $\Delta\eta(x,y,z)$ in equation (2.7) will have a periodicity along the $\hat{z}$ direction. This can be written as [71]

$$\Delta\eta(x,y,z) = \Delta\eta_o(x,y)\sin(Kz) . \tag{2.19}$$

Substituting (2.19) into (2.13) and neglecting the terms containing $\Delta\eta_o(x,y)^2$, the following expression for the coupling coefficient will result:

$$\begin{aligned}\kappa_{mn} &= \frac{k^2}{j\beta_m}\langle \mathbf{E}_m(x,y)|\eta_o(x,y)\,\Delta\eta_o(x.y)|\,\mathbf{E}_n(x,y)\rangle\,\frac{e^{jKz}-e^{-jKz}}{2j}e^{j(\beta_m-\beta_n)z} \\ &\quad +\frac{\mu_o\omega}{2\beta_m}\langle \mathbf{E}_m(x,y)|\sigma(x,y)|\,\mathbf{E}_n(x,y)\rangle\,e^{j(\beta_m-\beta_n)z} \\ &= \bar{\kappa}_{mn}\left[e^{j(\beta_m-\beta_n-K)z}-e^{j(\beta_m-\beta_n+K)z}\right]+\bar{\sigma}_{mn}e^{j(\beta_m-\beta_n)z} \qquad (2.20)\end{aligned}$$

where

$$\bar{\kappa}_{mn} = \frac{k^2}{2\beta_m}\langle \mathbf{E}_m(x,y)|\eta_o(x,y)\,\Delta\eta_o(x,y)|\,\mathbf{E}_n(x,y)\rangle \qquad (2.21)$$

$$\bar{\sigma}_{mn} = \frac{\mu_o\omega}{2\beta_m}\langle \mathbf{E}_m(x,y)|\sigma(x.y)|\,\mathbf{E}_n(x,y)\rangle\,. \qquad (2.22)$$

From equation (2.20) it can be seen that a strong coupling component will arise only between those modes that satisfy the *phase-matching condition* of $\beta_m-\beta_n=K$. All other components will have fast oscillation terms that will average out to zero. If we focus our attention to a narrow spectral range near this phase-matching region, the waves that contribute to this condition can be interpreted as two counter-propagating waves with propagation constants β_m and $-|\beta_n|$. The uniform loss (gain) term σ_{mn} produes a non-zero contribution only for the same mode, ie., it is a self-coupling term. It represents the net loss (gain) in the waveguide.

2.2.4 Coupled Wave Equations

In the rest of this thesis, only the two modes near the phase matching condition will be considered. All other modes away from the phase matching condition will be neglected. These two forward and backward moving transverse modes will be labeled with the subscripts 1 and 2 respectively.

The resulting two coupled mode equations, after neglecting the time derivative and the spontaneous emission terms, can then be written as:

$$\frac{\partial a_1(z)}{\partial z} - \kappa_{12} a_2(z) = 0 \tag{2.23}$$

$$\frac{\partial a_2(z)}{\partial z} - \kappa_{21} a_1(z) = 0. \tag{2.24}$$

These are the two equations that need to be solved in order to calculate the longitudinal properties of the DFB cavity. The two-dimensional transverse properties of the waveguide are buried the quantities κ_{12}, β_1 and β_2. The evaluation of these parameters for a two-dimensional waveguide structure will be described later in chapter 3. In the rest of this chapter the theoretical development of the DFB laser will proceed with the assumption that the quantities κ_{12}, β_1 and β_2 are already available.

2.2.5 Coupled Two-Wave Solution

The two-wave coupled equations (2.23) and (2.24) can be readily solved by substituting (2.24) into (2.23). This results in

$$\frac{\partial^2 a_1(z)}{\partial z^2} - \frac{1}{\kappa_{12}} \frac{\partial \kappa_{12}}{\partial z} \frac{\partial a_1(z)}{\partial z} - \kappa_{12}\kappa_{21} a_1(z) = 0. \tag{2.25}$$

Using equation (2.20) this reduces to

$$\frac{\partial^2 a_1(z)}{\partial z^2} - j(\beta_1 + |\beta_2| - K) \frac{\partial a_1(z)}{\partial z} - |\bar{\kappa}_{12}|^2 e^{2j\theta_{12}} = 0 \tag{2.26}$$

where θ_{12} is the phase of the complex coupling coefficient κ_{12}. Assuming a solution of the form

$$a_1(z) = a_{1o} e^{\Omega z} \tag{2.27}$$

the following solutions for equation (2.26) can be obtained:

$$a_1(z) = \left(Bre^{\gamma z} + Ae^{-\gamma z}\right) e^{j\delta z} \tag{2.28}$$

$$a_2(z) = \left(Be^{\gamma z} - Are^{-\gamma z}\right) e^{-j\delta z}. \tag{2.29}$$

Equations (2.28) and (2.29) describe the amplitudes of the forward and the backward traveling waves in the corrugated structure. Note that the $e^{\pm j\delta z}$ terms represent the traveling wave components while the $e^{\pm \gamma z}$ terms represent the exponential growth or decay terms due to the power transfer between the modes. The particular solution of these equations requires a boundary condition. This will be described in the next section.

The two new terms introduced in the above expressions are:

$$\gamma = \sqrt{|\bar{\kappa}_{12}|^2 e^{2j\theta_{12}} - \delta^2} \tag{2.30}$$

$$r = \frac{\bar{\kappa}_{12}}{\gamma + j\delta} \tag{2.31}$$

where δ is the detuning factor about the central Bragg frequency. This is defined as

$$2\delta = \beta_1 + |\beta_2| - K. \tag{2.32}$$

2.2.6 Reflection and Transmission Coefficients in the DFB Structure

Referring to figure 2.1, the left and right reflection coefficients in a DFB cavity can now be derived from the results in (2.28) and (2.29) as

$$r_1\left(0^+\right) = \frac{a_2(0^+)}{a_1(0^+)} \text{ with boundary condition at } r_1(\Delta z/2) \tag{2.33}$$

$$r_2\left(0^-\right) = \frac{a_1(0^-)}{a_2(0^-)} \text{ with boundary condition at } r_2(-\Delta z/2). \tag{2.34}$$

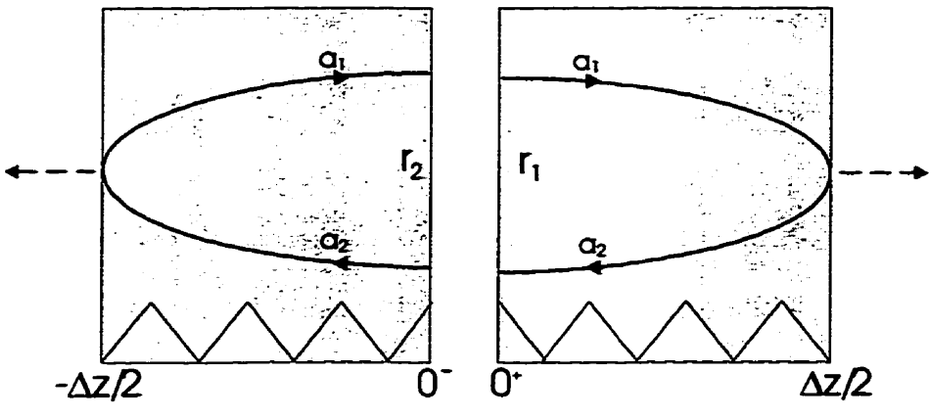

Figure 2.1: Reflection and transmission coefficients in a DFB structure.

Similarly, the transmission coefficients can be written as

$$t_1\left(0^+\right) = \frac{a_1\left(\Delta z/2\right)}{a_1\left(0^+\right)} \text{ with boundary condition at } r_1\left(\Delta z/2\right) \quad (2.35)$$

$$t_2\left(0^-\right) = \frac{a_2\left(-\Delta z/2\right)}{a_2\left(0^-\right)} \text{ with boundary condition at } r_2\left(-\Delta z/2\right) \quad (2.36)$$

The detailed derivations for these reflection and transmission coefficients are given in Appendix A.

2.3 Multi-Section Distributed Feedback Laser Model

The essentials of the multi-section DFB model are built from the formulations made in the earlier section, namely the DFB reflection and transmission coefficients. In order to account for the variation in photon flux and carrier density along the length, the DFB cavity is divided into a number of subsections. Within each subsection, the photon flux and carrier density are assumed to be uniform. This is as depicted on figure 2.2.

2.3.1 Reflections Through Multi-Sections

In order to complete the picture of figure 2.2, the reflection and transmission coefficients $r_{1,i}$, $r_{2,i}$, $t_{1,i}$ and $t_{2,i}$ have to be calculated from *any* point inside the DFB cavity. This has to be done taking the non-uniform cavity properties into account.

For example, referring to figure 2.2, the reflection coefficient $r_1\left(L - \Delta z/2\right)$ in subsection n_z is calculated using the boundary condition specified by the facet r_{F1}. Similarly, $r_1\left(2\Delta z + \Delta z/2\right)$ in subsection 3 is calculated using $r_1\left(3\Delta z\right)$ as the boundary condition.

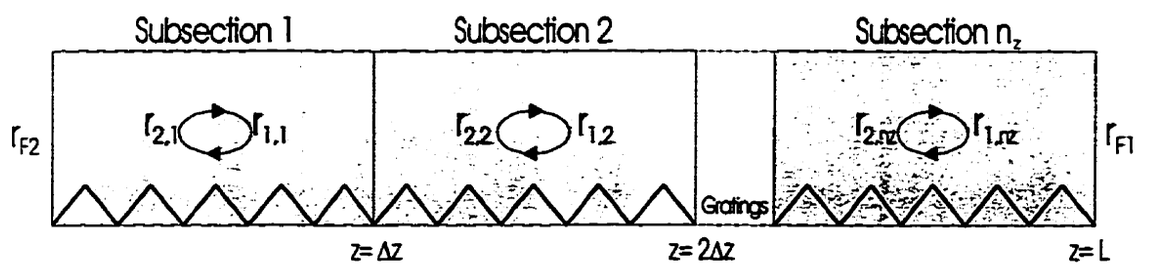

Figure 2.2: The laser structure is modeled as a stacked layer of several DFB subsections.

Similarly for r_2, the reflection coefficient $r_2(\Delta z/2)$ in subsection 1 is calculated using the boundary condition specified by the facet r_{F2}. $r_2(2\Delta z + \Delta z/2)$ in subsection 3 is calculated using $r_2(\Delta z)$ as the boundary condition.

A similar recursive formulation can be made for both transmission coefficients in each subsection.

2.3.2 Feedback Model

Figure 2.3 shows the equivalent feedback circuit model used within each subsection i. The left and right reflection coefficients are $r_{2,i}$ and $r_{1,i}$ respectively as described in the previous section. $a_{1,i,j}$ and $a_{2,i,j}$ are the forward and backward moving fields in subsection i due to fields transmitted from subsection j. Note that the three subscripts for a denote the direction, location and origin of the field respectively. For example, $a_{1,3,2}$ stands for the forward moving field in subsection 3 due to the field transmitted from subsection 2. $a_{sp1,i}$ and $a_{sp2,i}$ are the field amplitudes due to the spontaneous emission in subsection i. $a_{sp1,i}$ is the forward moving field and $a_{sp2,i}$ is the backward moving field.

Referring to figure 2.3, $a_{1,i,i}$ and $a_{2,i,i}$ are the forward and backward moving fields in the i-th subsection as a result of the spontaneous emission *within* that subsection. At steady-state, $a_{1,i,i}$ should be equal to the resulting value after traversing once around the feedback loop. That is:

$$a_{1,i,i} = (a_{1,i,i} r_{1,i} + a_{sp2,i})\, r_{2,i} + a_{sp1,i}. \tag{2.37}$$

This results in:

$$a_{1,i,i} = \frac{a_{sp2,i} r_{2,i} + a_{sp1,i}}{1 - r_{1,i} r_{2,i}}. \tag{2.38}$$

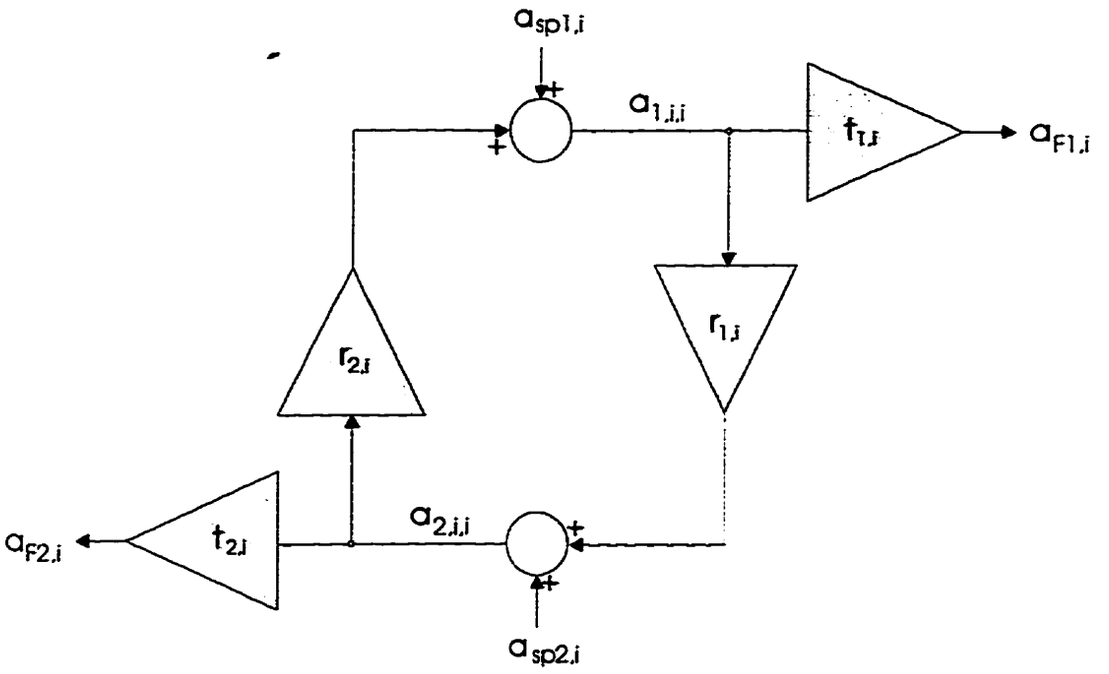

Figure 2.3: Each subsection is modeled as a positive feedback element.

Similarly for $a_{2,i,i}$:

$$a_{2,i,i} = \frac{a_{sp1,i} r_{1,i} + a_{sp2,i}}{1 - r_{1,i} r_{2,i}}. \tag{2.39}$$

Since $a_{sp1,i}$ and $a_{sp2,i}$ are spontaneously emitted fields they will be completely incoherent with each other. This fact will be utilized to convert the field equations into power equations. Due to this incoherence the time averaged overlap between the two fields will be zero, thereby eliminating the need to carry the cross terms. Therefore,

$$a_{sp1,i} a^*_{sp2,i} = 0. \tag{2.40}$$

This is an important step in the derivation of this DFB model. By converting all field quantities to power quantities, the requirements for handling the random phase of the spontaneous emission field are conveniently avoided.

The *total* spontaneous emission power per angular frequency in subsection i will be represented as $P_{\omega,sp,i}$. Then the amount of power coupled into the forward and backward traveling transverse modes can be related through the constants Q_1 and Q_2 as:

$$|a_{sp1,i}|^2 = Q_1 P_{\omega,sp,i} \tag{2.41}$$

$$|a_{sp2,i}|^2 = Q_2 P_{\omega,sp,i}. \tag{2.42}$$

The following assumptions regarding the coupling of spontaneous emission into the various transverse modes will be made:

- $Q_1 = Q_2$; i.e, the spontaneously emitted power is equally coupled into the forward and backward directions.

- Whenever there are more than one transverse mode present in the waveguide structure, the amount of spontaneous emission coupled into each transverse mode will be assumed to be equal.

- Although it is possible to consider a realistic spectral shape for $P_{\omega,sp,i}$, for simplicity it will be assumed to be a flat noise spectrum. As a result, the spontaneous emission power will be constant within the entire range of optical frequencied being considered. Although this is not very realistic when a large spectral range is being considered, for narrow ranges it can be fairly accurate.

From the above, the photon flux density (# of photons crossing per unit cross-sectional area per unit time) in the forward and backward directions corresponding to $a_{1,i}$ and $a_{2,i}$ can be written as:

$$P_{\omega,1,i} = P_{\omega,sp,i}\left(\frac{1+|r_{2,i}|^2}{|1-r_{1,i}r_{2,i}|^2}\right) \tag{2.43}$$

$$P_{\omega,2,i} = P_{\omega,sp,i}\left(\frac{1+|r_{1,i}|^2}{|1-r_{1,i}r_{2,i}|^2}\right). \tag{2.44}$$

2.3.3 Transmission Through Subsections

The photon flux density $P_{\omega,1,i,i}$ will be transmitted to it's neighbouring subsections $i+1$, $i+2$, etc. Similarly, $P_{\omega,2,i,i}$ will be transmitted to it's neighbours $i-1$, $i-2$, etc. This is shown on figure 2.4. As a result, the total photon flux density $P_{\omega,1,i}$ and $P_{\omega,2,i}$ in each subsection i has to be written as a superposition:

$$P_{\omega,1,i} = \sum_{j=1}^{i} P_{\omega,1,i,j} \tag{2.45}$$

$$P_{\omega,2,i} = \sum_{j=i}^{n_z} P_{\omega,2,i,j}. \tag{2.46}$$

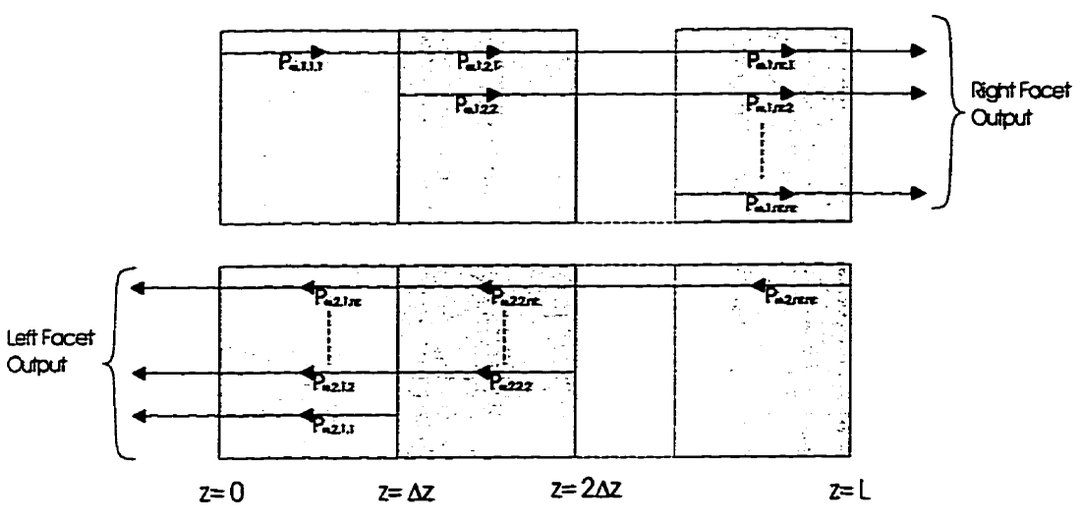

Figure 2.4: Photons generated in one subsection is transmitted through every other subsection.

The value of $P_{\omega,1,i,j}$ (photon flux density in subsection i due to transmission from subsection j) can be determined from the transmission coefficients from subsection j to i. This transmission coefficient will be denoted as $t^i_{1,j}$. Using equations (2.43), (2.44), (2.45) and (2.46), the following expression for the photon flux in each subsection can be derived:

$$P_{\omega,1,i} = \sum_{j=1}^{i} P_{\omega,sp,j} \left(\frac{1+|r_{2,j}|^2}{|1-r_{1,j}r_{2,j}|^2} \right) \left| t^i_{1,j} \right|^2 \tag{2.47}$$

$$P_{\omega,2,i} = \sum_{j=i}^{n_z} P_{\omega,sp,j} \left(\frac{1+|r_{1,j}|^2}{|1-r_{1,j}r_{2,j}|^2} \right) \left| t^i_{2,j} \right|^2 . \tag{2.48}$$

Within each section, the stimulated emission current can be written as (see derivation in Appendix B):

$$I_{i,st} = q\Delta z \int_\omega \int_x \int_y (P_{\omega,1,i} + P_{\omega,2,i})\, 2k\Im\{\eta\} d\omega\ dx\ dy. \tag{2.49}$$

The $2k\Im\{\eta\}$ term in the above equation represents the power gain in the medium. Further, within each section, the currents due to spontaneous and non-radiative transitions can be written as $I_{i,sp}$ and $I_{i,nr}$. Therefore, the total injected current in each section becomes:

$$I_i = I_{i,st} + I_{i,sp} + I_{i,nr}. \tag{2.50}$$

2.3.4 Facet Output Power

Once the photon flux terms $P_{\omega,1,i}$ and $P_{\omega,2,i}$ are known, then all the information needed to complete the steady-state picture of the DFB model are available (see figure 2.5).

The facet output power will be the photon flux in subsections 1 and n_z multiplied by the facet transmissions from those subection. The total optical power out of the

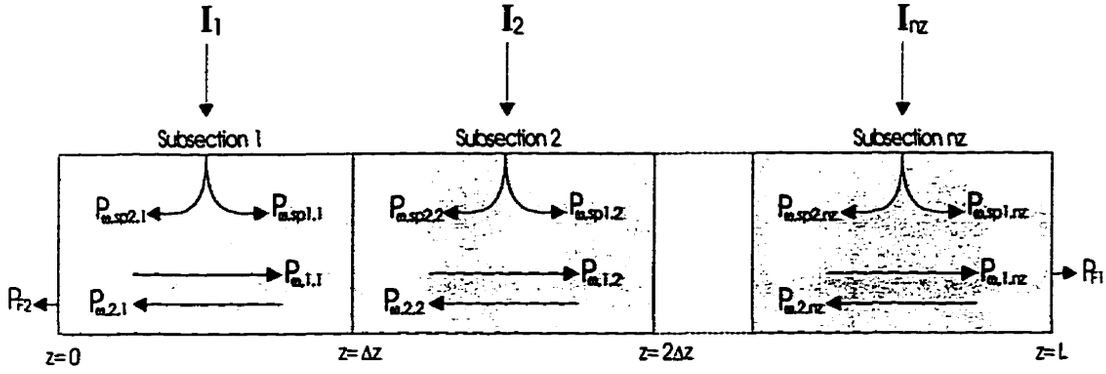

Figure 2.5: Depiction of stimulated and spontaneous emissions in each subsection.

facets can then be written as [11, 8]:

$$P_{\text{opt},F1} = \int_{\omega}\int_{x}\int_{y}\sum_{i=1}^{n_z}\hbar\omega P_{\omega,1,i,i}\,|t_{1,i}|^2\,dy\,dx\,d\omega \tag{2.51}$$

$$P_{\text{opt},F2} = \int_{\omega}\int_{x}\int_{y}\sum_{i=1}^{n_z}\hbar\omega P_{\omega,2,i,i}\,|t_{2,i}|^2\,dy\,dx\,d\omega. \tag{2.52}$$

The integration is carried out across the transverse cross-sectional area and the angular frequency range of the DFB laser.

2.4 Material Interaction Models

2.4.1 Gain Model

A simple gain model appropriate for quantum wells will be used in the rest of this work. It has been shown that the quantum well gain peak and the injected carrier density are related logarithmically [72, 73, 74, 75, 76]. That is:

$$kIm\{\eta\} = \frac{1}{2}a\ln\left(\frac{n}{n_{tr}}\right). \tag{2.53}$$

In this expression a is the gain coefficient and n_{tr} is the transparent carrier density.

Further, the spectral gain profile will be assumed to be flat. This is similar to the assumption made earlier for the spontaneous emission profile. Although this is not very realistic when large spectral ranges are considered, for narrow spectral ranges it is expected to be reasonable. The simulations considered in this thesis are for spectral ranges of less than about 15nm.

2.4.2 Line Width Enhancement Factor

The refractive index has a dependence on the carrier density [77, 78]. This is due to the free carrier or plasma effect, and the effects associated with the change in the gain spectrum. Using Kramer's Krönig relation this can be expressed by a constant α which relates the change in gain of the medium to the change in the real part of the refractive index. This parameter is also known as the line-width enhancement factor, and is defined as

$$\alpha = \frac{\mathrm{Re}\{\Delta\chi_p\}}{\mathrm{Im}\{\Delta\chi_p\}}. \tag{2.54}$$

The permittivity of the medium is $\epsilon = 1 + \chi + \chi_p$ where the reactivity χ_p is due to the carrier injection into the medium. Since the refractive index is $\eta = \sqrt{\epsilon}$ it can be shown that for small χ_p

$$\Delta k \approx \frac{k_o}{2\eta_o}\frac{\partial\chi_p}{\partial n}\Delta n. \tag{2.55}$$

Therefore, an increase in the carrier density n is reflected as an increase in the wave-vector k. In the model, this effect of α can be conveniently included in the detuning frequency δ such as:

$$\begin{aligned} 2\delta &= \beta_m + |\beta_n| + \alpha\left(\Re\{\Delta\beta_m\} + |\Re\{\Delta\beta_n\}|\right) - K + \\ &\quad j\left(\Im\{\Delta\beta_m\} + |\Im\{\Delta\beta_n\}|\right). \end{aligned} \tag{2.56}$$

2.4.3 Gain Saturation

At high photon flux inside the laser cavity, the gain becomes suppressed due to an effect called the gain saturation. This is denoted by the symbol ϵ. This is arises due to material effects as well as due to structural properties. For example, the effect of transverse spatial hole burning, which is a structural property, can be accounted for in ϵ.

The effects of gain saturation is included in the gain expression as:

$$g_i(n) = \frac{a \ln(n/n_{tr})}{1 + \epsilon/v_g (P_{1,i} + P_{2,i})}. \tag{2.57}$$

At high photon flux densities, the denominator in the gain expression increases, reducing the overall gain.

2.5 Method of Solution

2.5.1 Formulation

For the purposes of solving, the input current which is specified in the units of A/cm will split in two parts: the part that contributes to stimulated emission I_{st} and the part that contains the non-radiative and spontaneous emissions I_{nst}:

$$I = I_{nst} + I_{st} \tag{2.58}$$

$$I_{nst} = I_{nr} + I_{sp}. \tag{2.59}$$

I_{nst} is used as the input quantity to solve for the transverse carrier profile. This is described in chapter 3. The effect of I_{st} is neglected in solving for the transverse carrier profile. This is tantamount to neglecting the transverse spatial hole burning. The resulting quantities are the spontaneous and non-radiative currents I_{sp} and I_{nr} and the spontaneous volume current $G_{\omega,sp}$. The two-dimensional quantities κ_{mn} and β_m are also calculated from the transverse model.

These two-dimensional transverse quantities are used to calculate the one-dimensional DFB reflection and transmission coefficients. These are then used to calculate the total photon flux density given by equations (2.43) and (2.44). From the total field, the stimulated emission portion of the current I_{st} is calculated from equation (2.49).

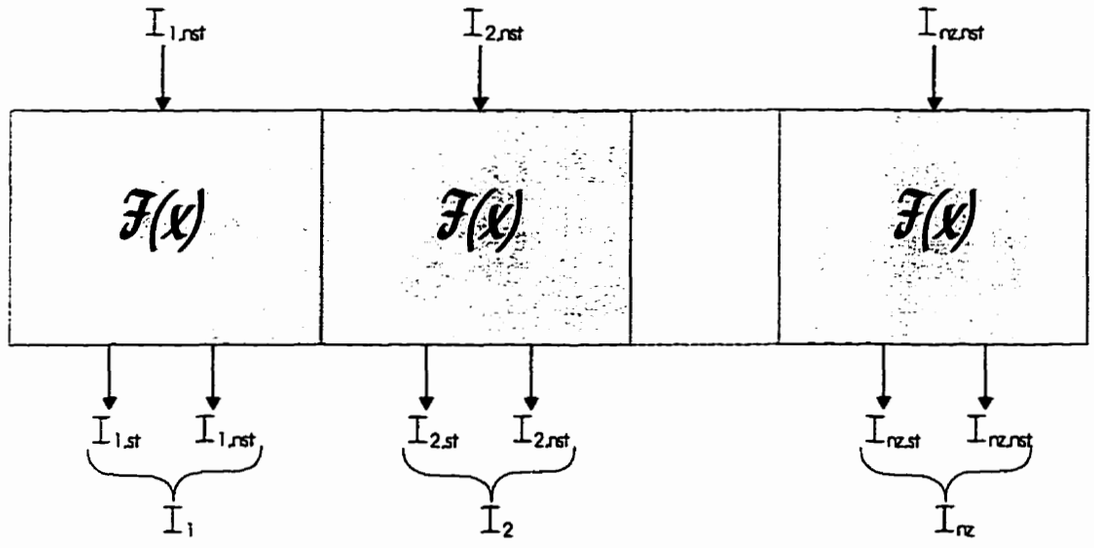

Figure 2.6: Diagrammatic description of the numerical solution method.

This results in the total current $I = I_{nst} + I_{st}$. Mathematically this can be written as (see figure 2.6)

$$\mathbf{I} = \mathcal{F}\ \mathbf{I_{nst}} \tag{2.60}$$

where $\mathbf{I}$ and $\mathbf{I_{nst}}$ are given by the vector quantities

$$\mathbf{I} = \begin{bmatrix} I_1 \\ I_2 \\ I_3 \\ \vdots \\ I_{nz} \end{bmatrix} \tag{2.61}$$

and

$$\mathbf{I_{nst}} = \begin{bmatrix} I_{1,nst} \\ I_{2,nst} \\ I_{3,nst} \\ \vdots \\ I_{nz,nst} \end{bmatrix}, \tag{2.62}$$

and $\mathcal{F}$ is the non-linear matrix containing equations (2.43), (2.44) and (2.49). The goal is to find $\mathbf{I_{nst}}$ for any given input current $\mathbf{I}$. However, for ease of solution, the approach taken here is to solve for $\mathbf{I}$ for a given $\mathbf{I_{nst}}$. Since $\mathbf{I}$ and $\mathbf{I_{nst}}$ have a one-to-one correspondence, the two approaches are equivalent.

2.5.2 Numerical Solution Method

Equation (2.60) is highly non-linear and can only be solved by numerical iteration. The method followed here is to assume an initial estimate for $\mathbf{I_{nst}}$ for a given input current distribution $\mathbf{I}$. Since a one-pass evaluation of equation (2.60) is computationally expensive, conventional methods of iterative solution would consume

excessive computational resources. In order to overcome this difficulty the following method is used: the iterative improvement on $\mathbf{I_{nst}}$ is obtained by first obtaining the photon flux density distribution $\mathbf{P}$

$$\mathbf{P} = \mathcal{E}\ \mathbf{I_{nst}}. \tag{2.63}$$

The operator $\mathcal{E}$ in the above expression contains the equations (2.47) and (2.48). This is used in the following steady-state rate equation to solve for an improved value of $\mathbf{I'_{nst}}$

$$\mathbf{I} = \mathbf{I'_{nst}} + q\mathbf{P} \cdot \mathbf{g}^T(\mathbf{I'_{nst}}) \tag{2.64}$$

$$= \mathbf{I'_{nst}} + q(\mathcal{E}\mathbf{I_{nst}}) \cdot \mathbf{g}^T(\mathbf{I'_{nst}}). \tag{2.65}$$

g in the above expression is the the gain distribution, which can be expressed as a function of $\mathbf{I'_{nst}}$, and can be written as

$$\mathbf{g} = 2k \begin{bmatrix} \Im\eta_1(I_{1,nst}) \\ \Im\eta_2(I_{2,nst}) \\ \Im\eta_3(I_{3,nst}) \\ \vdots \\ \Im\eta_{nz}(I_{nz,nst}) \end{bmatrix}. \tag{2.66}$$

The repeated improvement on $\mathbf{I_{nst}}$ by applying equation (2.65) is terminated when the improvement becomes negligible.

2.6 Demonstration of the Model

In this section the DFB model developed in the previous sections is demonstrated through a few examples.

2.6.1 Truncated Quantum Well Gain-Coupled DFB Lasers

Complex coupling in the form of gain coupling can be provided by periodically truncating the quantum wells by etching [79, 80, 81, 82, 83, 84]. This produces a corrugation in the real part of the refractive index as well as the imaginary part. The imaginary part of the corrugation will not be a constant, but will be a function of the injection current. As a result, the strength of the mode selection properties will change as a function of injection. In the following examples, an eight-quantum well laser with two truncated quantum wells is considered. This is shown schematically on figure 2.7. The other relevant laser parameters are listed on table 2.6.1. Except for the active region and the top SCH region, the rest of the transverse structure is as shown on figure 4.1 in chapter 4.

On figure 2.8 the lasing spectrum as a function of injection current is shown for the laser structure described on table 2.6.1. The spectrum is shown for three different injection currents: 15mA, 30mA and 40mA. Due to the gain-coupling effect, the long wavelength side of the DFB mode will be the preferred mode of oscillation. The threshold current of the laser is about 30mA. This can be identified on figure 2.8 from the rapid increase in optical output power at the long wavelength side of the DFB stop-band near 30mA. 15mA is below threshold and 40mA is above threshold. Below threshold, the gain increases with increasing carrier injection. With increasing gain, the line-width enhancement factor α causes a reduction in the refractive index of the medium. As a result, the spectrum shows the characteristic blue-shift. Near and above threshold, the change in gain with increasing current injection will be extremely small because almost all of the injected current is expended in producing stimulated emission. This results in a smaller blue-shift with increasing injection.

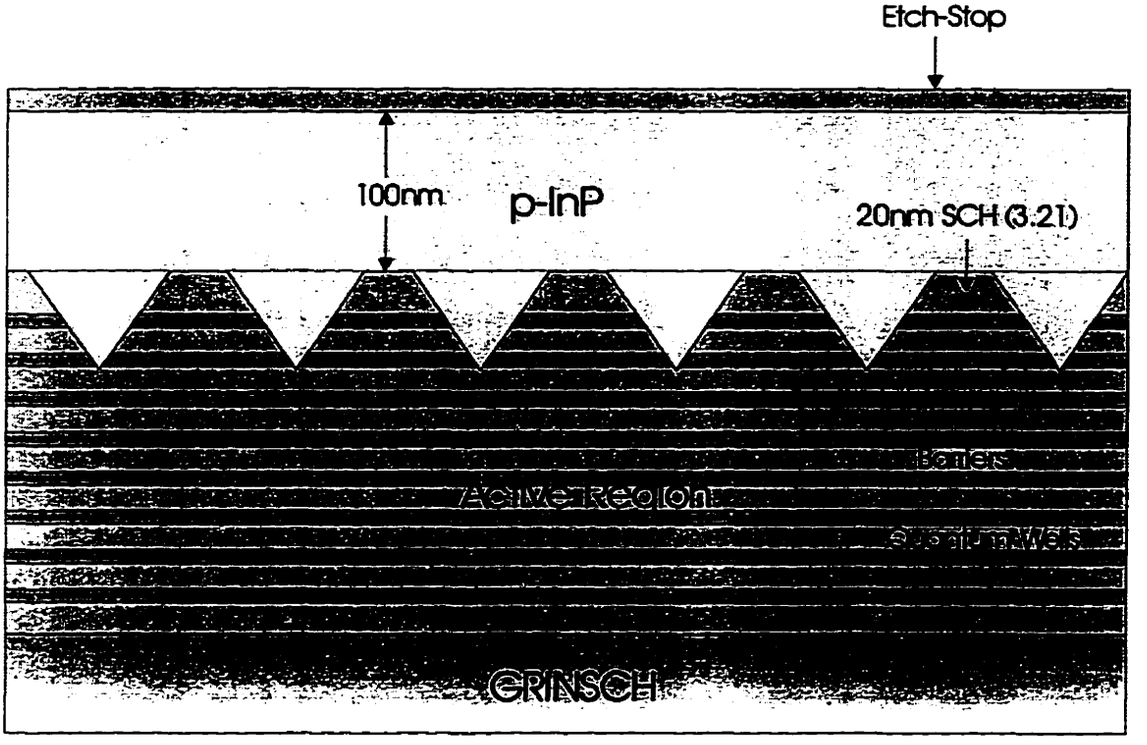

Figure 2.7: Periodically truncated quantum well gain-coupled structure.

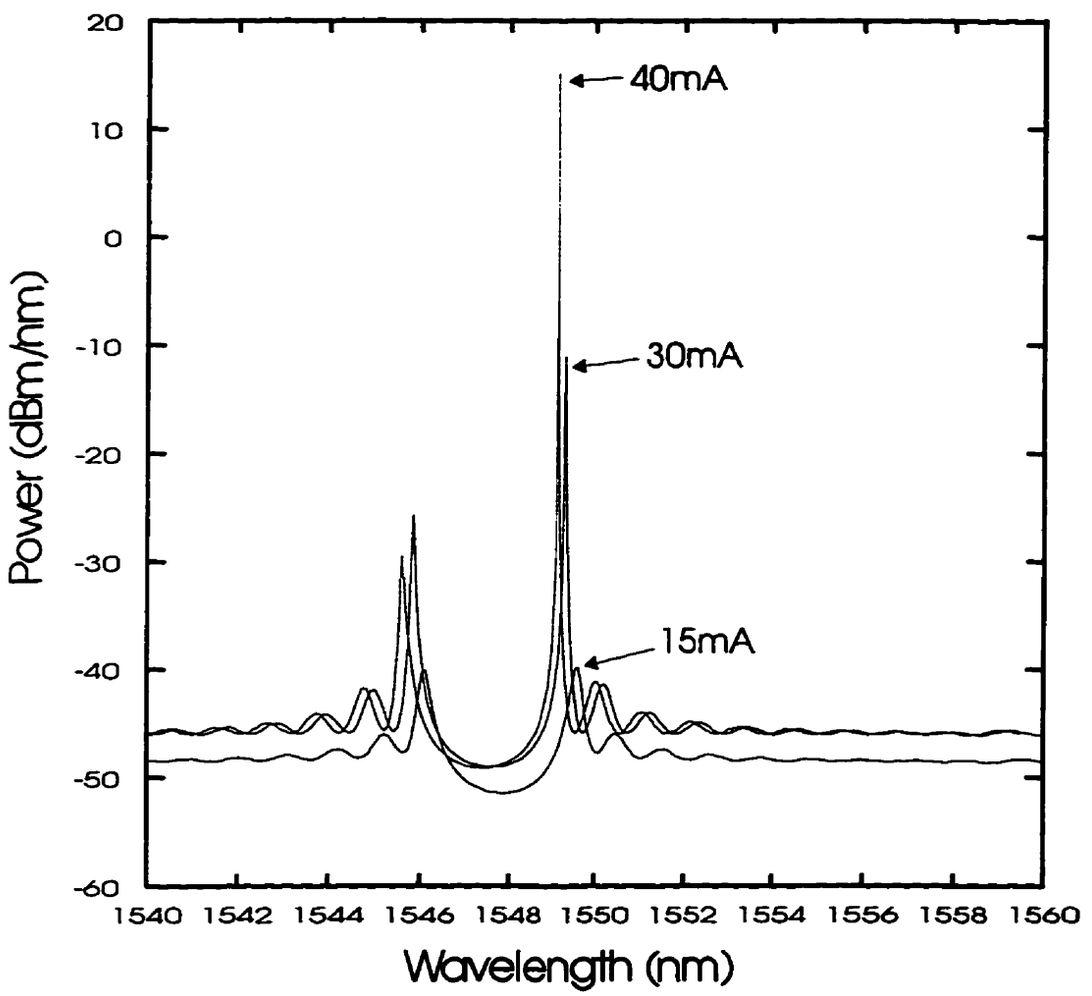

Figure 2.8: Lasing spectrum of the gain-coupled laser.

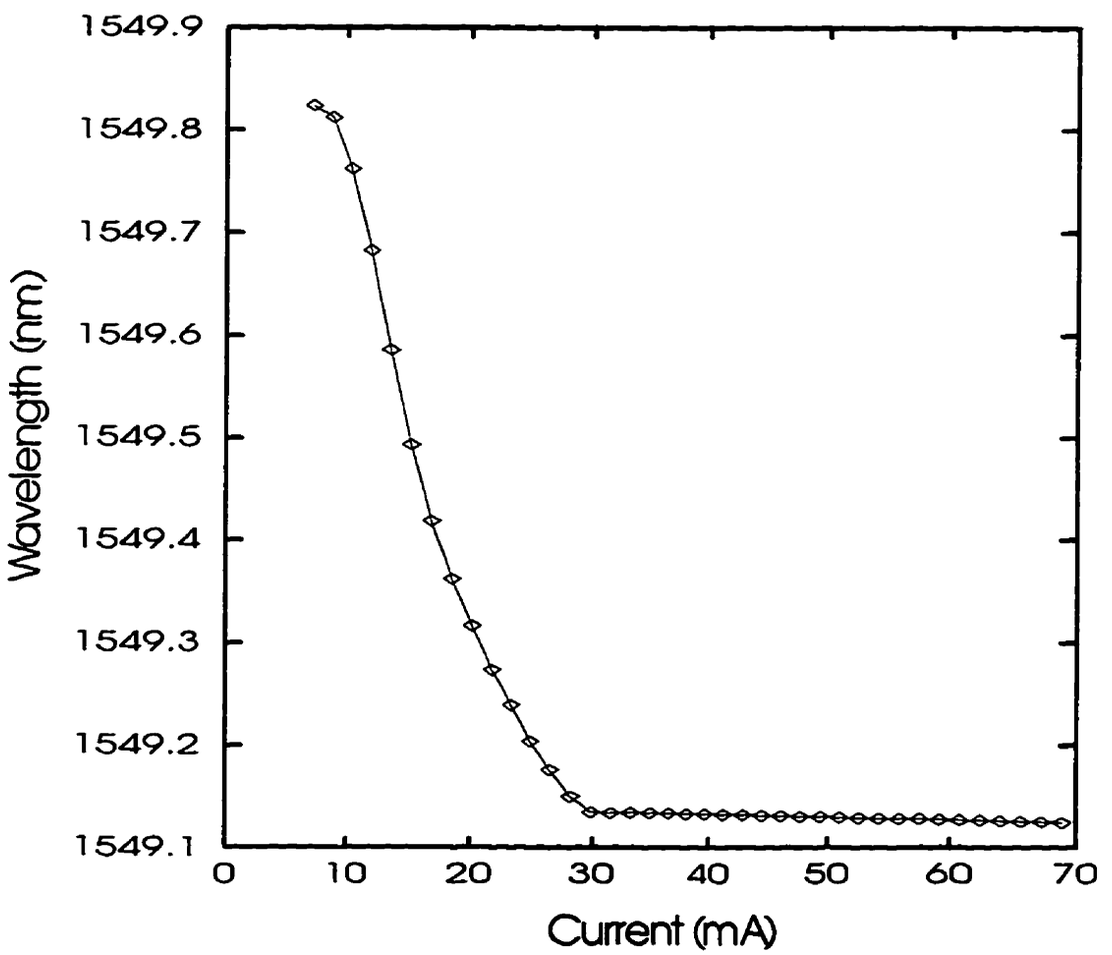

Figure 2.9: Wavelength with injection current for the gain-coupled laser.

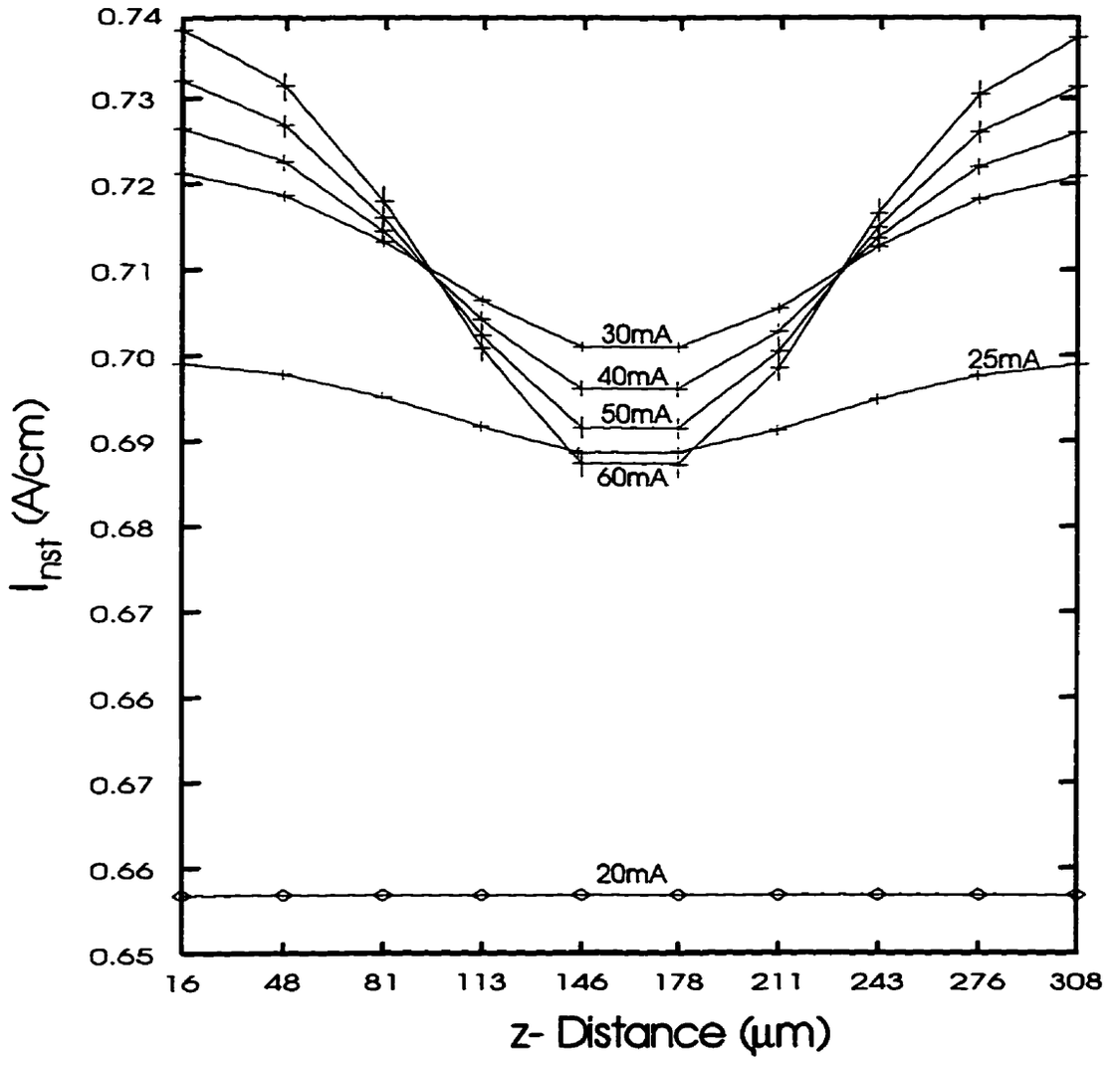

Figure 2.10: I_{nst} as a function of cavity distance in the gain-coupled DFB laser.

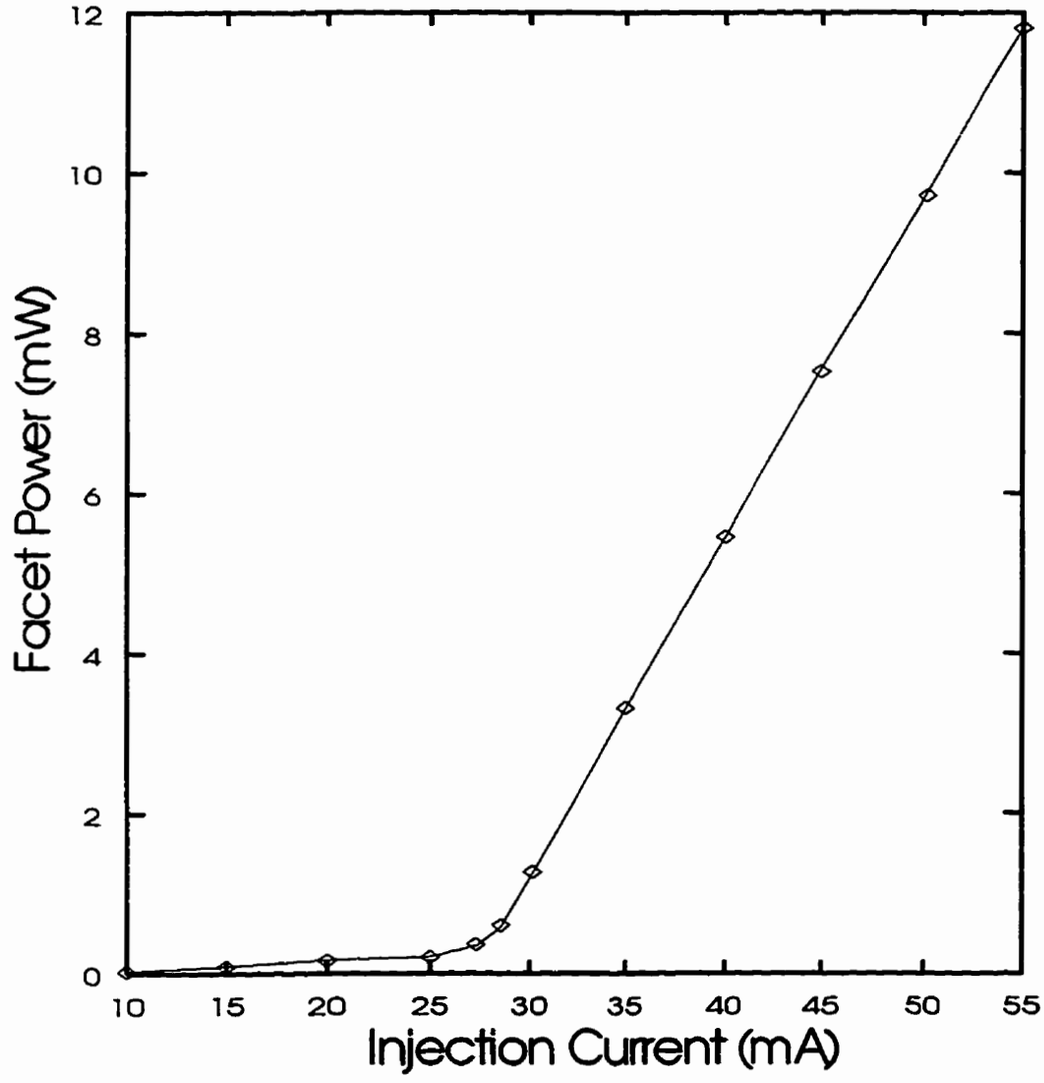

Figure 2.11: L-I curve of the gain-coupled DFB laser.

Name	Parameter	Value	Units
Cavity Length	L	325	μm
Grating Pitch	$2\pi/K$	241.455	nm
Gain Coefficient	a	1000	cm^{-1}
Transparent Carrier Density	n_{tr}	1.0×10^{18}	cm^{-3}
Facet Reflectivities	$r_{1,2}$	0	-
Scattering Loss	α_s	40	cm^{-1}
Line Width Enhancement Factor	α	-2.5	-
Linear Recombination	A	2.5×10^{8}	s^{-1}
Bimolecular Recombination	B	1.0×10^{-10}	$cm^3 s^{-1}$
Auger Recombination	C	3.0×10^{-29}	$cm^6 s^{-1}$
Transverse Structure	Figure 4.1	-	-
Quantum Well Structure	Figure 4.1	-	-
Grating Structure	Figure 2.7	-	-
Ridge Width	W	2.0	μm
Thickness of the top InP Layer	d_0	180	nm
Acceptor Concentration	N_A	6.0×10^{17}	cm^{-3}
Donor Concentration	N_D	6.0×10^{17}	cm^{-3}
Non-linear Gain Factor	ϵ	2×10^{-17}	cm^3
Hole Mobility	μ_p	100	$cm^2 V^{-1} s^{-1}$
Electron Mobility	μ_n	6×10^{3}	$cm^2 V^{-1} s^{-1}$

Table 2.1: Table of numerical values used for the simulation.

On figure 2.9 the change in lasing wavelength with increasing injection current is shown. As noted earlier, when the laser is below threshold, the wavelength shifts towards the shorter wavelengths. At and above threshold, more and more of the injected current contributes to stimulated emission instead of contributing towards increasing the carrier density. This is what is known as *carrier density clamping.* As a result, the blue-shift is much slower above threshold. In reality, however, one would observe a significant amount of red-shift above a certain current level due to the ohmic and non-radiative heating effects that takes place inside the laser. It is known that the refractive index increases with increasing temperature. As a result, initially one would observe a blue-shift, followed by a red-shift with increasing current injection. The exact nature of the red-shift is highly dependent on the thermal resistivity and the geometry of the laser. In the above model, thermal effects have not been considered.

On figure 2.12 the photon and gain (related to carrier) distributions are shown for different values of coupling coefficients κ. Since the threshold currents are different for these lasers, in order to make a fair comparison, the injection current was set at 50mA above the threshold current of the lasers. Figure 2.12a shows the photon flux and 2.12b shows the gain profile as a function of the cavity distance. Note that as κ increases from 60.0/cm to 120.0/cm the average modal gain decreases indicating a lower threshold gain. On the other hand, the spatial non-uniformity of the photons and the gain profile increases with κ indicating a larger amount of spatial hole burning. In general, the gain and the photon flux distributions will be correlated to one another in such a manner such that the product of the two yield the stimulated recombination current of 50mA.

On figure 2.11 the optical output power as a function of the injection current is shown. This is the well known L-I curve of the laser.

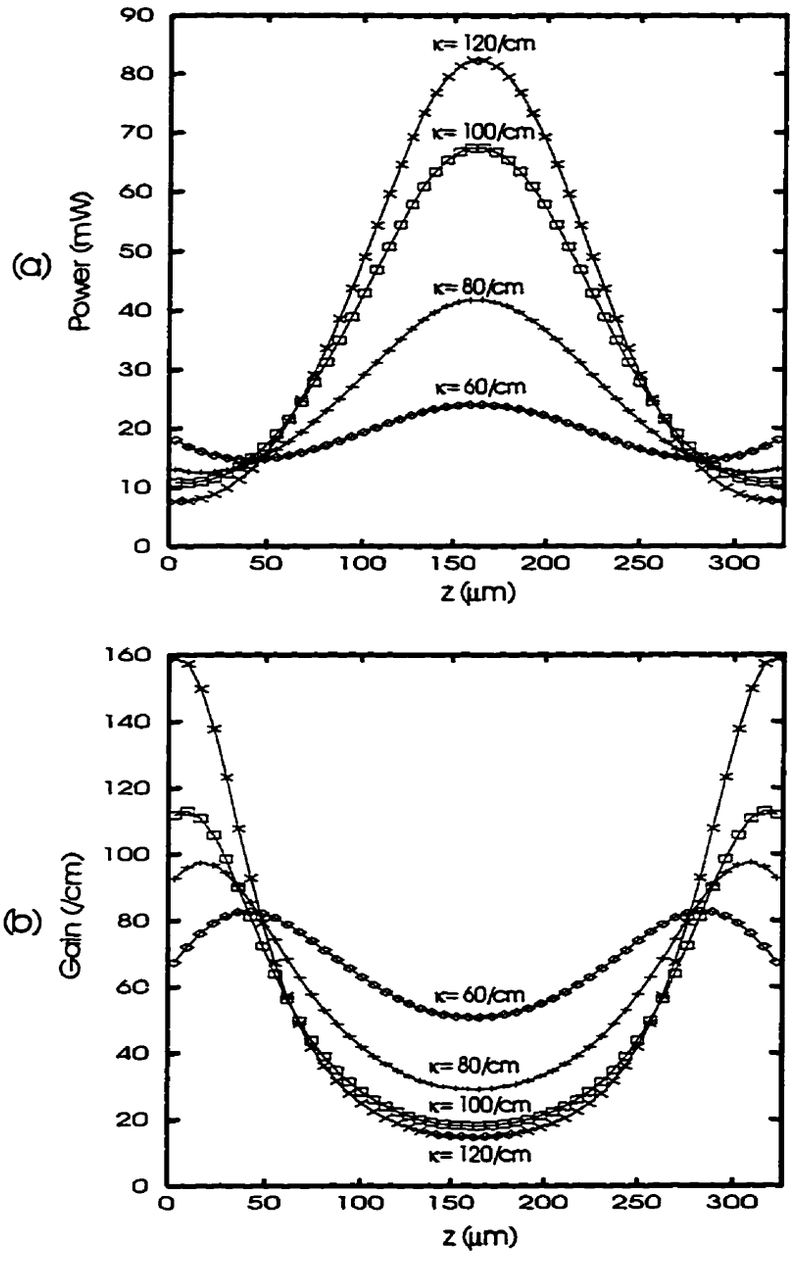

Figure 2.12: (a) Photon flux, and (b) gain distribution in an index-coupled DFB cavity for $\kappa = 60/\text{cm}$, $80/\text{cm}$, $100/\text{cm}$ and $120/\text{cm}$ at $I = I_{th} + 50\text{mA}$. The cavity length was assumed to be $325\mu\text{m}$.

2.6.2 Mode Selection due to Spatial-Hole Burning in Index-Coupled DFB Lasers

Index coupled DFB lasers are normally considered as having two degenerate lasing modes placed symmetrically about the DFB stop-band. Although this is true below threshold, at injections above threshold this symmetry is broken by the spatial hole burning effect. Spatial hole burning is the result of depleted gain (or carriers) near the location of the peak optical intensity. Since gain (or carriers) and the refractive index are related through the line-width enhancement factor α, this results in a higher refractive index at the location of the peak optical intensity. The non-uniform refractive index profile along the length of the DFB cavity breaks the symmetry of the two otherwise degenerate modes. It has been shown that an optical intensity maximum will be located at the middle of the cavity if $\kappa L > 1.6$, while an optical intensity minimum will be located at the middle of the cavity for $\kappa L < 1.6$ [22].

On figure 2.13 the spectrum of an index coupled DFB laser with $\kappa \approx 2.6$ is shown. The line-width enhancement factor α causes non-uniform refractive index profile to evolve in the cavity with increasing injection current. This results in a lasing preference towards the shorter wavelength DFB mode. This can be seen from figure 2.13, where at low injection currents both DFB modes are equally excited, and as spatial hole burning sets in, the preference shifts towards the shorter wavelength side. The corresponding refractive index profile is shown on figure 2.14. It can be seen that, with increasing injection current, spatial hole burning causes a peak in the refractive index in the middle of the cavity.

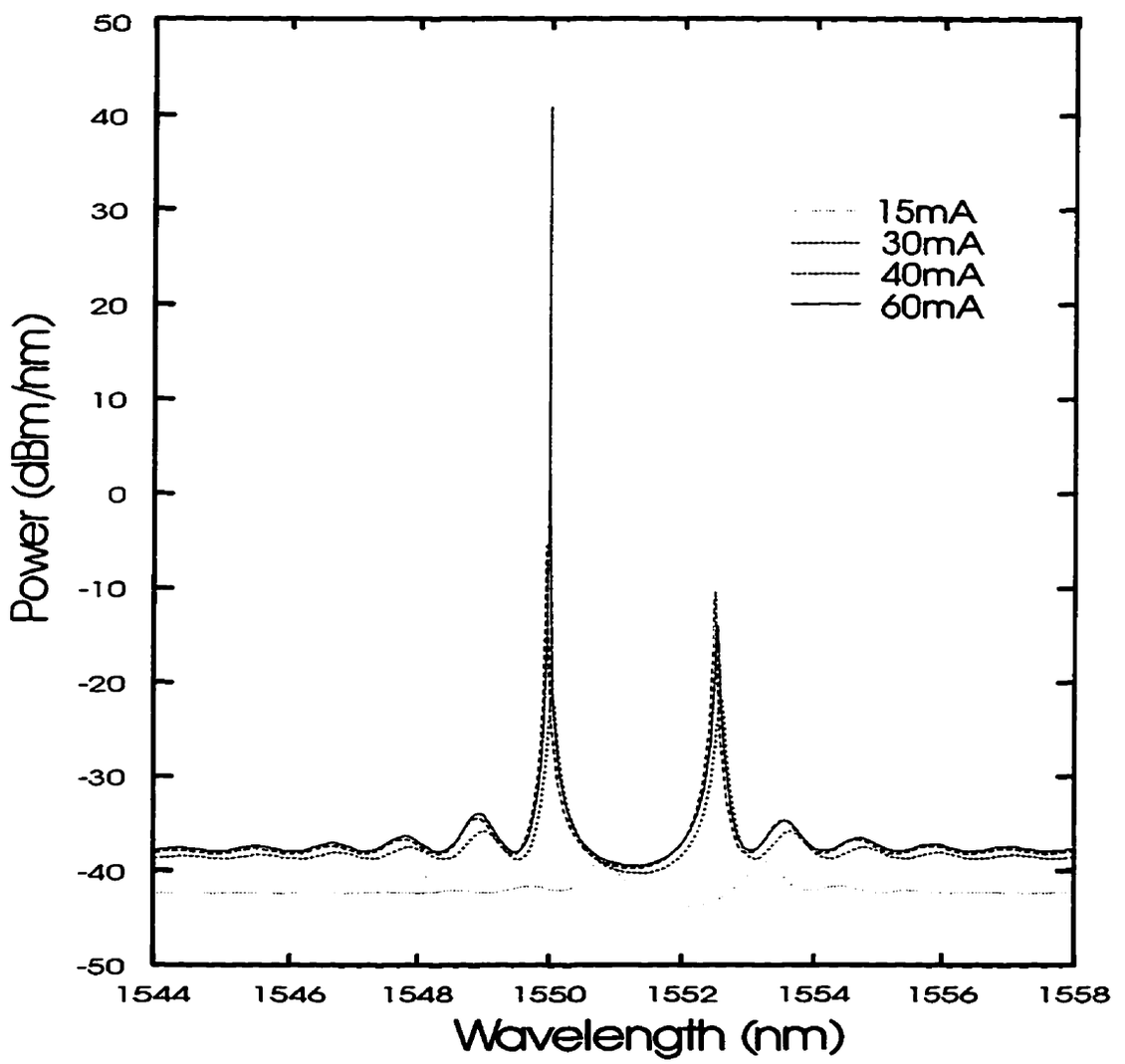

Figure 2.13: Effect of spatial hole burning on the lasing spectrum of index-coupled DFB laser with $\kappa L \approx 2.6$.

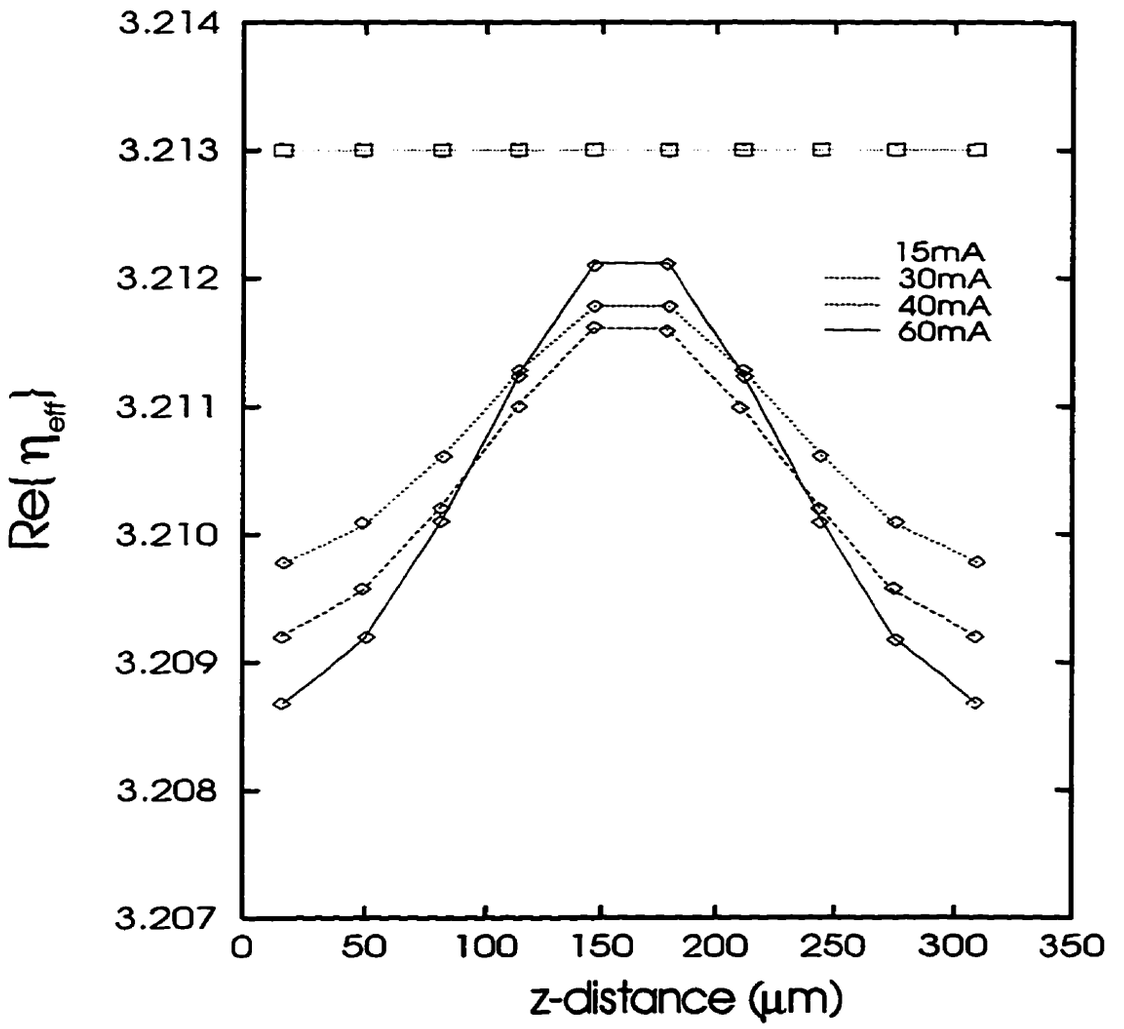

Figure 2.14: Effect of spatial hole burning on the effective index of index-coupled DFB laser with $\kappa L \approx 2.6$.

2.7 Conclusions

In this chapter the longitudinal model of the DFB laser was presented. Although it is difficult to separate the longitudinal part from the transverse part, for logical progress in the presentation it was separated as such. The model is based on the coupled mode theory for corrugated structures and is formulated in the spectral domain. The total power is obtained by integrating the spectral power. This alleviates the need to handle the conceptually difficult idea of a *mode* along the longitudinal direction. The capability of the model to handle spatial hole burning, lasing spectra and L-I curves was demonstrated through a few examples.

Chapter 3

Distributed Feedback Lasers: Transverse Model

3.1 Introduction

In this chapter the transverse two-dimensional model of the DFB laser is presented. In addition to the two-dimensional optical model, it also includes lateral diffusion of minority carriers, lateral drift of majority carriers, and recombination due to linear, bimolecular and Auger mechanisms. Following the approach of Stern and Xu [85], the optical mode profile is represented using a non-uniform-mesh finite-difference scheme and solved using the iterative inverse-power method.

3.2 Two-Dimensional Optical Model

Consider the eigen value equation (2.5) in chapter 2:

$$\hat{H}_t \mathbf{E}_n(x,y) = \left[\beta_n^2 - k^2\eta^2(x,y)\right]\mathbf{E}_n(x,y). \tag{3.1}$$

The two-dimensional optical model discussed in this chapter concerns the solution of this equation for arbitrary complex refractive index distributions $\eta(x,y)$. When cast in a convenient form for finite-difference implementation, equation (3.1) becomes:

$$P_{ii}E_{i,n}(x,y) + P_{ij}E_{j,n}(x,y) = 0 \tag{3.2}$$

where i and j denote the $\hat{x}$ and $\hat{y}$ polarizations of the field. The P_{ii} and P_{ij} terms can be shown to be:

$$\begin{aligned} P_{ii}E_{i,n}(x,y) &= \frac{\partial}{\partial i}\left[\frac{1}{\eta^2(x,y)}\frac{\partial \eta^2(x,y)\,E_{i,n}(x,y)}{\partial i}\right] + \\ &\quad \frac{\partial^2 E_{i,n}(x,y)}{\partial j^2} + \left(\eta^2(x,y)\,k^2 - \beta^2\right)E_{i,n}(x,y) \qquad (3.3) \\ P_{ij}E_{j,n}(x,y) &= \frac{\partial}{\partial i}\left[\frac{1}{\eta^2(x,y)}\frac{\partial \eta^2(x,y)\,E_{j,n}(x,y)}{\partial j}\right] - \\ &\quad \frac{\partial^2 E_{j,n}(x,y)}{\partial i \partial j}. \qquad (3.4) \end{aligned}$$

By choosing to implement a semi-vectorial approach, the P_{ij} cross terms can be neglected retaining only the P_{ii} terms. The ridge waveguide structures considered in this thesis are only weakly guiding along the lateral direction. As a result, a semi-vectorial approach should suffice.

The two-dimensional space (x,y) is discretized into a non-uniform mesh to accurately take the intensity distribution of the optical field into account. Initially, a trial field distribution $E_{i,n}^{(0)}(x,y)$ and an estimated propagation constant $\beta^{(0)}$ are assumed. In the notation used here, the (0) stands for the 0-th (initial) iteration. Using the initial solution, iterative improvements to the eigen equation (2.5) are sought by standard LU decomposition and back-solving. A given solution $E_{i,n}^{(p)}(x,y)$ is refined to $E_{i,n}^{(p+1)}(x,y)$ by solving for a linear equation of the form:

$$\hat{A}_i E_{i,n}^{(p+1)}(x,y) = \beta^{(p)^2} E_{i,n}^{(p)}(x,y)/M. \tag{3.5}$$

The constant M is chosen to normalize $E_{i,n}^{(p)}$ so that its largest element is equal to unity. The iterative solution of equation (3.5) will converge to the eigen value β^2 and its corresponding eigen vector $E_{i,n}$. The final value of β^2 will be closer to the initial estimate $\beta^{(0)}$ than any other eigen value of this matrix. Therefore, any required transverse mode of the structure can be calculated by choosing a suitable value for the initial estimate $\beta^{(0)}$. This technique is known as the *Inverse Power Iteration Method* and is adequately described in [85].

A transparent boundary condition (TBC) is used at the computational window boundaries. This enables one to reduce the computational window size without introducing any unphysical reflections off the computational window boundaries.

The complex optical mode $\mathbf{E}(x,y)$ and its effective index η_{eff} are initially solved for given injection current around which the d.c. solution is sought. For small variation in injection current around this operating point, the variation in effective index is found by using the following perturbative approach:

$$\eta_{\text{eff}}'^2 = \eta_{\text{eff}}^2 + \langle \mathbf{E}(x,y) | 2\eta(x,y)\,\Delta\eta(x,y) | \mathbf{E}(x,y) \rangle . \tag{3.6}$$

3.3 Lateral Carrier Model

The cross section of a ridge waveguide laser depicting the flow of carriers is shown on figure 3.1. The current is injected from the top of the ridge contact. The junctions are located on both sides of the active region below the ridge structure.

The two-dimensional flow of carriers in this structure is governed by the drift-diffusion and Poisson's equations. However, several approximations can be made to greatly simplify this picture and to reduce it to an approximate one-dimensional

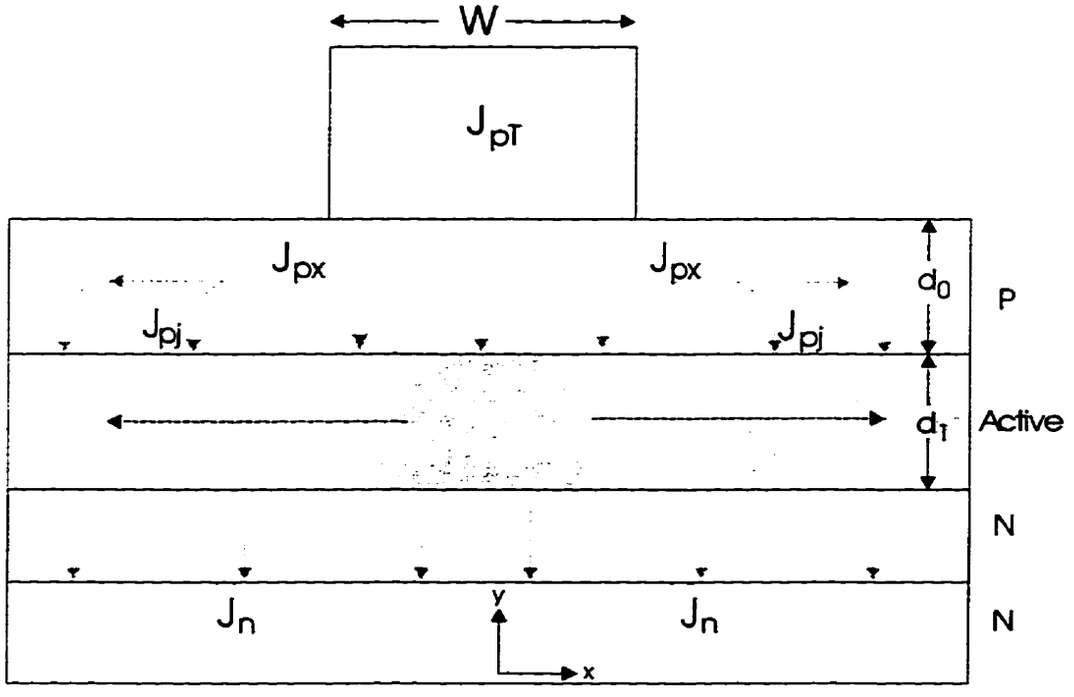

Figure 3.1: The lateral transport of carriers in the ridge waveguide DFB laser due to drift and diffusion.

model. This can be done by identifying the regions where the transport is primarily due to drift or diffusion.

As shown on figure 3.1, electrons injected into the active region flow upwards and laterally. Similarly, holes injected from above will flow downwards and laterally. Since the active region is typically undoped, this region can be treated as being ambipolar and essentially charge neutral. Further, since the width of the active region is much smaller than the ambipolar diffusion length, carrier diffusion will primarily occur along the lateral direction. The recombination processes in the active region will be dictated by the linear, bimolecular and Auger mechanisms. In addition, there will be recombination due to stimulated emission in the active region.

The recombined electrons flow as majority hole drift current on the p-side. This is aided by the voltage profile that exists along the x-direction. The finite sheet resistance of this layer causes the applied voltage within the width d_0 to decay along the x direction due to the flow of this lateral drift current. Similarly, there will be another current term due to the hole injection from the p-side. The combination of the drift and diffusion terms will characterize the electron carrier profile in the active region.

3.3.1 Carrier Transport in the Upper GRINSCH Region

Referring to figure 3.1, consider the voltage $V(x)$ on the p-side of the junction. Directly under the ridge ($|x| < w/2$) this voltage distribution will be constant and equal to the applied voltage on the ridge contact. Away from the ridge ($|x| > w/2$), it will vary as a function of x. It will be assumed that the n-side is relatively highly doped and grounded so that there is no variation in voltage on the n-side. As a result, the diode junction voltage will be equal to $V(x)$. There are two sources of majority

carrier current on the p-side: one supplementing for the recombination of electrons injected from the n-side, $J_{p1x}(x)$, and the other supplying holes for injection into the active region, $J_{p2x}(x)$. In addition, there will be a current component due to stimulated emission $J_{st}(x)$. It will be assumed here that $J_{st}(x)$ has a constant non-zero value directly under the ridge and zero elsewhere. This is a reasonable assumption since the overlap of the gain and the optical intensity profile is typically confined to the area under the ridge. This is tantamount to neglecting the effects of transverse spatial hole burning. Transverse spatial hole burning is not expected to play a major role in narrow ridge devices. This is especially true at low injection currents. Even at high injection currents its effects can usually be included in the gain compression factor ϵ. Further, the analysis done in chapters 4 and 5 are at threshold or slightly above threshold. As a result, the effects of transverse spatial hole burning will be neglected in this work.

Outside the ridge ($|x| > w/2$), the following equations can be written:

$$d_0 \frac{dJ_{p1x}(x)}{dx} = -J_s e^{V_x(x)/V_t} \tag{3.7}$$

$$d_0 \frac{dJ_{p2x}(x)}{dx} = -R(x) \tag{3.8}$$

where J_s is the diode saturation current, V_t is the thermal voltage, and $R(x)$ is due to the recombination of electrons in the active region. The voltage $V(x)$ along x is determined by the resistivity ρ_x of the p-doped layer:

$$\frac{dV_x(x)}{dx} = -\rho_x J_{px}(x) \tag{3.9}$$

where

$$J_{px}(x) = J_{p1x}(x) + J_{p2x}(x). \tag{3.10}$$

Further, since $n(x) \approx p(x)$ in the active region, it will be assumed that

$$R(x) \approx J_s e^{V_x(x)/V_t}. \tag{3.11}$$

Combining (3.7) - (3.10) results in:

$$\frac{d^2 J_{px}(x)}{dx^2} = -\frac{\rho_x J_{px}(x)}{V_t}\frac{dJ_{px}}{dx}. \tag{3.12}$$

This second order differential equation can be easily solved. The solution is:

$$J_{px}(x) = \frac{J_{px}(w/2)}{1 + x/L_o} \tag{3.13}$$

where

$$L_o = \frac{2V_t}{\rho_x J_{px}(w/2)}. \tag{3.14}$$

From this, the injection current $J_{pj}(x)$ into the diode can be found:

$$J_{pj}(x) = -\frac{dJ_{px}(x)}{dx}d_0 = \frac{J_{px}(w/2)\, d_0}{L_o\left(1 + (x - w/2)/L_o\right)^2}. \tag{3.15}$$

At $x = w/2$, the injected current is

$$J_{pj}(w/2) = \frac{J_{px}^2(w/2)\,\rho_x d_0}{2V_t}. \tag{3.16}$$

Since the voltage is maintained at V between $-w/2 < x < w/2$, the injected current in that region will be equal to $J_{pj}(w/2)$. For $|x| > w/2$ the injected current will vary as $J_{pj}(x)$ as given by equation (3.15). Further, since the stimulated emission current J_{st} was assumed to exist only under the ridge, this term has to be acounted for in $J_{pj}(w/2)$. Above threshold, the carrier density and voltage are clamped at their threshold values. As a result, J_{st} can be added to $J_{pj}(w/2)$ without affecting the diode voltage. The total injected current can then be expressed as

$$\begin{aligned} I_{nst} &= J_{pt} w \\ &= \left[J_{pj}(w/2) + J_{st}\right] w + 2J_{px}(w/2)\, d_0. \end{aligned} \tag{3.17}$$

Substituting for $J_{pj}(w/2)$ gives a quadratic expression in terms of $J_{px}(w/2)$. The solution for $J_{px}(w/2)$ will then be

$$J_{px}(w/2) = \frac{\sqrt{4d_0^2 + 2K'(I_t - I_{st})} - 2d_0}{K'} \tag{3.18}$$

where

$$K = \frac{w\rho_x d_0}{V_t}. \tag{3.19}$$

This completely determines the injection current profile $J_{pj}(x)$.

3.3.2 Carrier Transport in the Active Region

The minority electron carrier profile in the active region is dictated by the continuity equation

$$\frac{dJ_n(x)}{dx} = G(x) - R_{nst}(x) - R_{st}(x). \tag{3.20}$$

The volume generation rate $G(x)$ is given by

$$G(x) = \frac{J_{pj}(x)}{d_1} \tag{3.21}$$

and the recombination $R_{nst}(x)$ can be written as

$$R(x) = q\left[An(x) + Bn^2(x) + Cn^3(x)\right] \tag{3.22}$$

where A, B and C are the linear, bimolecular and Auger recombination coefficients respectively [86, 87, 88]. $R_{st}(x)$ is the stimulated recombination rate. From the previous section,

$$R_{st}(x) = \frac{J_{st}}{d_1} \text{ for } |x| < w/2 \tag{3.23}$$

$$= 0 \text{ elsewhere.} \tag{3.24}$$

Assuming dominantly diffusive currents, the governing equation for carriers in the active region becomes:

$$qD\frac{\partial^2 n(x)}{\partial x^2} = \frac{J_{pj}(x)}{d_1} - q\left[An(x) + Bn^2(x) + Cn^3(x)\right]. \tag{3.25}$$

D in the above expression is the ambipolar diffusion constant given by

$$D = \frac{2D_pD_n}{D_p + D_n}. \tag{3.26}$$

This non-linear equation can only be solved numerically using iterative techniques. An initial estimate of the carrier profile is used to estimate the carrier lifetimes as:

$$\frac{1}{\tau(x)} = A + 2Bn(x) + 3Cn^2(x). \tag{3.27}$$

The resulting second order differential equation is

$$qD\frac{\partial^2 n(x)}{\partial x^2} = \frac{J_{pj}(x)}{d_1} - q\frac{n(x)}{\tau(x)}. \tag{3.28}$$

Since B is the radiative coefficient and A and C are non-radiative coefficients, the spontaneous emission and non-radiative currents can be calculated from the resulting carrier profile $n(x)$ as follows [89]:

$$I_{sp} = \int_x Bn^2(x)\,dx \tag{3.29}$$

$$I_{nr} = \int_x \left(An(x) + Cn^3(x)\right)dx \tag{3.30}$$

with

$$I = I_{sp} + I_{nr} + I_{st}. \tag{3.31}$$

3.3.3 Interaction of Transverse Gain and Optical Profiles

The overlap between the gain profile and the optical mode profile determines the one-dimensional quantity $\Im\{\eta_{\text{eff}}\}$ through equation (3.6). The gain profile is used for calculating the complex perturbation quantity $\Delta\eta(x,y)$. As a result, it is not the transverse carrier profile, but the overlap between the gain and the optical profiles which is the important quantity.

On figure 3.2 the calculated transverse profiles for a 2.0μm ridge waveguide laser at the onset of threshold are shown. Shown are: injection profile $J_{pj}(x)$, electron carrier profile $n(x)$. gain profile $2k\Im\{\eta\}$ and the optical field profile $E(x)$. The vertical units have been arbitrarily scaled to unity for the purpose of clarity. Note that the extent of the carrier profile is much greater than the optical profile. This is the observation that leads to the idea of leakage current. However, note that the extent of the gain profile. though still greater than the optical mode profile, is much closer to the optical mode profile.

On figure 3.3a the carrier profiles in a 3.0μm, 1.2μm and a 0.6μm wide ridge laser are shown at the onset of threshold. Note that despite all other device parameters being equal, the peak carrier density in the 0.6μm device is higher than in the 3.0μm device. This is purely a two-dimensional effect. In a one-dimensional model the carrier density will typically be considered to be constant at the threshold value for all ridge widths. In addition, the coupling coefficients for figure 3.3 are calculated from the two-dimensional field profile from equation 2.21. These values are 55.1/cm, 61.7/cm and 66.0/cm for the 0.6μm, 1.2μm and 3.0μm wide ridges respectively. The two-dimensional interaction between the gain and optical profiles can be understood from 3.3b. For the 3.0μm device the optical field is well contained within the ridge, therefore most of the injected current contributes to the modal gain. In the 0.6μm device a significant fraction of the optical field outside the ridge. As a result, the peak gain under the ridge has to be higher to produce the same threshold modal gain.

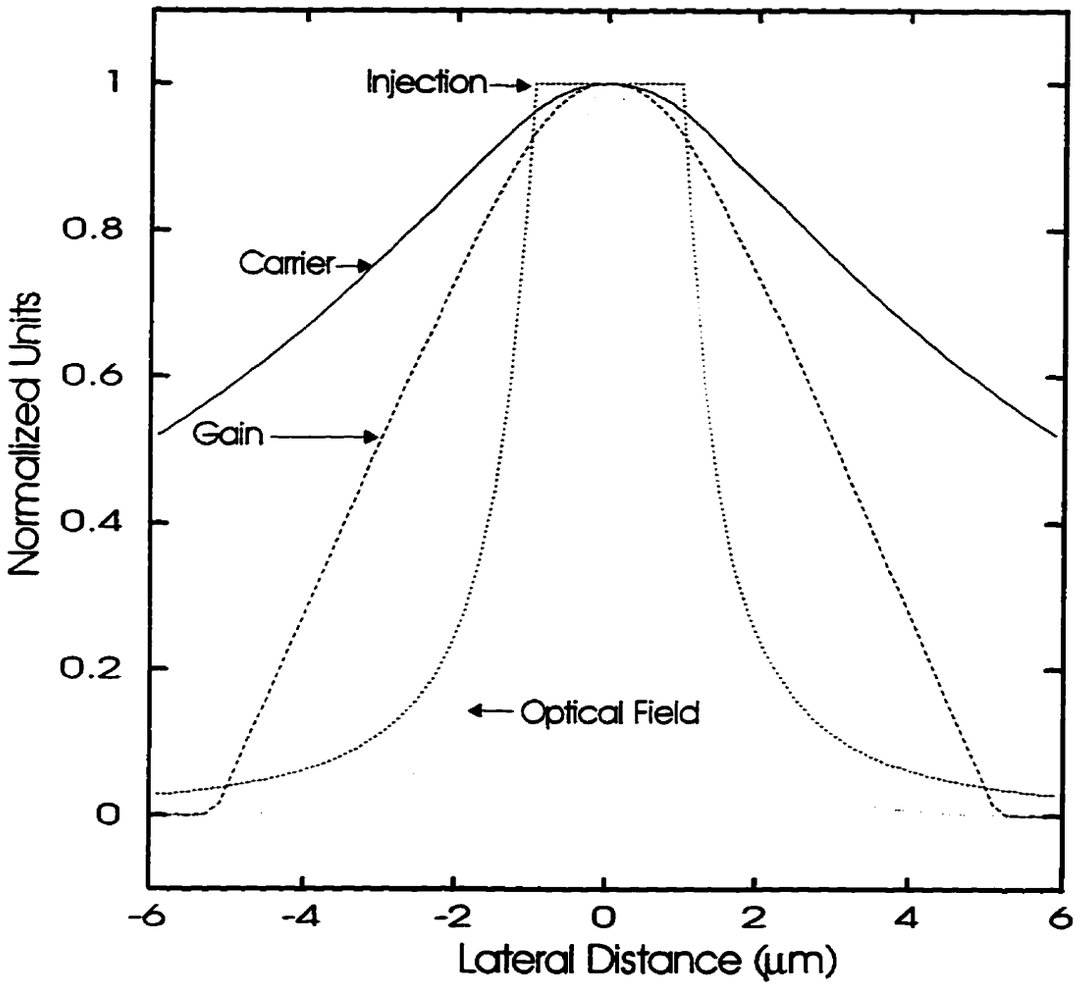

Figure 3.2: Lateral distribution of the injection current $J_{pj}(x)$, carrier density $n(x)$, gain profile $2k\Im\{\eta\}$, and the optical field profile $E(x)$ for a 2.0μm wide ridge laser at the onset of threshold. The following parameters were assumed: $A = 2.5 \times 10^8/s$, $B = 1.0 \times 10^{-10}\text{cm}^3s^{-1}$, $C = 3.0 \times 10^{-29}\text{cm}^6s^{-1}$, $a_o = 1000.0/\text{cm}$, $d_0 = 180.0\text{nm}$, $d_1 = 20.0\text{nm}$, $N_A = 6.0 \times 10^{17}\text{cm}^{-3}$, $\mu_p = 100.0\ \text{cm}^2V^{-1}s^{-1}$, $\mu_n = 6000.0\ \text{cm}^2V^{-1}s^{-1}$. The two-dimensional optical field is calculated from the detailed DFB structure shown on figure 4.1. The vertical scales have been arbitrarily scaled to unity.

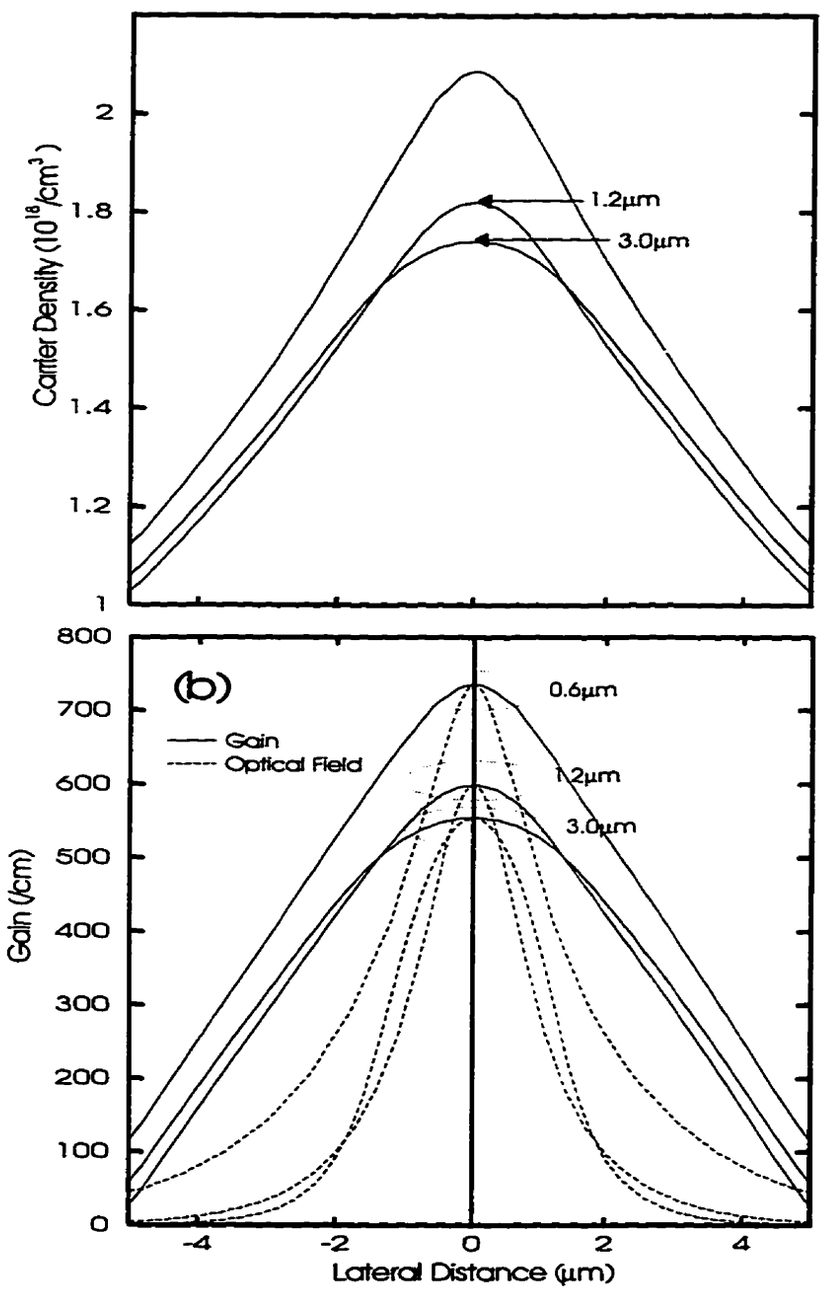

Figure 3.3: (a) Carrier profiles and (b) gain and optical profiles in 0.6μm, 1.2μm and 3.0μm ridges at the the onset of threshold. All parameters used for the simulation are given in figure 3.2.

3.4 Lateral Leakage Current Model

Lateral leakage current is loosely defined as the the current that "leaks" away from the ridge along the lateral direction. This increases the threshold current as well as the operating temperature of the device. Unlike in buried hetero-structure (BH) DFB lasers, the lack of lateral current confinement, the weak lateral optical confinement and the higher thermal impedance in Ridge Waveguide DFB lasers is believed to be reponsible for the degradaton in its performance.

Leakage current has been defined in various ways by several authors. The most commonly used definition of leakage current is as the total recombination current outside the ridge width [90]:

$$I_L = 2\int_{w/2}^{\infty} R(x)\,dx. \tag{3.32}$$

Inherent in this definition is the assumption that the optical field is uniformly and completely confined under the ridge width. Strictly speaking, this assumption is not correct because there is always a finite field intensity outside the ridge width, especially in narrow width ridges. Alternatively, one can also define leakage current as the recombination current outside the positive gain profile [61]. Although slightly more realistic, this assumption also breaks down for small ridge widths. In all these definitions the two-dimensional nature of the optical field has not been considered.

In Ridge Waveguide DFB lasers, the weak lateral optical confinement leads to a finite optical power outside the ridge width. As a result, some of the current that flows laterally away from the ridge can actually help *reduce* the threshold current. Using the above definition of leakage current, one might erroneously conclude that the threshold current of the device can always be reduced by reducing the lateral drift and diffusion components. Although this is true in most cases, it fails for

ridge waveguides smaller than about 1.0μm. A correct description of leakage current should include the field profile *and* the gain profile simultaneously. Therefore, instead of defining a leakage current, it is more convenient study the *change* in the threshold current for a give change in the design parameter. This is the approach that will be taken here.

3.4.1 Threshold Current and GRINSCH Layer Properties

On figure 3.4 the effect of increasing the GRINSCH layer resistance *and* reducing its diffusion coefficient is shown. For the large ridge devices, as the lateral spreading is reduced the threshold current decreases. However, for the narrow ridge devices, the threshold current starts to increase if the lateral spreading is reduced too much. This is due to the diminishing overlap between the gain profile and the optical profile as the gain profile is confined more and more under the ridge. As a result, it can be seen that lateral current spreading, which is typically defined as the leakage current, actually helps reduce the threshold current in narrow ridge devices.

3.5 Conclusions

In this chapter, the transverse two-dimensional optical model of the DFB laser and the lateral carrier model were described. The optical mode is solved by the inverse power iteration method. Current flow due to drift in the GRINSCH layer and diffusion in the active region were taken into account to predict the lateral carrier profile. The interaction between the optical and gain profiles determines the modal gain. The interaction between the optical profile and the etched regions determines the coupling coefficient. These are the one-dimensional quantities which are then

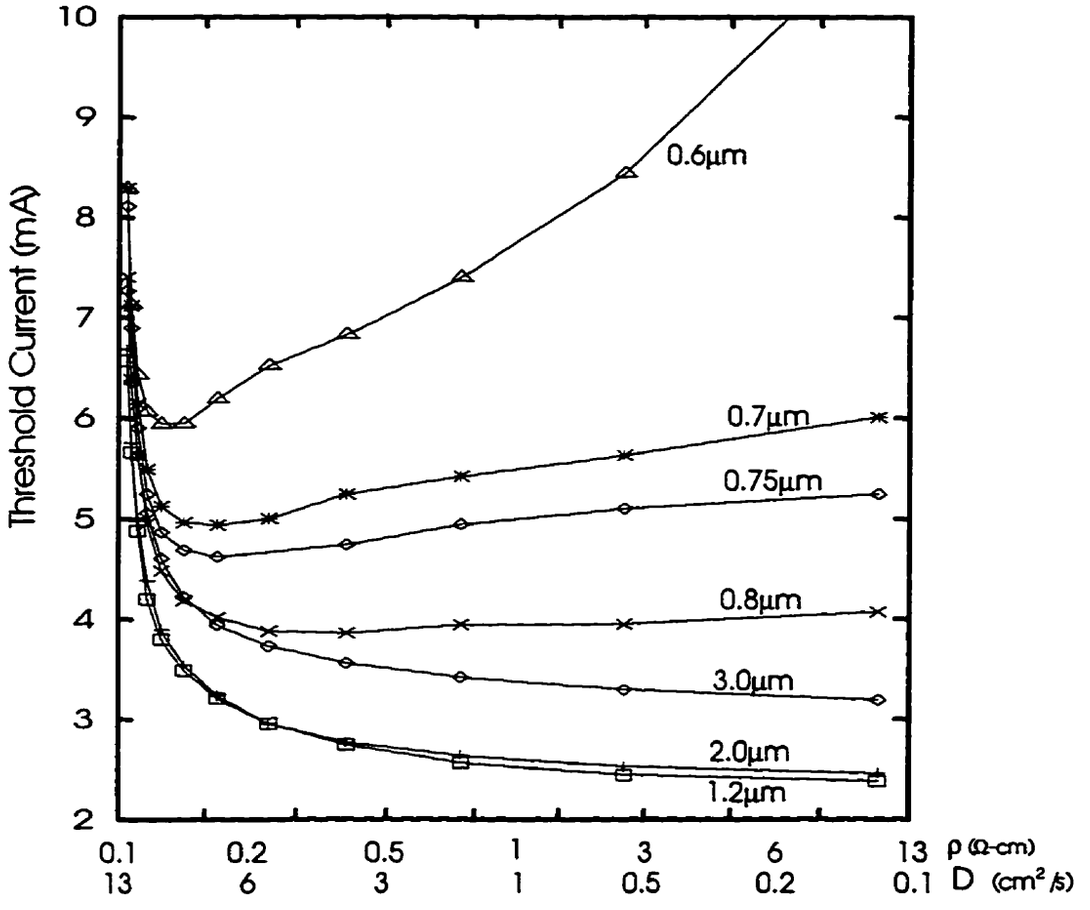

Figure 3.4: Reduction of threshold current by increasing the GRINSCH layer resistance and reducing the electron diffusion coefficient in the quantum wells for different ridge width DFB lasers.

used in the longitudinal model of the DFB laser.

The change in threshold current with different GRINSCH layer resistivity and diffusion constants was studied. As a result, it was shown that the conventional definition of leakage current is inadequate because it does not take the two-dimensional nature of the optical field into account.

Chapter 4

Varying Ridge Width Laser Array

4.1 Introduction

A simple method for realizing wavelength control in DFB laser arrays is by varying the modal index of the waveguide structure. Although the modal index varies somewhat with injection current, sufficiently large shifts in modal index can be obtained by controlling the structure of the ridge waveguide.

The vertical structure of the ridge is determined by the thicknesses of the various epitaxially grown layers. Since the growth is a uniform process, it is not practical to control the vertical structure between adjacent elements of a laser array. Such an approach would require a fairly involved selective area epitaxial (SEA) techniques [39. 40]. The lateral dimensions of the ridges, however, are defined after the epitaxial growth phases. Conventional photo-lithography and dry-etch are used for the ridge definition. As a result, it is much easier to control the ridge width than it is to control the ridge height or the SCH layer thicknesses.

The deign concept of the multi-wavelength laser array presented in this chapter

is based on sequentially incrementing the ridge widths of the waveguides. In the literature, the main concern in using such a scheme has been over potential mode instabilities and/or multi-transverse mode oscillation of the lasers. As a result the few authors who have studied this scheme had restricted their attention to a narrow range of ridge width variation within which the waveguide was single moded. Naturally, this resulted in a very small tuning range of about 2nm. This is too small to be of much practical value. Although it is reasonable to expect that wider ridge waveguides will be able support higher order transverse modes, all the elements in the laser array designed for this experiment continued to lase in the fundamental transverse mode. This condition was observed even for ridges that were calculated to be wide enough to support multiple transverse modes. As a result it became possible to demonstrate a tuning range of roughly 8nm while still maintaining single mode operation. In this chapter the reasons for this transverse mode discrimination and their limitations are explained.

4.2 Device Description

On figure 4.1 the epitaxial growth sequence and the transverse ridge waveguide structure of an index coupled DFB wafer is shown. Quartenary SCH layers including eight quantum wells and barriers were grown on an InP substrate. The gratings (shaded regions) were produced by holographic exposure followed by an etch and re-growth process. The re-grown material was InP. This provided sufficient contrast between the etched quartenary material and the re-grown material. The ridge waveguides were processed using standard photo-lithography, dry-etch and a wet-etch finish. The ridges were coated with Au metalization and patterned using the lift-off process.

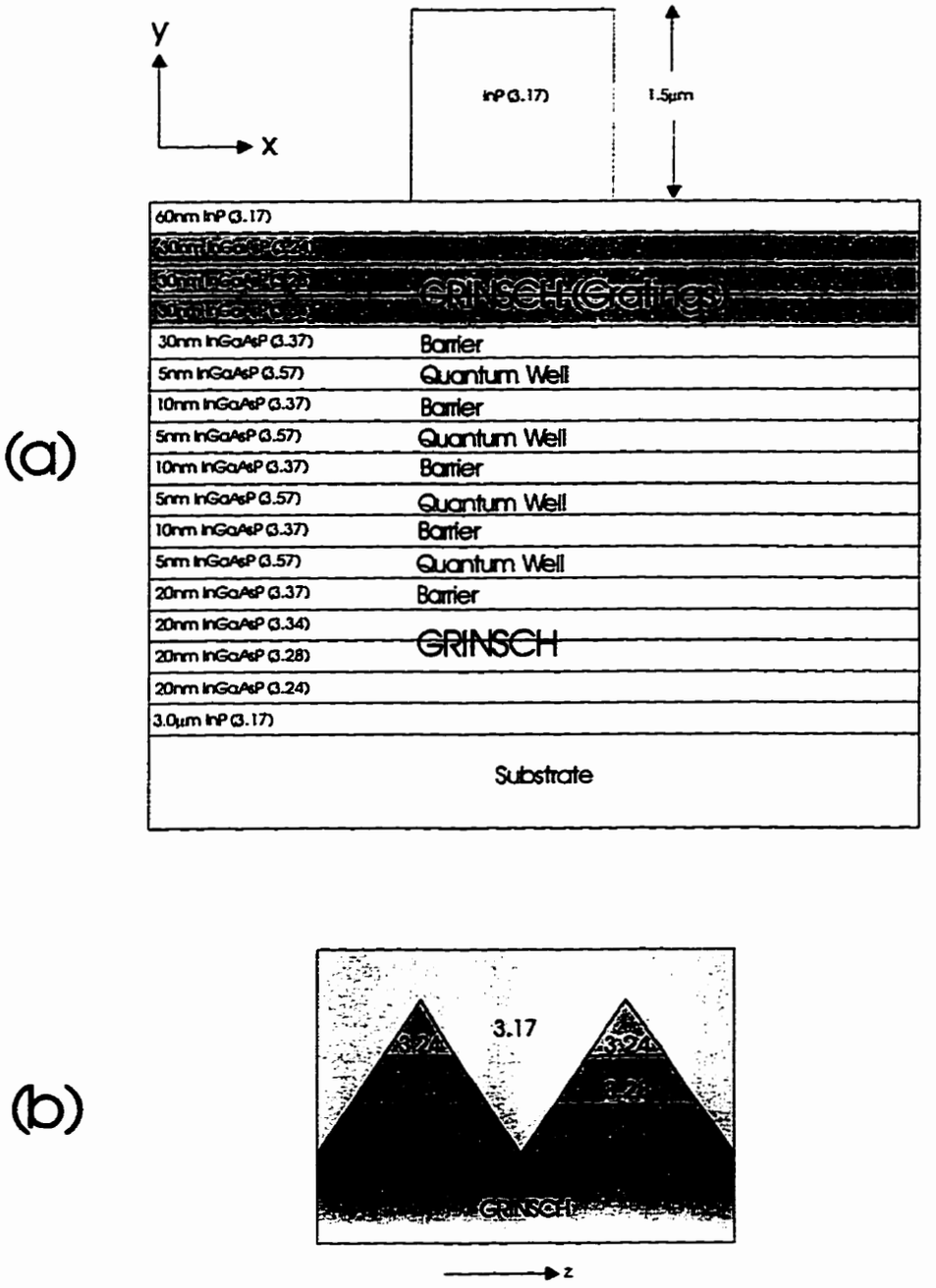

Figure 4.1: Layer structure of the index-coupled DFB laser.

A chip photograph of the laser array after processing, die-bonding and wire-bonding is shown on figure 4.2. On each array a total of sixteen elements were designed with an element spacing of 250μm. The ridge widths were varied from 1.6μm to 5.2μm in 16 incremental steps. The front facets were 5% AR coated and the rear facets were as-cleaved.

On each element a thin film of Ti was deposited and patterned close to the active region to provide extra tuning functionality. Controlled thermal dissipation from the Ti film resistor can provide a wavelength red-shift of as much as 0.65nm as a post-processing feature [64, 65]. A detailed discussion on the Ti film thermal tuning is not included in this thesis.

4.3 Single Transverse Mode Operation

The modal index of the structure is determined by the width of the ridge as well as the refractive indices and thicknesses of each epitaxial layer. A proper analysis of this structure requires a full two-dimensional mode solution. The two-dimensional semi-vectorial iterative formulation of Maxwell's equation described in chapter 3 was applied to these structures to solve for the complex optical modes as well as their effective indices. The index profile of figure 4.1 was optimally discretized into a non-uniform mesh allowing for finer resolution in the waveguide core and coarser elsewhere.

The calculated effective indices of the structure for the various modes as a function of ridge width is shown on figure 4.3. Both the $\hat{x}$ and the $\hat{y}$ polarized fundamental modes exist when the ridge is 1.6μm (the polarization selectivity due to strain in the quantum wells will be ignored). When the ridge gets wider than about 2.2μm, additional modes start to appear. Beyond 2.2μm the waveguide behaves as

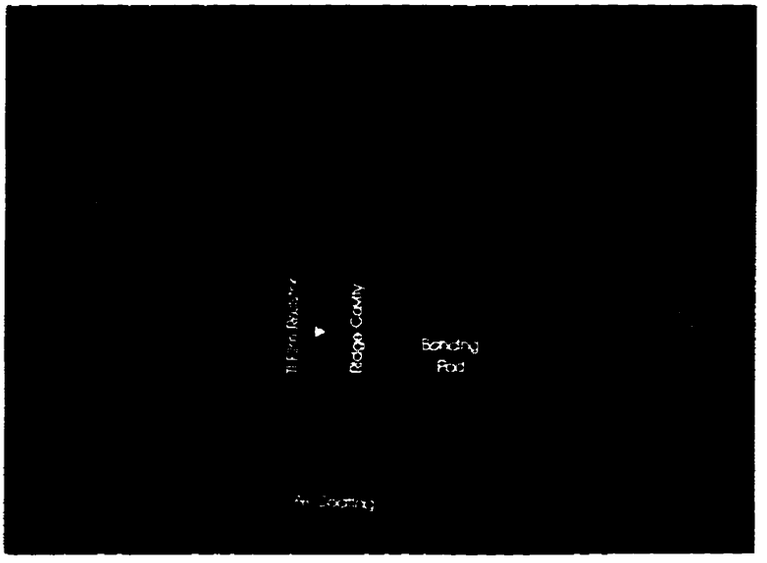

Figure 4.2: Chip photograph of the 16-element varying ridge width DFB laser array.

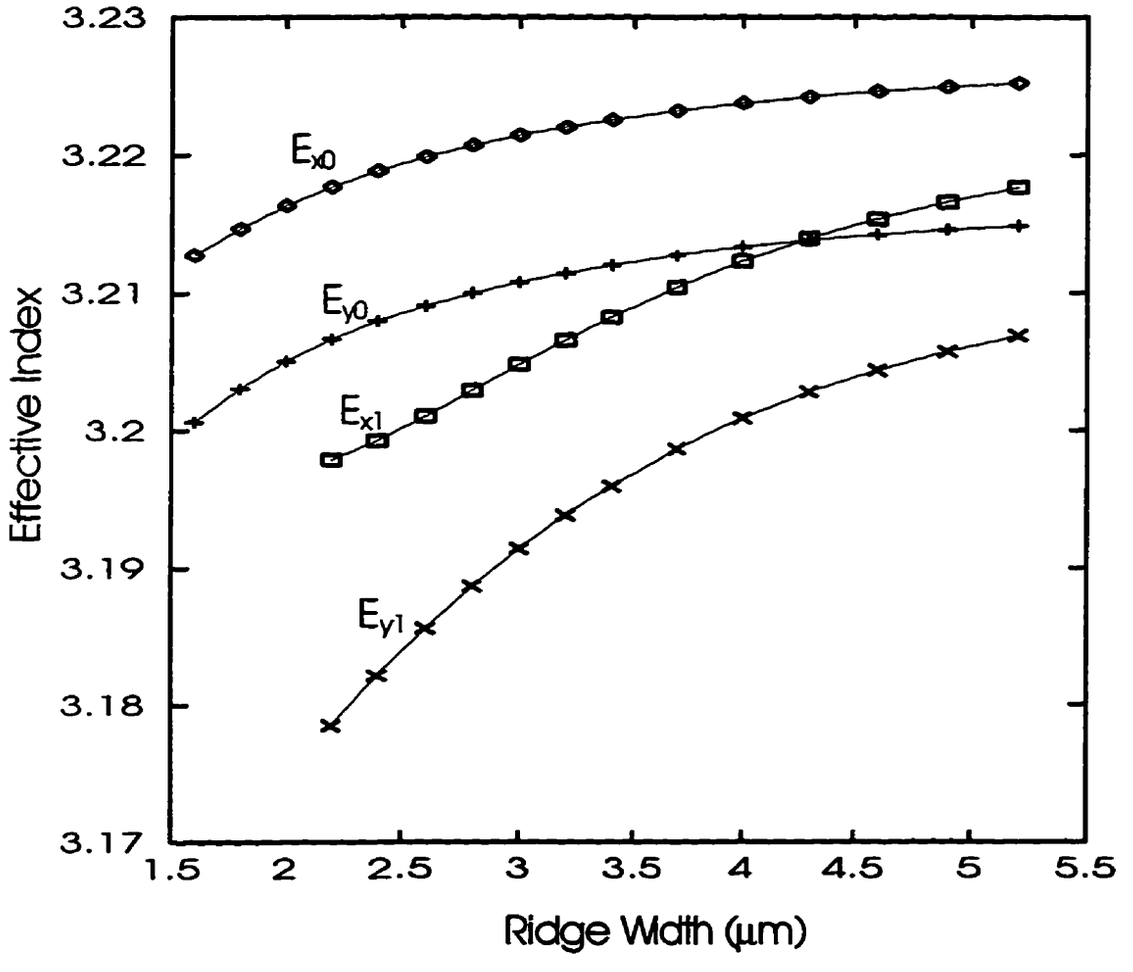

Figure 4.3: Calculated effective indices for the various transverse modes in the varying ridge width DFB laser array.

a multi-mode waveguide. In the DFB structure, a larger effective index will correspond to a longer lasing wavelength. As a result, one can expect a red-shift in wavelength as the ridge width is increased. Further, even though there are several transverse modes in the structure, lasing is always preferred along the E_{x0} mode. The reason for this becomes evident from figure 4.4.

Figure 4.4 shows how the coupling coefficient κ evolves as a function of ridge width for the various transverse modes. This was calculated using the two-dimensional mode profiles $\mathbf{E}(x, y)$ using the perturbative approach described by equation (2.21) in chapter 2. It can be seen that κ for the fundamental E_{x0} mode is larger than that of all other modes. As the ridge gets wider, this difference gets smaller. At infinity, the κ for all the $\hat{x}$ polarized modes will converge at one point and that of the $\hat{y}$ polarized modes will converge at a lower point. This can be understood if one thinks of an infinitely wide ridge waveguide as essentially a planar waveguide confined only along the y direction. Since there is no confinement along the x direction, the shape of all the lateral modes will be identical and uniform. Due to the confinement along the vertical direction, the $\hat{x}$ and $\hat{y}$ polarized vertical modes will have different mode shapes. The $\hat{y}$ polarized vertical mode will be more confined to the active region than the $\hat{x}$ polarized mode. Note that the gratings are in the SCH region *above* the active quantum wells (figure 4.1). As a result, the overlap of the $\hat{y}$ polarized mode with the gratings will be smaller, resulting in a smaller value of κ.

As the ridge gets wider, the value of κ also gets larger. This can be understood by considering the two extreme cases of a non-existent ridge and an infinitely wide ridge. In both cases, the waveguides approach the characteristics of a planar waveguide. In the first case, as a result of the lower refractive index of air compared to InP, the average optical intensity in the SCH layer will be smaller. In the second case, the optical intensity in the SCH laser will be larger. As a result, the coupling

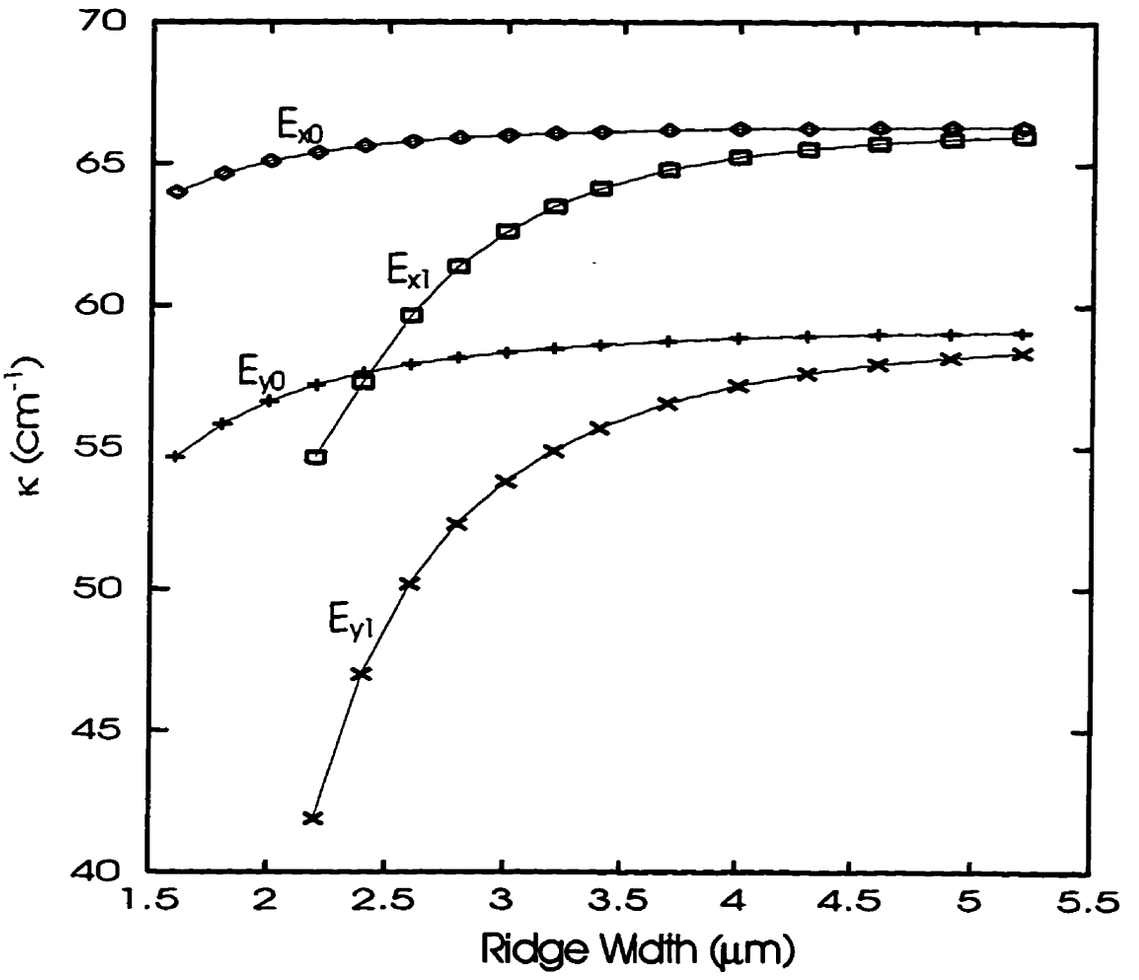

Figure 4.4: Calculated coupling coefficients κ_{mn} for the various transverse modes in the varying ridge width DFB laser array.

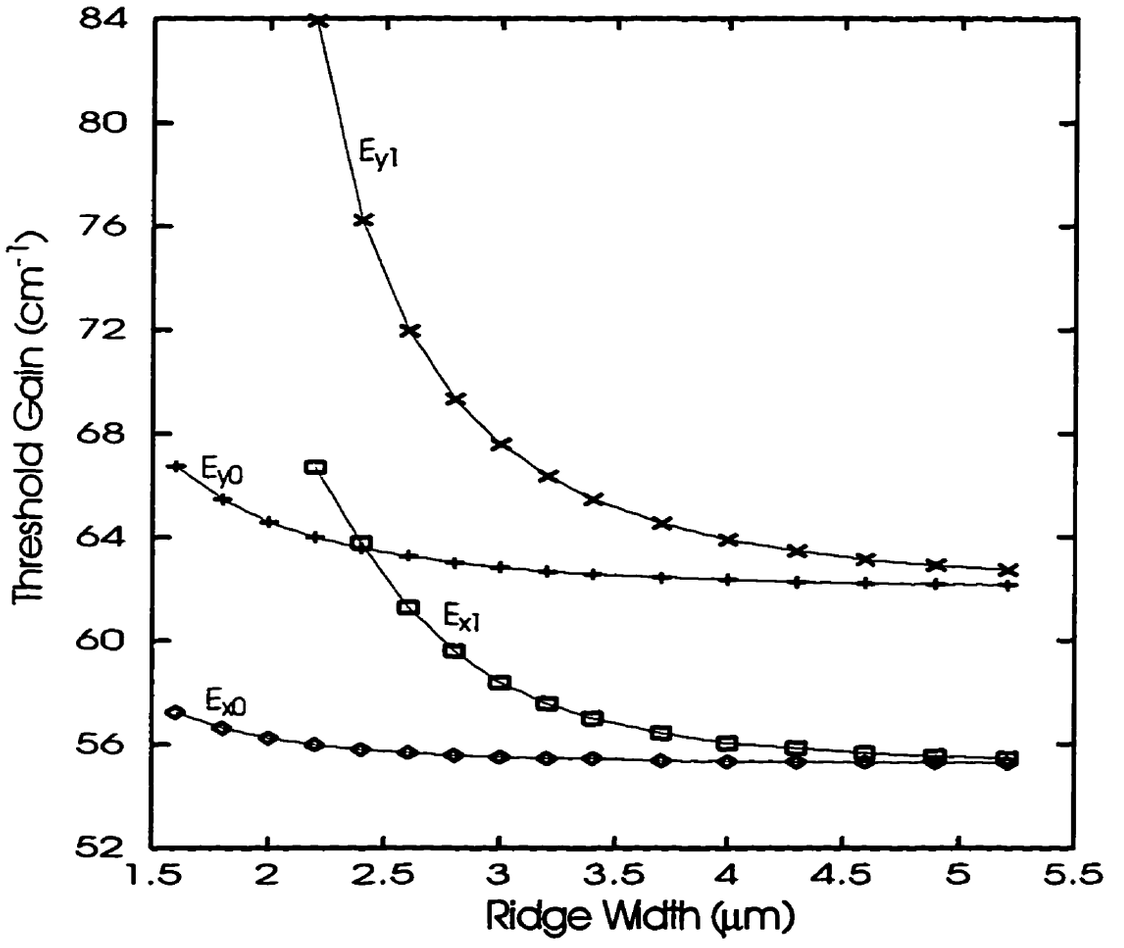

Figure 4.5: Calculated threshold gain for the various transverse modes in the varying ridge width DFB laser array. This curve was calculated using the coupling coefficients shown on figure 4.4.

improves marginally with increasing ridge width.

The threshold gains corresponding to the coupling coefficients shown on figure 4.4 for the various modes are shown on figure 4.5. For this calculation the cavity length was assumed to be 325μm with zero facet reflectivities. Consistent with figure 4.4 the E_{x0} mode has the lowest threshold gain ensuring single mode operation. The difference in threshold gains between the main mode and the side mode is largest for the smaller ridge widths. This difference progressively gets smaller for larger ridge widths. However, throughout the operating range, the E_{x0} mode has the lowest gain.

4.4 Lasing Wavelength Shift with Ridge Width

The calculated DFB mode wavelengths corresponding to the different transverse modes are shown on figure 4.6. Since the structure under consideration is an index-coupled laser, both ends of the DFB stop-band are shown. On the same figure, the measured results from the laser array are shown for comparison. The measured points can be seen to agree fairly well with the behaviour of the E_{x0} mode. This confirms the expectation of single mode oscillation along the E_{x0} mode. The experimental sample was 5% anti-reflection coated on one side and cleaved on the other. As a result, the symmetry of the two DFB lasing modes, which are otherwise degenerate, is removed. This can be identified from the random selection of the lasing mode around the DFB stop-band on figure 4.6. Further, the wavelength measurements were done at a current slightly above the threshold current of these lasers. The *total* threshold current in this array actually increases with ridge width although the threshold current ***density*** decreases. This decrease in threshold current density is due to the increase in κ with ridge width as shown on figure 4.4. The higher threshold current will cause the active region of the device to operate at a

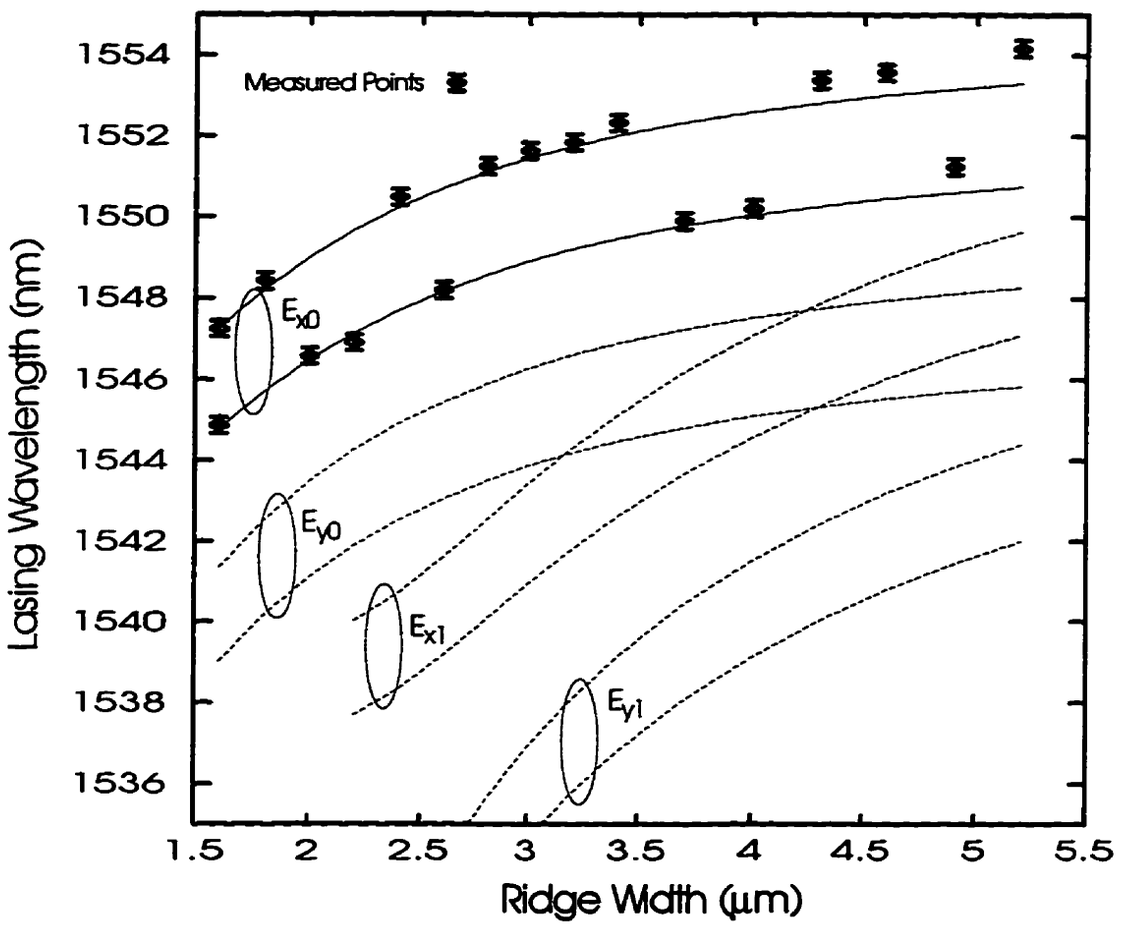

Figure 4.6: Calculated and measured wavelength vs ridge width is shown. The calculated lines correspond to all the transverse modes in the structure, but lasing takes place on the fundamental transverse mode only. The random selection of the lasing mode on either side of the DFB stop-band is due to the facet-phase uncertainty.

higher temperature. This will cause an extra red shift in the lasing wavelength. This is the reason the measured wavelengths exhibit a slight departure from the simulated curves towards longer wavelengths at larger ridge widths.

On figure 4.7 the spectrum of the 4.9μm wide ridge laser under direct small signal modulation is shown. The device was biased well above threshold at 70mA and modulated with an a.c small-signal sweep signal from 130 MHz to 20 GHz at a power level of -10 dBm. The arrows show the stop-band locations of the higher order E_{x1} and the E_{y0} modes. This is shown to demonstrate that the single mode lasing condition is maintained even under dynamic operation. The side mode suppression ratio (SMSR) is in excess of 40dB under modulation. Although the time averaged spectrum is single moded under direct modulation. the Bit Error Rate (BER) is actually a function of the threshold gain difference between the different modes. This error rate is related to the likelihood of momentary lasing along the mode with the lower threshold gain due to random fluctuations. However, a digital transmission test was not performed or studied as part of this work. A detailed model of the relationship between the side mode suppression ratio. threshold gain difference and the transmitted bit error rate can be found elsewhere [91, 92, 93].

4.5 Simultaneous Multi-Wavelength Demonstration of the Laser Array

A 16-wavelength gain-coupled DFB laser array was used in the demonstration of a four-channel WDM transmitter. To the best of the author's knowledge, this is the first such demonstration of a WDM transmitter using this approach.

On figure 4.8 the set-up of the experiment is shown. The 16-wavelength gain-

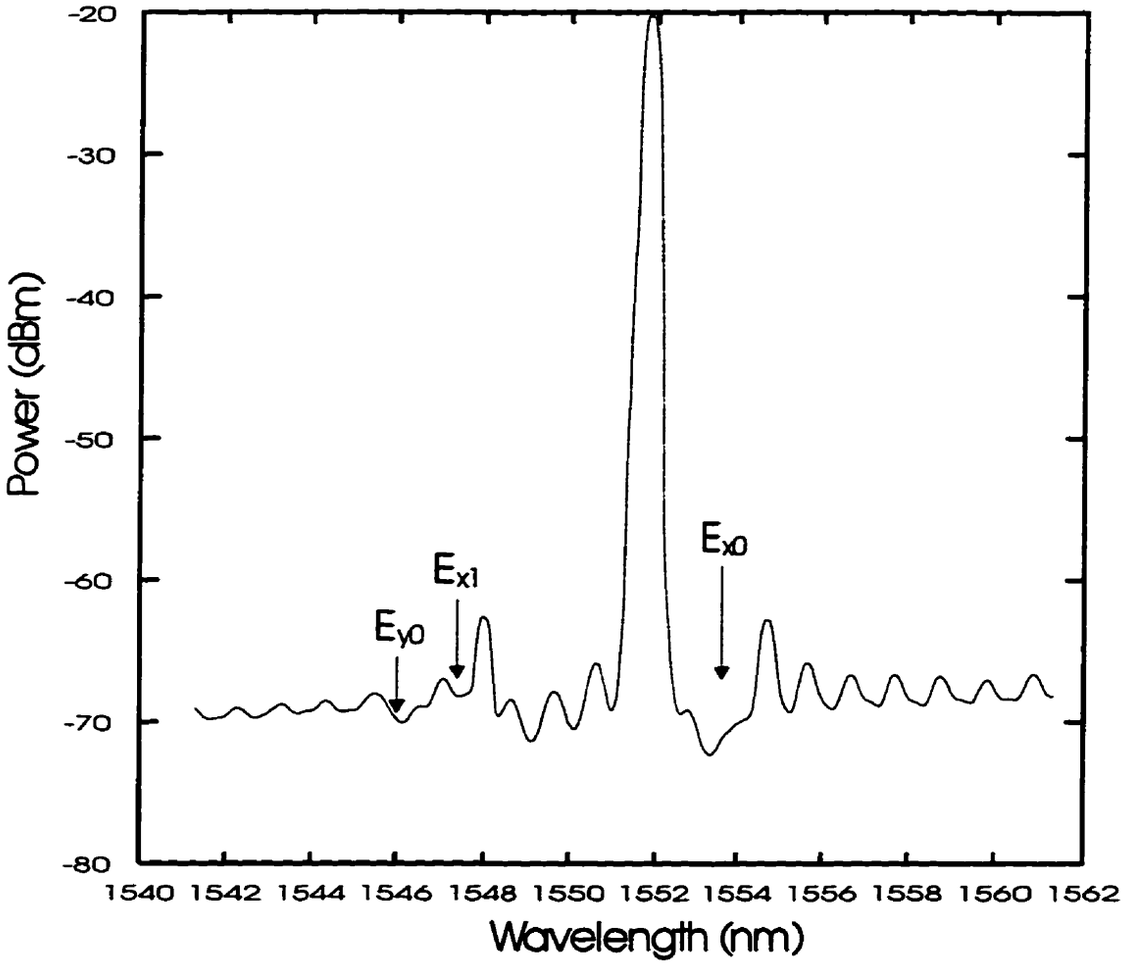

Figure 4.7: Spectrum of the 4.9μm wide ridge laser under small signal modulation. The arrows show the locations of the stop-bands corresponding to the higher order transverse modes.

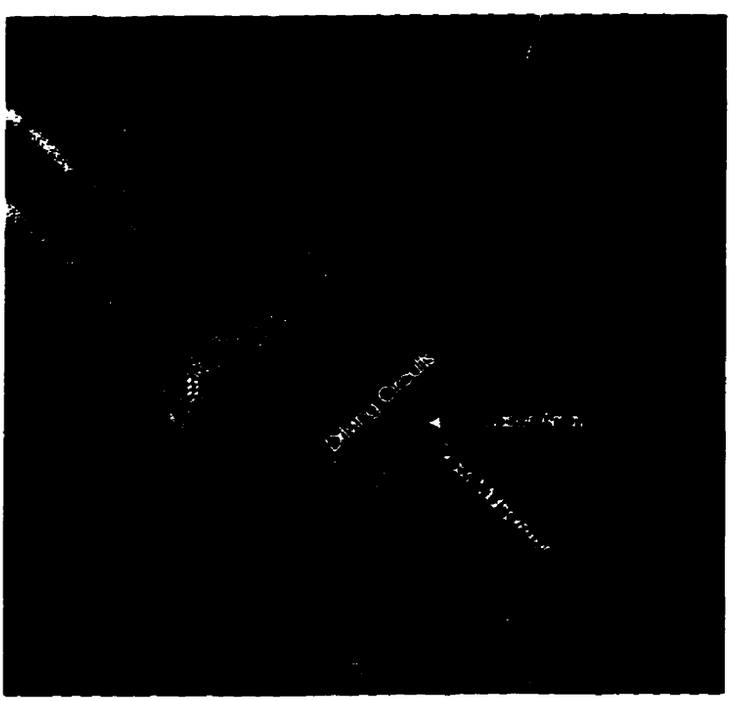

Figure 4.8: WDM experimental setup with the laser array, drivers and the glass waveguide multiplexer.

coupled DFB-laser array was mounted on a patterned-metal chip carrier on top of a heat sink and a thermo-electric cooler. Four parallel units of electronic integrated circuits containing the d.c. bias circuits, pulse-shaping and Ti temperature controllers were wire bonded to four pre-selected lasers on the array [94]. The choice of which lasers out of the sixteen are selected for bonding depends on the required channel separation. The output from the four lasers were directly coupled into a glass waveguide based multiplexer with a single pigtailed fiber output [95]. The glass waveguide array spacing was 250μm exactly matching the laser spacing on the array.

On figure 4.9 the spectrum from the simultaneous operation of four channels is shown. The bias current for each laser was set at about 40mA and slightly adjusted for equal coupled output power. Figure 4.9a shows the case of dense wavelength spacing of about 0.3nm These are from four devices with small ridge width variation selected from the eight devices that were coupled to the multiplexer. Figure 4.9b shows the measured spectrum from a selection of devices with larger ridge width variation. This results in a larger wavelength spacing between channels of about 1.2nm. This demonstrates the flexibility of the laser array to adapt for applications in either dense WDM or coarse WDM simply by re-wiring the circuit.

4.6 Conclusions

In this chapter the description of wavelength control using the varying ridge width approach in DFB laser arrays was given. It was shown for the first time that single mode operation is preserved even in ridge waveguides that are wide enough to support multiple transverse modes. As a result, it is possible to extend the useful tuning range to as high as 8nm. A 16 wavelength laser array using this approach

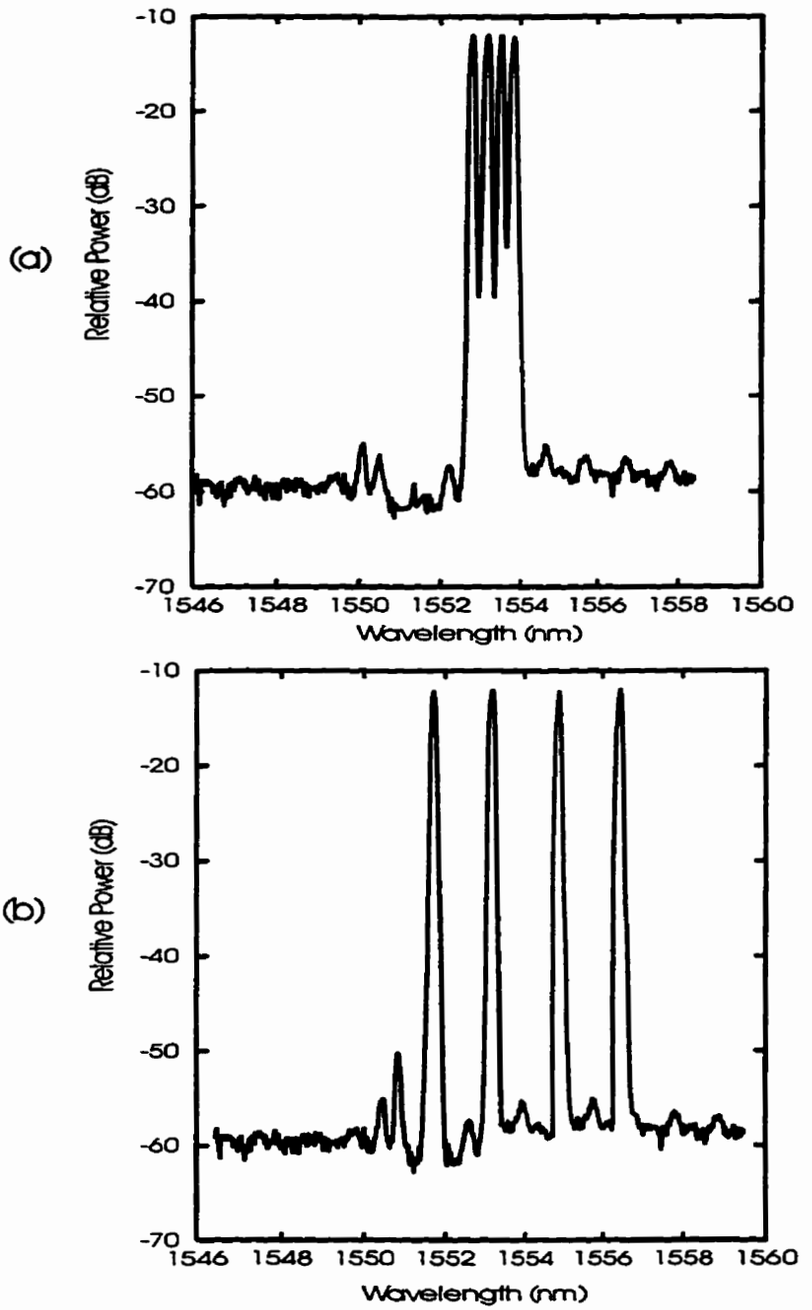

Figure 4.9: Demonstration of four wavelengths into a single fiber with the varying ridge width DFB laser array. The wavelength spacings are approximately (a) 0.3nm and (b) 1.2nm.

was designed, fabricated, measured and compared with the theoretical predictions from the DFB laser model developed in the earlier chapters. The results were found to be in good agreement with simulations. Simultaneous WDM operation of four pre-selected lasers was demonstrated at CW for both coarse and dense wavelength spacing using a hybrid assembly approach. This is the first such reported demonstration using the varying ridge width approach.

Chapter 5

Varying Ridge Tilt Laser Array

5.1 Introduction

It is well known that the lasing wavelength can be controlled by altering the grating pitch inside the DFB cavity. However, directly controlling the grating pitch is not simple, especially in a laser array configuration where the grating pitch variation has to be laterally across the chip. Direct E-beam writing [34, 35] and printed phase-masks [36, 37, 38] are two such schemes but they demand a fairly elaborate processing technology. From a reliability point of view it would be beneficial to consider a wafer with uniformly etched gratings using holography. The varying ridge width approach presented in chapter 4 is a simple scheme that takes advantages of this benefit. An alternate scheme, which is equally simple to implement, is to control the waveguide tilt with respect to the gratings. This effectively changes the grating pitch inside the cavity and provides a convenient means of controlling the lasing wavelength in DFB laser arrays.

As early as 1978, the wavelength tuning effects by tilting the pumping line in

optically pumped GaAs DFB lasers have been reported [96]. Others have discussed the effects of mis-aligned or curved gratings in waveguides [97, 98]. Recently, Tsang et. al. from AT&T reported experimental results from angled stripe gain-coupled DFB lasers [49]. So far, only the wavelength as a function of tilt angle has been investigated. This has been shown to roughly vary as $\lambda \sim 1/\cos\theta$. The effects of the coupling coefficient (κ) has been neglected or assumed to be insignificant. In [49] they allude to a slight decrease in κ with tilt angle. But yet they neglect its importance and erroneously attribute this to grating non-uniformities across the wafer. It has been found in this work that the decrease in κ with tilt angle is as significant as the dependence of wavelength itself. In fact, it was found that the increase in threshold current resulting from the decrease in κ is what ultimately limits the usable range of tilt angle in these lasers.

When the tilted ridge is wide enough to support multiple transverse modes several other interesting features also emerge. Since the tilt angle effectively introduces a transverse periodicity in the gratings, the selection of which transverse mode will oscillate greatly depends on this angle. Further, due to the variation in κ with tilt (and the associated variation in the DFB stop-band), the exact relationship of lasing wavelength with tilt will deviate from the simple $\lambda \sim 1/\cos\theta$ expression.

In addition to the control of lasing wavelength, tilted structures are also used for realizing other performance enhancements. In S-bend DFB lasers, for example, the tilt is used to improve the single mode yield and to reduce spatial-hole burning. So far in the literature the dependence of κ on tilt angle has been neglected or considered to be of minor importance [99, 100, 101, 102]. The findings described in this chapter has the potential to seriously impair the predicted performances of these S-bend laser structures. Nevertheless they were not be assessed or described as part of this thesis.

In this chapter, the theoretical development and experimental results leading to these new insights are presented.

5.2 Coupling Coefficients with a Waveguide Tilt

Consider a ridge waveguide that is oriented along $\hat{z}$. Now a grating at an arbitrary angle θ is introduced such that the perturbation in refractive index $\Delta\eta(x,y)$ can be written as

$$\Delta\eta(x,y) = \Delta\eta_o \sin(\mathbf{K}\cdot\mathbf{r}) \tag{5.1}$$

where θ is the angle between $\mathbf{K}$ and $\hat{z}$ (see figure 5.1). In this context, it is convenient to think of the grating as a plane standing wave that has both direction and magnitude. The waveguide modes will then experience a component of this corrugation along $\hat{z}$ and another component along $\hat{x}$. Using the equations derived earlier in chapter 2, equations (2.20) and (2.21), the coupling coefficient in the presence of tilt can be written as:

$$\kappa_{nm} = \left[\bar{\kappa}^2_{nm,a} + \bar{\kappa}^2_{nm,s}\right]^{1/2} e^{j(\beta_m+|\beta_n|-K_z)z} e^{j\alpha} \tag{5.2}$$

where $\bar{\kappa}_{nm,s}$ and $\bar{\kappa}_{nm,a}$ are the symmetric and the anti-symmetric components of the coupling, and

$$\alpha = \sin^{-1}\left[\frac{\bar{\kappa}_{nm,a}}{\sqrt{\bar{\kappa}^2_{nm,s} + \bar{\kappa}^2_{nm,a}}}\right]. \tag{5.3}$$

The symmetric component is responsible for coupling between even *or* odd modes while the anti-symmetric component is responsible for coupling between odd *and* even modes. These can be expressed as:

$$\bar{\kappa}_{nm,s} = \frac{k^2}{2\beta_m}\left\langle \mathbf{E_n}(x,y)\left|\eta(x,y)\,\Delta\eta_o\cos(K_x x)\right|\mathbf{E}_m(x,y)\right\rangle \tag{5.4}$$

$$\bar{\kappa}_{nm,a} = \frac{k^2}{2\beta_m}\left\langle \mathbf{E}_n(x,y)\left|\eta(x,y)\,\Delta\eta_o\sin(K_x x)\right|\mathbf{E}_m(x,y)\right\rangle \tag{5.5}$$

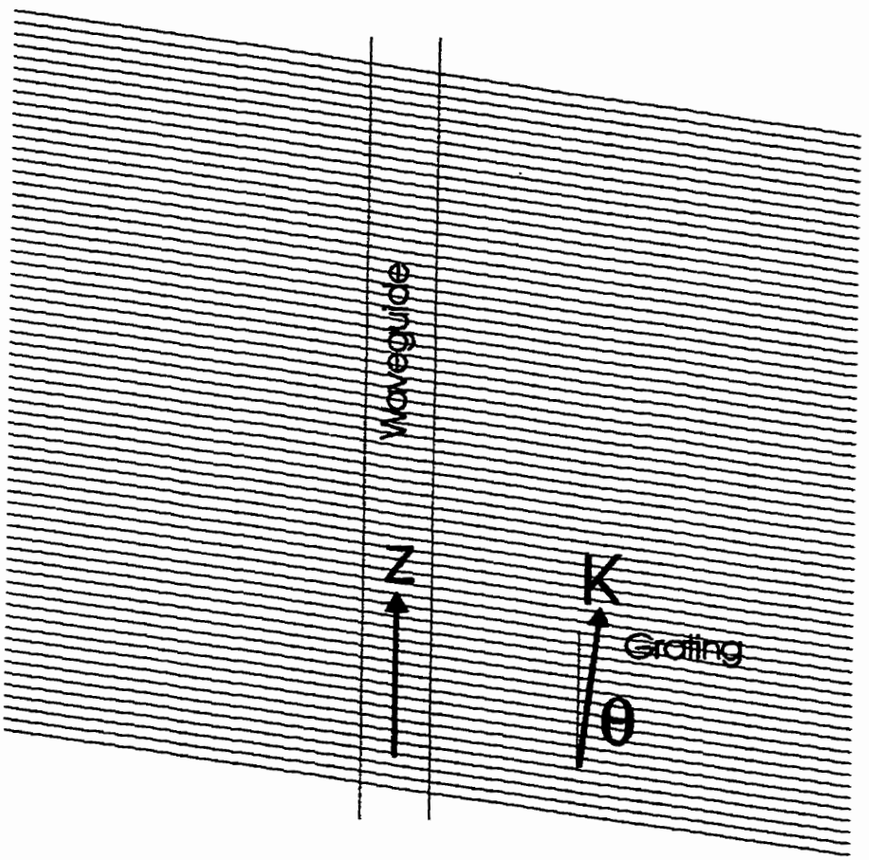

Figure 5.1: Depiction of the tilted ridge waveguide with respect to the gratings.

where

$$K_z = K\cos\theta \tag{5.6}$$

$$K_x = K\sin\theta. \tag{5.7}$$

Much of the mathematical derivations leading to the above results have been omitted. However, the main outcome of this formulation is that, as a result of the finite angle between the propagation constant $\beta_m\hat{\mathbf{z}}$ and the grating vector $\mathbf{K}$, a periodic perturbation along the *lateral* direction is induced. Therefore, the effect of the tilt angle θ is not only to reduce the grating wave-vector from K to $K\cos\theta$ (or alternatively increase the grating pitch by a factor $1/\cos\theta$), but also to reduce the coupling coefficient through the expressions given in (5.4) and (5.5).

As an example, consider a typical InGaAsP 1.55μm DFB laser with a grating pitch of 242nm and a ridge width of 3.0μm. Using equations (5.6) and (5.7) it can be seen that it only takes about 4.6 degrees tilt to induce a transverse period that is *equal* to the ridge width. Even at much larger transverse periods this effect will still be important. As a result, one can expect a significant degradation of κ at angles much smaller than 4.6 degrees. This is shown diagrammatically on figure 5.2 for various tilt angles. Obviously, this effect becomes more prominent for larger ridge widths than for smaller widths for a given tilt angle. Further, this effect is not restricted to ridge waveguide structures alone. The formulation should be valid for all guided wave laser structures including buried hetero-structure lasers. The only difference would arise through the transverse optical mode profiles for these structures. In a ridge waveguide laser, the lateral optical confinement is weak and the lateral extent of the optical field is larger than the ridge width. On the other hand, in a buried hetero-structure laser the lateral optical confinement is stronger. This will result in an optical field that is well confined within the waveguide. Therefore, the

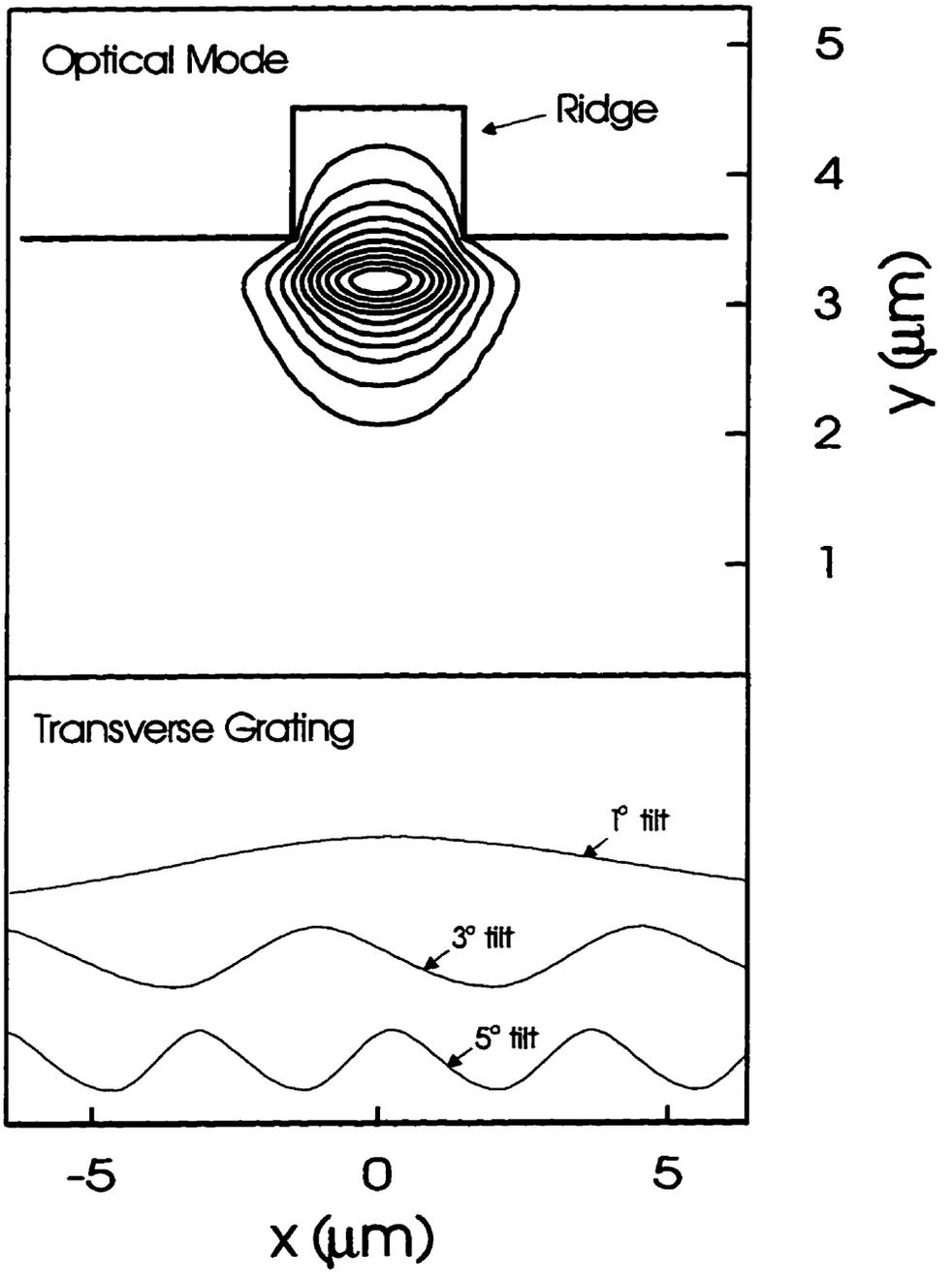

Figure 5.2: Contour plot of the fundamental $\hat{x}$ polarized optical mode ($E_{x,0}$) and the effect of tilt-induced transverse periodicity.

effect of tilt will be more pronounced in a ridge waveguide laser than in a buried hetero-structure laser for the same waveguide width. However, qualitatively the behaviour of the two structures will be similar.

In a DFB laser, one is are primarily interested in resonant states only. In general, hybrid coupling terms do not produce resonant states. This is because the hybrid terms do not lead to the phase matching condition required in equation 2.20. This was discussed in chapter 2. As a result, these hybrid terms will be ignored in the rest of this chapter, and only the intra-mode coupling terms will be retained.

The longitudinal corrugation will be the $\hat{z}$ component of $\mathbf{K}$. Therefore, the center of the stop-band (bragg frequency) will shift as $K_{\text{bragg}} = K\cos\theta$ and the wavelength will shift as $\lambda_{\text{bragg}} = \lambda/\cos\theta$. In the case of index-coupled DFB laser, there will be two degenerate lasing modes displaced from the bragg mode by half the DFB stop-band width. Since the stop-band width is a function of $\bar{\kappa}_{nm}$ it can be seen that one cannot simply ignore the dependence of $\bar{\kappa}_{nm}$ on θ. Further, the relative magnitudes of $\bar{\kappa}_{nm}$ from the different transverse modes will have to be considered to determine which mode has the lowest threshold gain. It was shown in chapter 4 that the E_{x0} mode always had the lowest threshold gain in the absence of tilt. It will be shown in this chapter that that will not necessarily be the case in the presence of a tilt angle.

In the following sections, the effect of ridge tilt on single- and multi-transverse moded ridge waveguides are investigated separately.

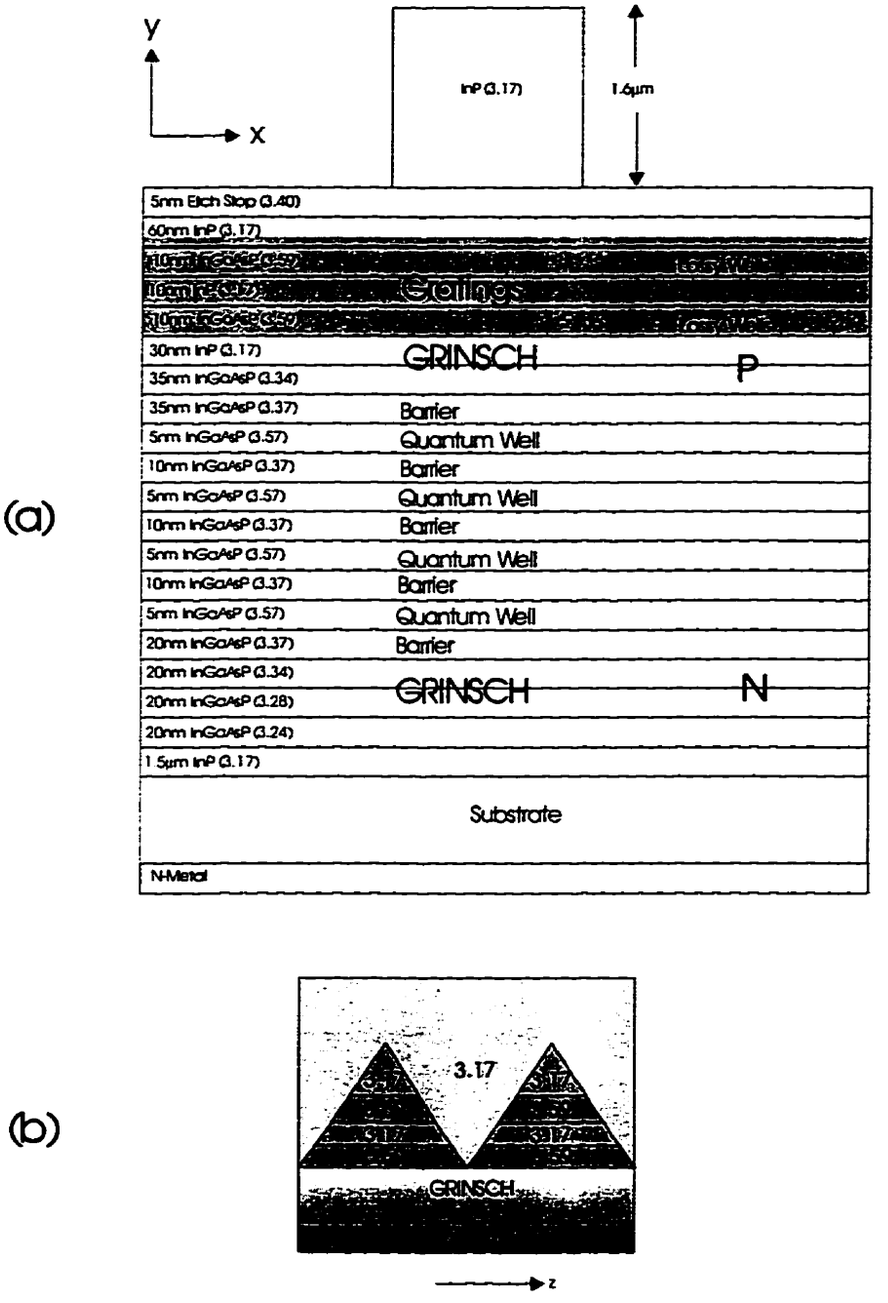

Figure 5.3: Layer structure of the loss-coupled DFB laser.

5.3 Single Transverse Mode Tilted Ridge DFB Lasers

The DFB laser structure considered here is shown on figure 5.3. It is a 1.55μm InGaAsP/InP weakly loss-coupled GRINSCH-MQW structure with four gain quantum wells and two absorbing quantum wells. The absorbing quantum wells have a smaller band-gap than the gain quantum wells and are away from the p-n junction. The absorbing wells, which are grown above the gain wells, were periodically etched off and re-grown with InP to produce a complex grating. The width of the ridge waveguide was designed to be single moded at 1.2μm, and the facets were AR coated on one side and cleaved on the other.

For the calculation, the complete two-dimensional refractive index profile including all epitaxial layers and quantum wells was discretized and input into a non-uniform two-dimensional mesh. Using a finite-difference scheme described in chapter 3. the optical mode of this structure was computed. This was then used to find the complex coupling coefficient κ as a function of the tilt angle (equation 5.4). Due to the effect of tilt-induced transverse periodicity. κ decreases with increasing tilt angle. This is shown on figure 5.4a. It can be seen that $\Re\{\kappa\}$ varies from about 120/cm to 20/cm as the ridge is tilted incrementally from 0 degrees to 10 degrees. As a result, the threshold gain of the device can be expected to increase quite drastically. The corresponding threshold gain (for a cavity length of 375μm) is shown on figure 5.4b.

On figure 5.5. the calculated and measured wavelengths as a function of the tilt angle is shown. The wavelength measurements were made at current levels just above threshold. The solid lines were calculated by neglecting the thermal effects, and the dashed lines by including the thermal effects (The thermal aspects of the problem are discussed in the next section). For each curve, the two lines correspond

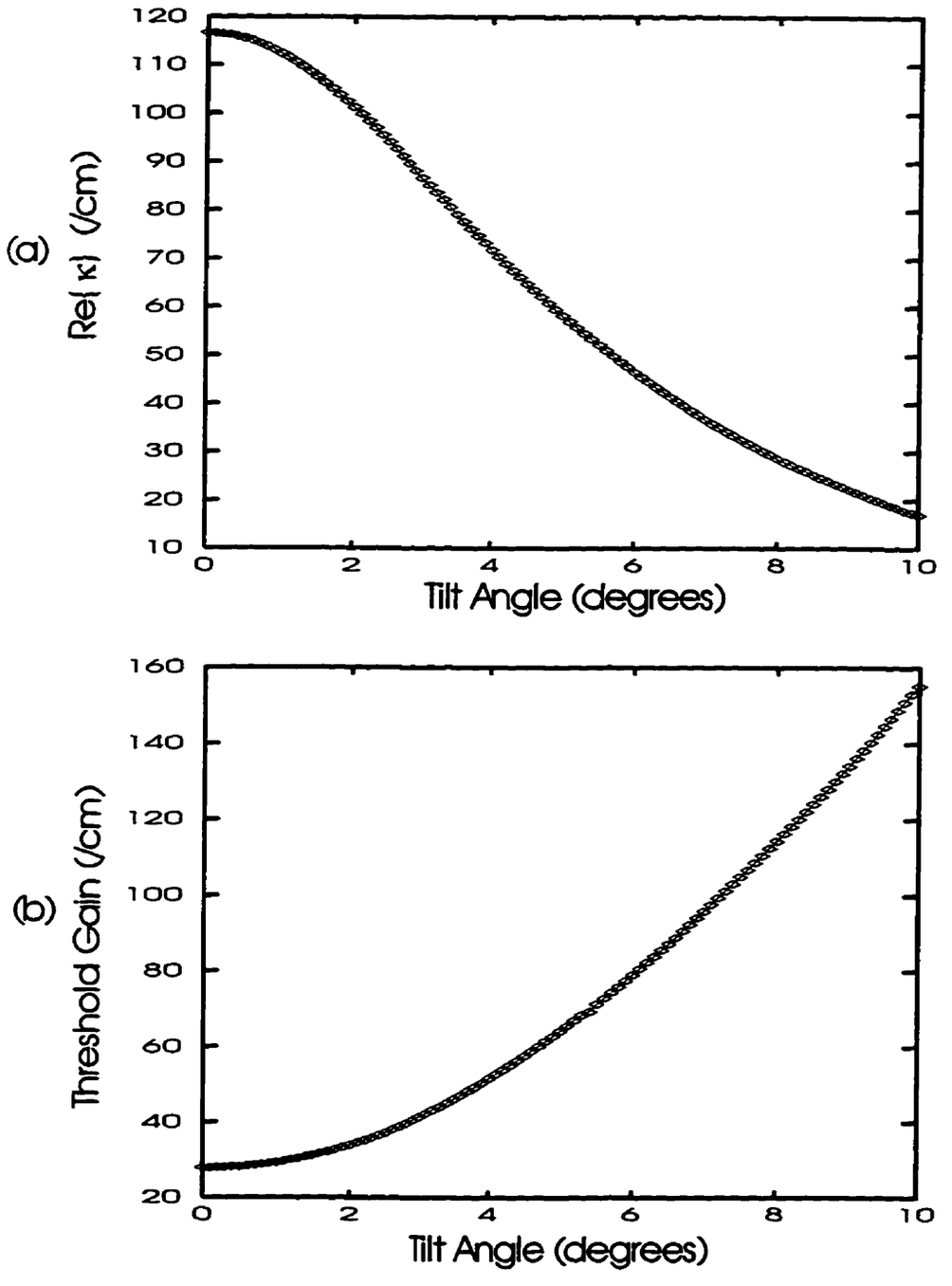

Figure 5.4: Calculated (a) Re{κ} (b) threshold gain as a function of the waveguide tilt angle for the single mode 1.2μm wide laser.

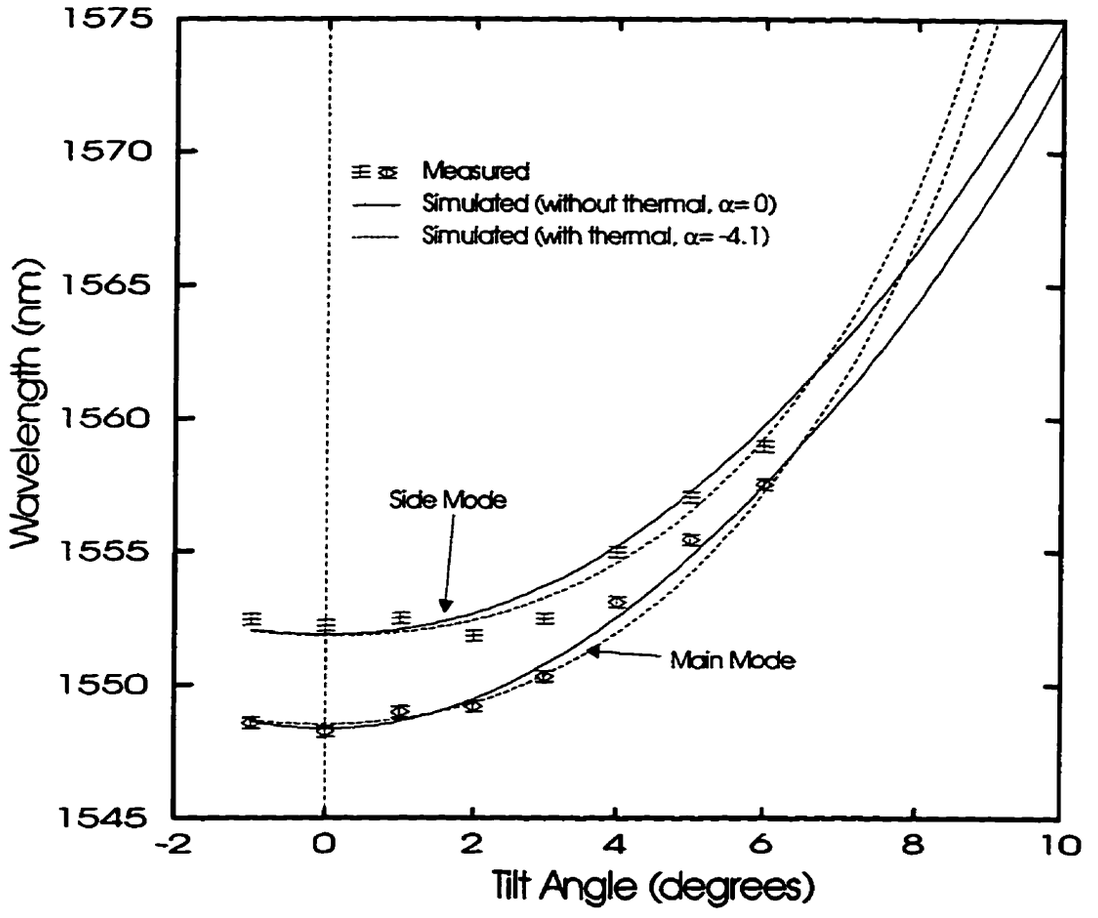

Figure 5.5: Calculated and measured wavelength vs tilt angle for the 1.2μm wide laser. Both the main lasing mode and the side modes are shown. The solid line was obtained by neglecting all thermal and linewidth enhancement effects, while the dashed line was obtained by considering both these effects.

to the main lasing mode and the main side mode. Due to the loss-coupling effect, the shorter side of the DFB mode is the primary lasing mode at low injection currents. The dependence of κ on tilt angle is exemplified by the narrowing stop band width at high tilt angles. As a result, the wavelength vs tilt relationship deviates from the simple $\lambda \sim 1/\cos\theta$ expression. The center of the DFB stop band will follow the $\lambda \sim 1/\cos\theta$ expression while the lasing mode being displaced from the center of the stop-band will deviate from this simple relationship.

On figure 5.6 the measured spectra are shown for six different tilt angles. The measurements were taken at a constant injection level of 80mA. The plots have been arbitrarily offset along the y-axis to enhance clarity. At 0 degrees and 1 degree tilts, the primary lasing oscillation takes place on the short wavelength side of the DFB stop-band. This is as expected from the loss-coupling mechanism. However, for the devices with larger tilt angles the primary oscillation shifts to the longer wavelength side. In fact, it has been observed that the oscillation starts on the short wavelength side at low currents, and then switches to the long wavelength side at high currents. This is attributed to a combination of several factors: (a) since κ progressively gets smaller with increasing tilt angles, the spatial hole burning effects will also get smaller. This will result in a reduced preference towards the short wavelength side of the oscillation; (b) since the devices with larger tilts have a higher threshold current, the carrier density in these devices will also be higher for a given injection level above threshold. As a result, the absorbing quantum wells will get saturated and become less absorbing. This reduces the preference towards the short wavelength side; (c) due to the higher threshold currents, the devices with larger tilt angles operate at a higher temperature at any given injection current. The gratings in this wafer were placed with a negative detuning from the gain peak. As the gain peak moves with temperature, due to the nonlinear shape of the gain curve, this will result in

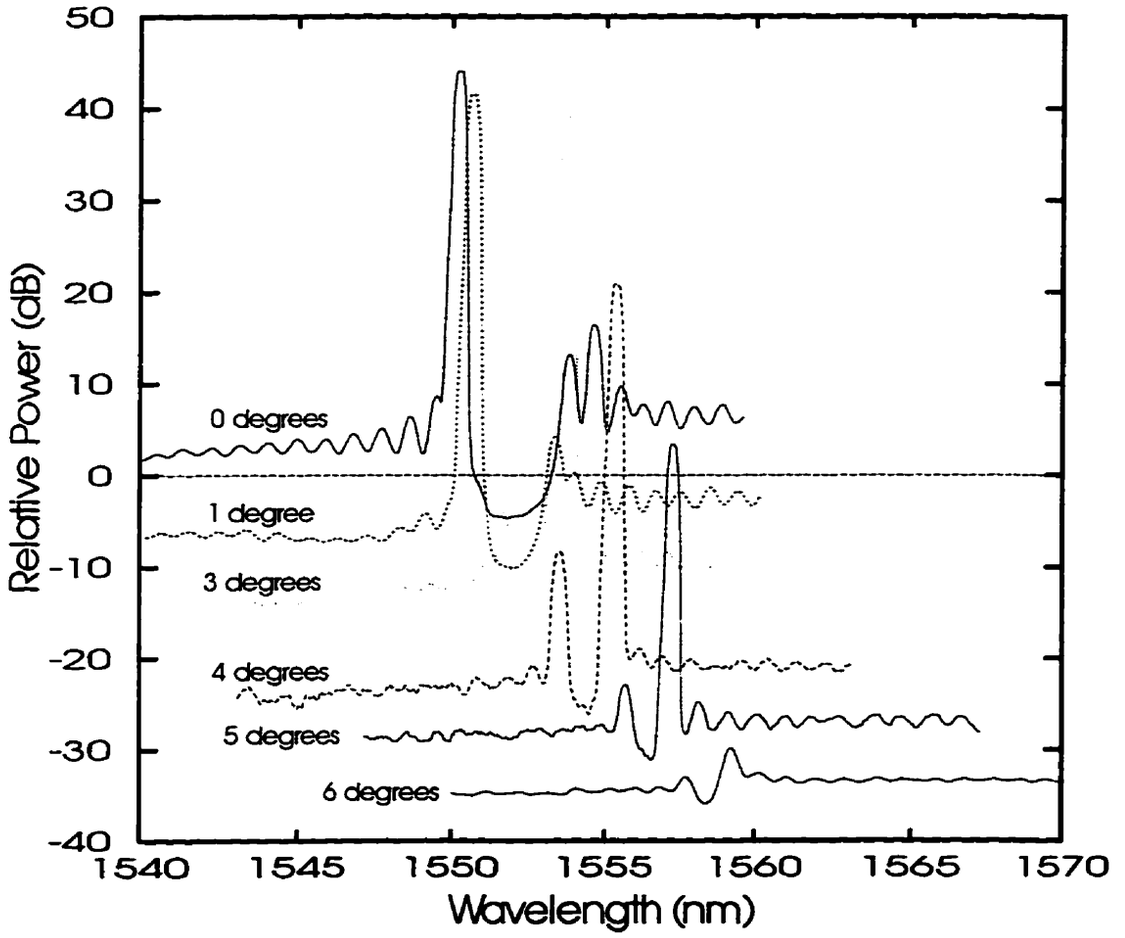

Figure 5.6: Measured lasing spectra at 80mA for the 1.2μm wide tilted laser arrays.

a preference towards the longer wavelength side. Nevertheless, the main features to observe on figure 5.6 are the red-shifting of the stop-band, the narrowing of the stop-band and the reduced power in the lasing mode. These are all direct results of the diminishing κ.

Next, assuming a logarithmic MQW gain function of the form

$$g = a \ln\left(\frac{J}{J_o}\right) \tag{5.8}$$

the threshold current density as a function of tilt angle can be written as

$$J_{th} = J_o \exp^{\frac{g_{th}(\theta)}{(\Gamma a)}} . \tag{5.9}$$

The two-dimensional optical confinement factor Γ was calculated from the mode profile to be around 4.4%. With $a = 850/\text{cm}$ and $AJ_o = 15.3\text{mA}$, the resulting threshold current as a function of tilt angle is shown on figure 5.7 along with the measured values. Since g_{th} is a function of θ (figure 5.4b), the threshold current becomes even more sensitive to the tilt angle. As a result, the maximum range of tilt angle that can be used for wavelength control becomes limited to about 4 or 5 degrees. For the laser structure considered in this context, that translates to a wavelength tuning range of about 10nm.

5.3.1 Thermal Effects

The increase in threshold current as a function of tilt angle was shown on figure 5.7. This was primarily due to the increase in the threshold gain with tilt angle. The increase in threshold gain as a function of tilt angle was shown on figure 5.4b. As a result, one would expect a significant increase in the active region temperature at the threshold current with increasing tilt angle. Since refractive index increases

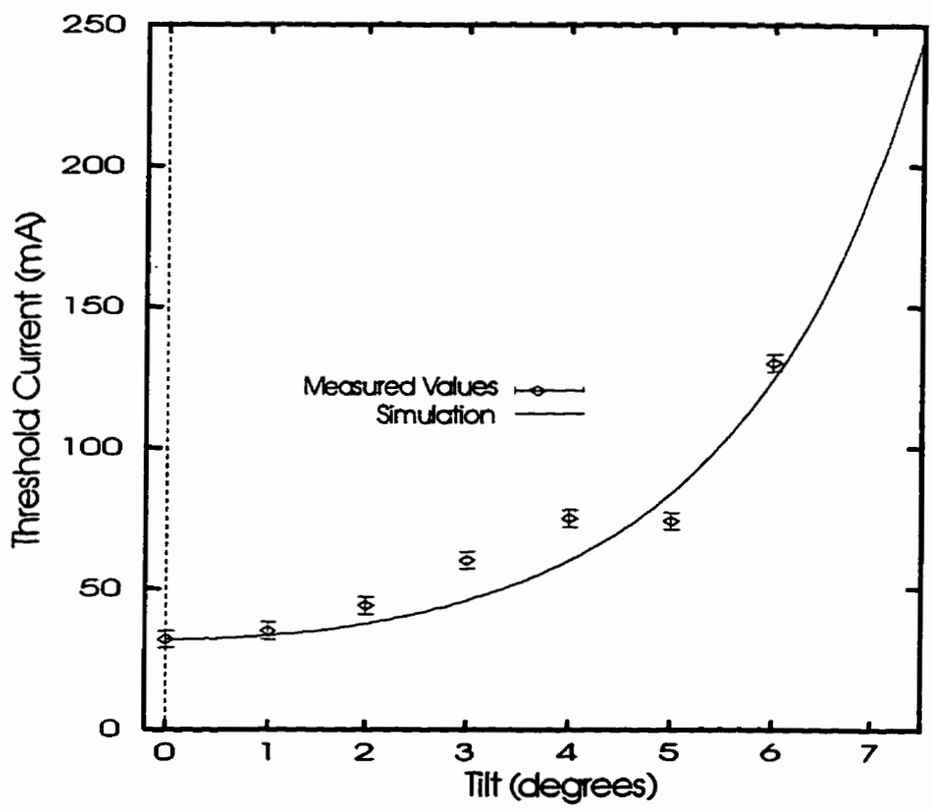

Figure 5.7: Calculated and measured threshold current as a function tilt angle for the 1.2μm wide laser array.

with temperature, this will lead to a red-shift in wavelength. However, at the same time, the increasing threshold gain in the device will produce a blue-shift due to the effects of the line width enhancement factor α. These two effects will be competing with each other. The end result will be a much smaller net wavelength shift (red or blue shift) than one would expect from one effect alone. On figure 5.5, the solid lines were calculated without considering any thermal effects and with $\alpha = 0$. The dashed line was calculated using a simple thermal model as described below.

The change in wavelength measured at threshold can be written as the sum of the red shift due to thermal effects and the blue shift due to the linewidth enhancement effects. It will be assumed that the heat is generated in the laser by the current flowing through the parasitic series resistance of value R_s. Assuming a thermal resistivity of R_T degrees C/Watt, and a a thermal wavelength shift of $d\lambda/dT$:

$$\Delta\lambda = \Delta\lambda_{\text{thermal}} + \Delta\lambda_{\alpha} \tag{5.10}$$

$$= \frac{d\lambda}{dT} I_{th}^2 R_s R_T + \alpha \frac{\lambda g_{th}}{K \cos\theta}. \tag{5.11}$$

The dashed line on figure 5.5 was calculated using typical values of $R_s = 10\Omega$, $d\lambda/dT = 0.1$nm/deg C, $R_T = 100$ deg C/W and $\alpha = -4.1$. At 6 degrees tilt angle, $\Delta\lambda_{\text{thermal}} \approx 1.40$ nm, while $\Delta\lambda_{\alpha} \approx -1.42$ nm. As a result, the net wavelength shift with the thermal model and $\alpha = -4.1$ is very close to the one obtained without considering either of these effects. Although in this example the thermal and the linewidth enhancement factors have almost cancelled each other out within the range of measured values, in general that would not be the case. Depending on the magnitudes of the thermal resistivity of the chip R_s and α, one may observe a resultant red or blue shift at the threshold current with increasing tilt angle.

5.4 Multi Transverse Mode Tilted Ridge DFB Lasers

Consider the index-coupled GRINSCH-MQW laser structure shown on figure 4.1. It has 17 layers of different refractive indices and thicknesses. For this study, the ridge width and height were chosen as 3.0μm and 1.5μm respectively. The 3.0μm ridge width was chosen so that the structure is able to support at least four transverse modes. The gratings were produced by etching the shaded region on figure 4.1 and re-growing it with InP. Therefore, in calculating the transverse optical modes the average refractive index between the etched/re-grown area and the un-etched area is used. The amplitude $\Delta\eta_o(x,y)$ will then be half the difference between this average index and the actual index in the re-grown areas. The two-dimensional non-uniform mesh was discretized with 10 points in each layer in the vertical direction (total of 190 points including the ridge and air layers) and 45 points in the lateral direction. On figure 5.8 the resulting first order $\hat{x}$ polarized optical mode ($E_{x,1}$) is shown.

On figure 5.9 the coupling coefficient $\bar{\kappa}_{mn}$ is shown. At 0 degrees tilt, the fundamental $E_{x,0}$ mode has the largest $\bar{\kappa}_{mn}$. As a result. lasing oscillation along a single transverse mode will be obtained even though the ridge waveguide is multi-moded. This is consistent with the description presented in chapter 4. However, as the tilt is increased, the difference in $\bar{\kappa}_{mn}$ between the $E_{x,0}$ and the $E_{y,0}$ modes gets smaller. At some angle, both these modes will be degenerate and will oscillate simultaneously. Further increase in tilt will favour the higher order transverse modes. It is interesting to note that the fundamental modes will be completely attenuated while the higher order mode oscillates. This is an effect that cannot be achieved by any other means of design in a DFB laser. On figure 5.10 the threshold gains of these modes are shown. Note that this is plotted on a log scale due to the large sensitivity of the threshold gain on $\bar{\kappa}_{mn}$. In this calculation, the device length was set at 325μm

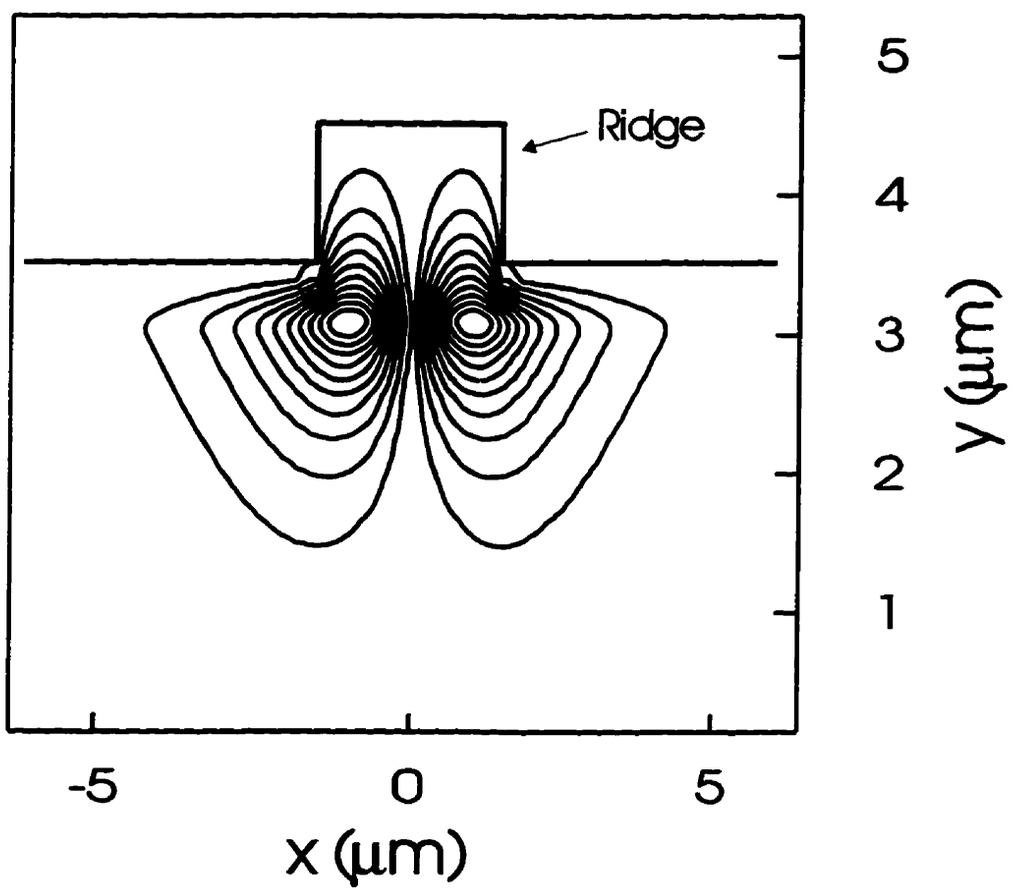

Figure 5.8: Calculated contour plot of the $\hat{x}$-polarized first order mode in the 3.0μm wide laser structure.

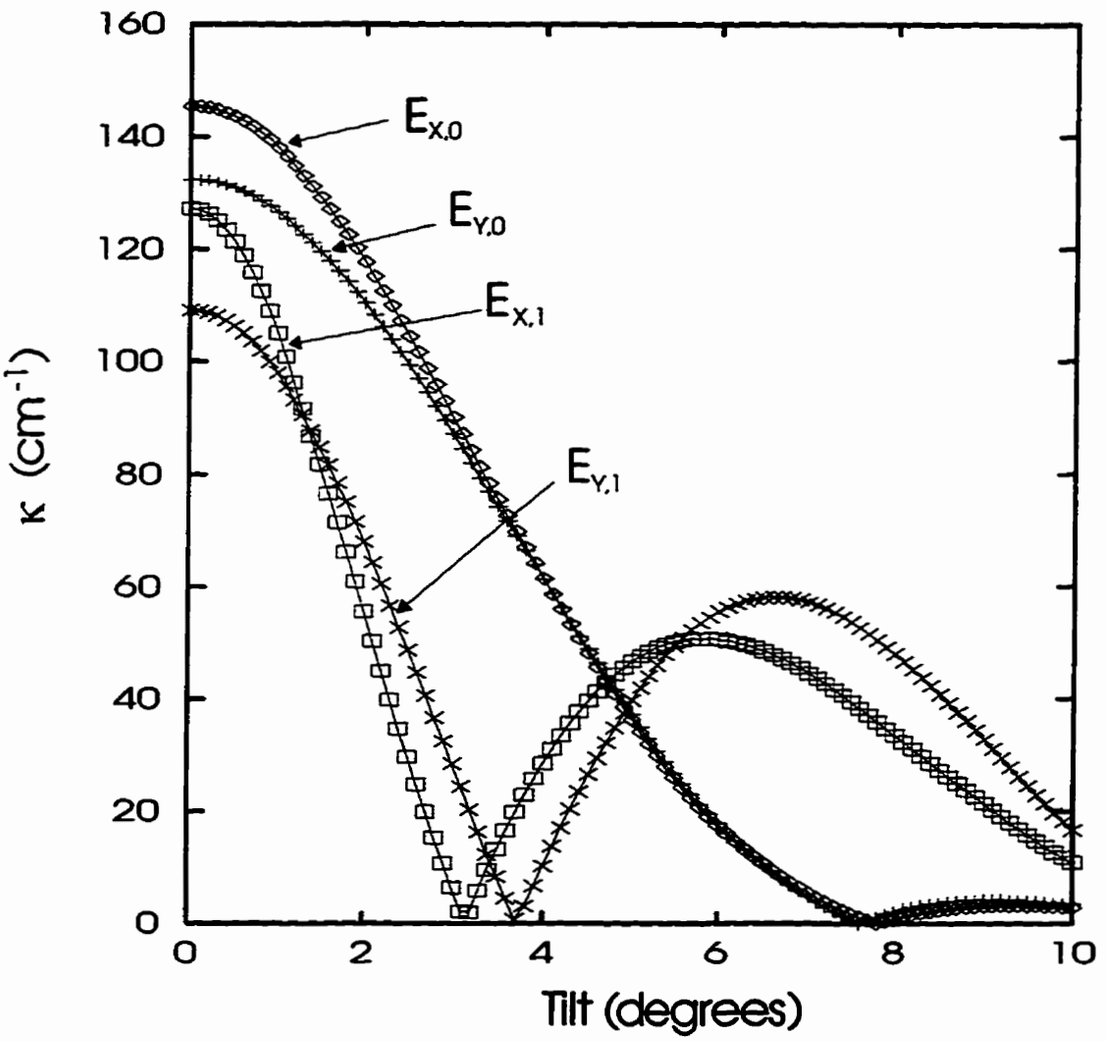

Figure 5.9: Calculated κ_{mn} with tilt angle for the various transverse modes for the 3.0μm wide laser array.

with zero facet reflectivities. The crossing points of the threshold gains correspond to the degenerate states of the different transverse modes.

The simulated emission spectrum just near threshold of the 0° tilt ($E_{x,0}$ oscillation) and the 8° tilt ($E_{y,1}$ oscillation) are shown on figure 5.11. The smaller stop-band width of the 8° tilt can be clearly seen on this figure. Also, as a result of the higher threshold gain of the tilted device a larger amount of spontaneous emission noise can be seen outside its lasing DFB modes. This raises the spontaneous emission noise floor of the spectrum.

On figure 5.12 the cumulative lasing wavelength as a function of tilt angle is shown. Due to the effect of threshold gain on tilt angle the lasing mode will shift towards the higher order modes. This will correspond to a shift to a shorter wavelength. Although these shifts are shown as sudden jumps, in reality the transition region will be somewhat smoother because both transverse modes will lase when the threshold gain difference is sufficiently small. As a result, it becomes evident that the wavelength as a function of tilt in multi-transverse moded ridge structures will be characterized by discrete jumps towards shorter wavelengths in addition to the $1/\cos\theta$ type relationship.

5.5 Combined Effect of Ridge Tilt and Ridge Width

Having studied the wavelength tuning effects due to waveguide width and waveguide tilt, it is of interest to know if the two effects can be combined to achieve a larger tuning range. In order to investigate this, a laser array consisting of 16 elements with ridge widths incrementing from 1.6μm to 5.2μm and with tilts incrementing from 0° to 7.5° was fabricated on the index-coupled wafer structure shown on figure 4.1. The device geometries are summarized in table 5.1.

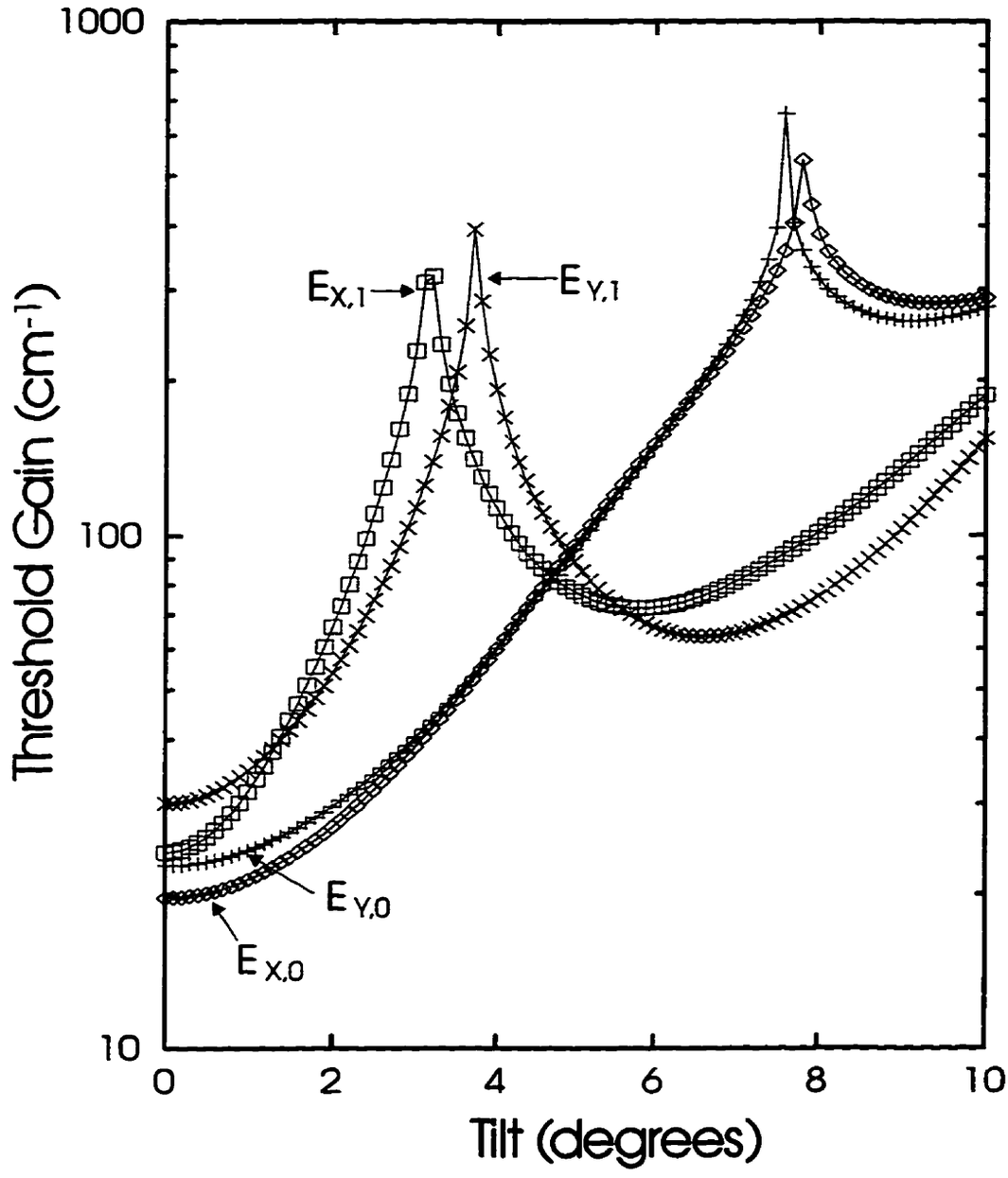

Figure 5.10: Calculated threshold gain with tilt angle for the various transverse modes in the 3.0μm wide laser array.

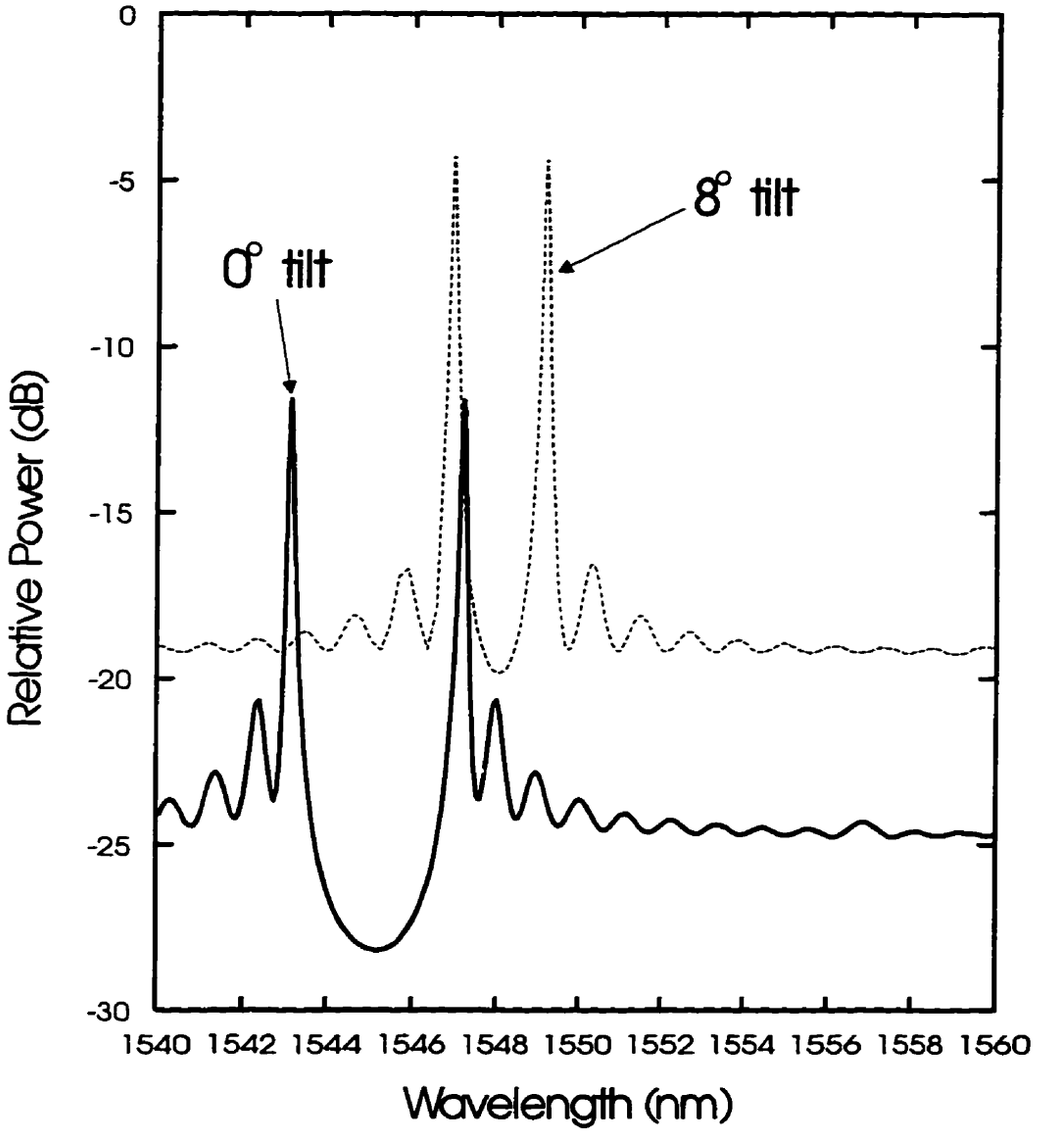

Figure 5.11: Simulated above threshold lasing spectra for 0° and 8° tilt angles for the 3.0μm wide laser.

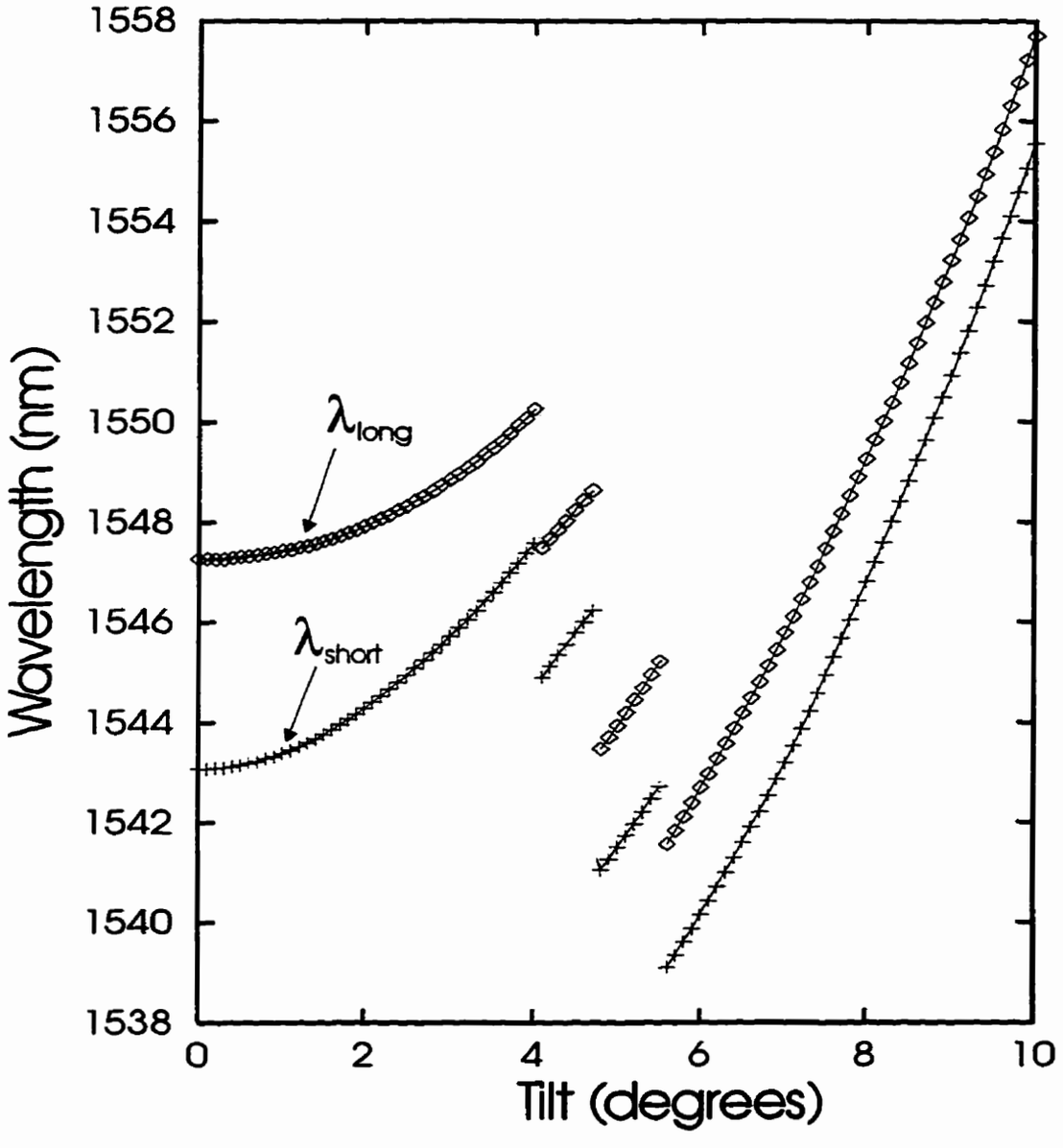

Figure 5.12: Calculated cumulative lasing wavelength as a function of tilt angle for the 3.0μm wide laser. Both wavelengths corresponding to the degenerate DFB modes are shown.

Device Number	Ridge Width (μm)	Ridge Tilt (degrees)
1	1.6	0.0
2	1.8	2.0
3	2.0	3.0
4	2.2	3.5
5	2.4	3.9
6	2.6	4.3
7	2.8	4.7
8	3.0	5.0
9	3.2	5.3
10	3.4	5.6
11	3.7	5.9
12	4.0	6.2
13	4.3	6.5
14	4.6	6.8
15	4.9	7.1
16	5.2	7.5

Table 5.1: Ridge width and tilt angle of combined width/tilt laser array.

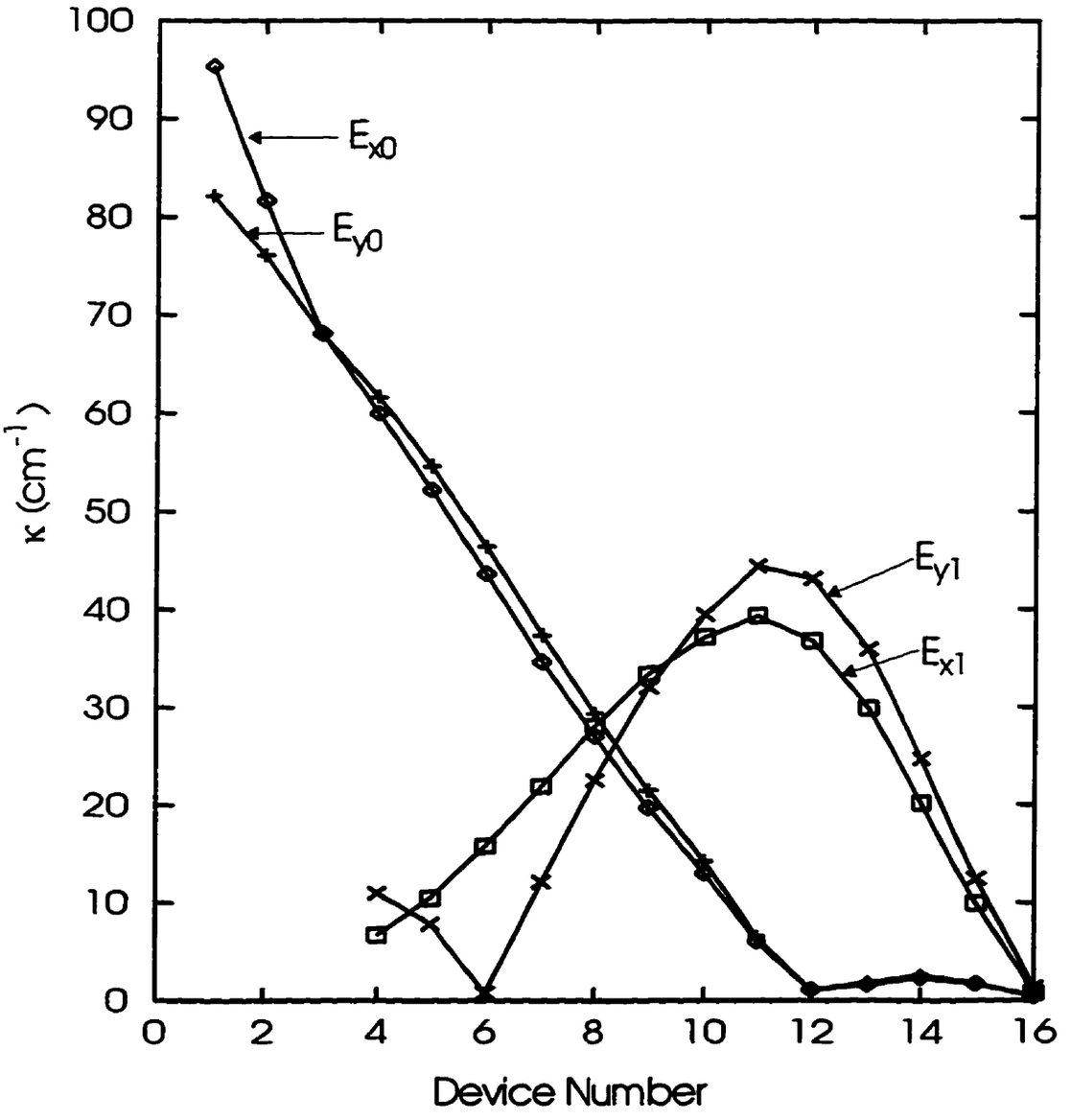

Figure 5.13: Calculated κ_{mn} in the combined ridge width/tilt angle DFB laser array.

The two-dimensional optical mode profiles and the coupling coefficients were calculated for this array of lasers. The results are shown on figure 5.13. From this figure it can be seen that for devices 1-3 the fundamental E_{x0} mode will oscillate. This will be followed by oscillation along E_{y0} for devices 4-7. Subsequent oscillations will be along E_{x1} and the E_{y1} modes. Within each transverse mode the wavelength will red-shift approximately as $1/\cos\theta$, and the transition between the modes will be characterized by a jump towards a shorter wavelength.

The lasing spectrum measured at 30mA of injection current is shown on figure 5.14 for devices #1, #3, #5 and #7. In device #1 the oscillation is due to the E_{x0} mode only and the higher order transverse modes cannot be seen. In device #3 the higher order E_{y0} mode just starts to appear. In device #5 the E_{y0} mode is more prominent but yet the lasing takes place along the E_{x0} mode only. In device #7 the lasing has switched to the E_{y0} mode and the E_{x0} mode is less prominent. Note that these devices were index-coupled with facets AR/CL. Therefore the uncontrolled facet phase results in a random DFB mode selection as well as FP mode competition. This can be seen from the spectra on figure 5.14.

On figure 5.15 the wavelengths corresponding to all the detectable transverse modes in the laser array are shown. Both DFB modes on either sides of the stop-band are shown although only one mode lases due to the random phase of the facet. The non-lasing transverse modes are shown as dashed lines while the lasing modes are indicated by the solid lines. The thick lines correspond to measured points and thin lines for simulated points. This figure provides a fairly consistent agreement between experimental observation and theoretical simulation.

The above findings can be confirmed by the measurement of near field profile measurements at various current injection levels. On figure 5.16 the near field profiles of devices #8 and #11 are shown just below and above their threshold

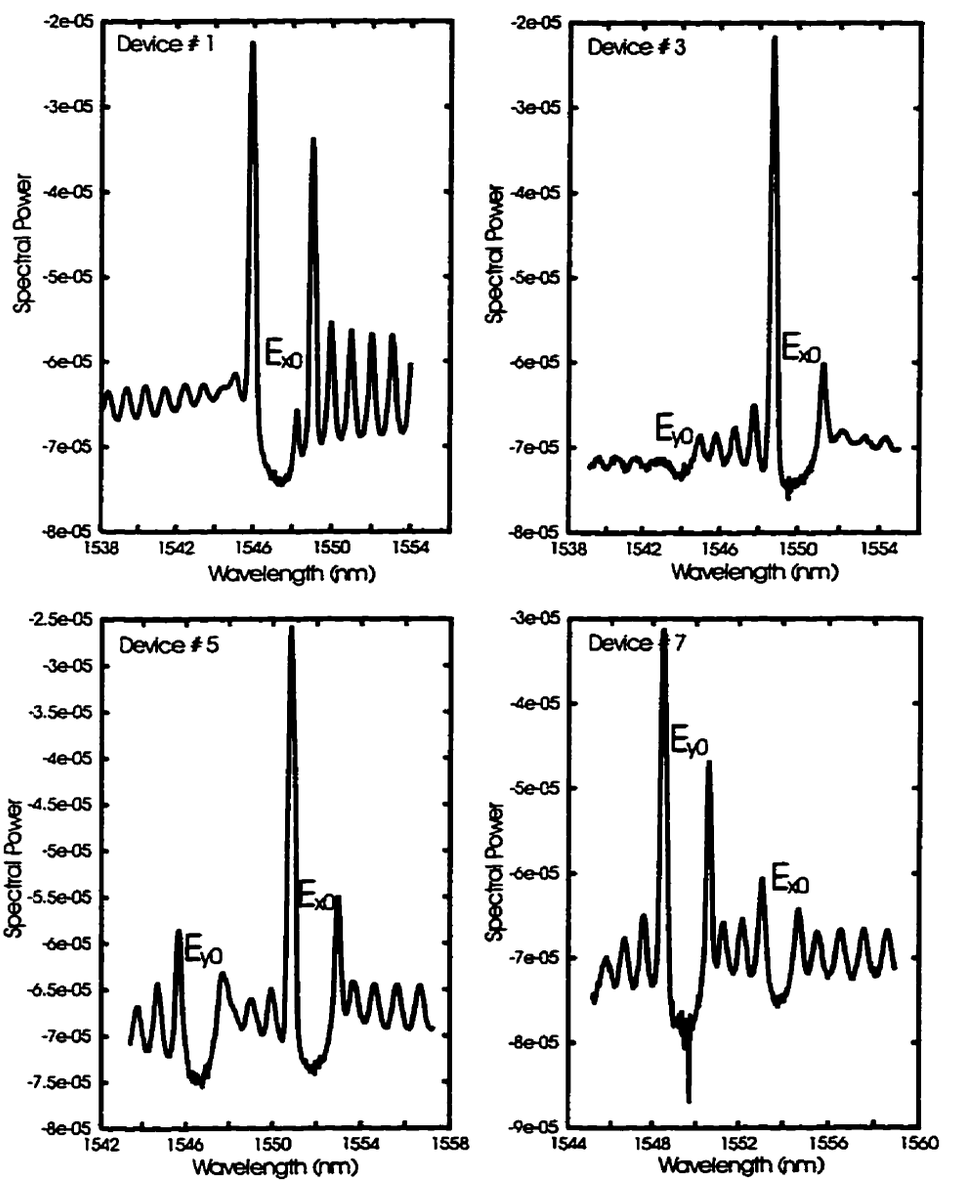

Figure 5.14: Measured lasing spectra of the combined ridge width/tilt angle DFB laser array.

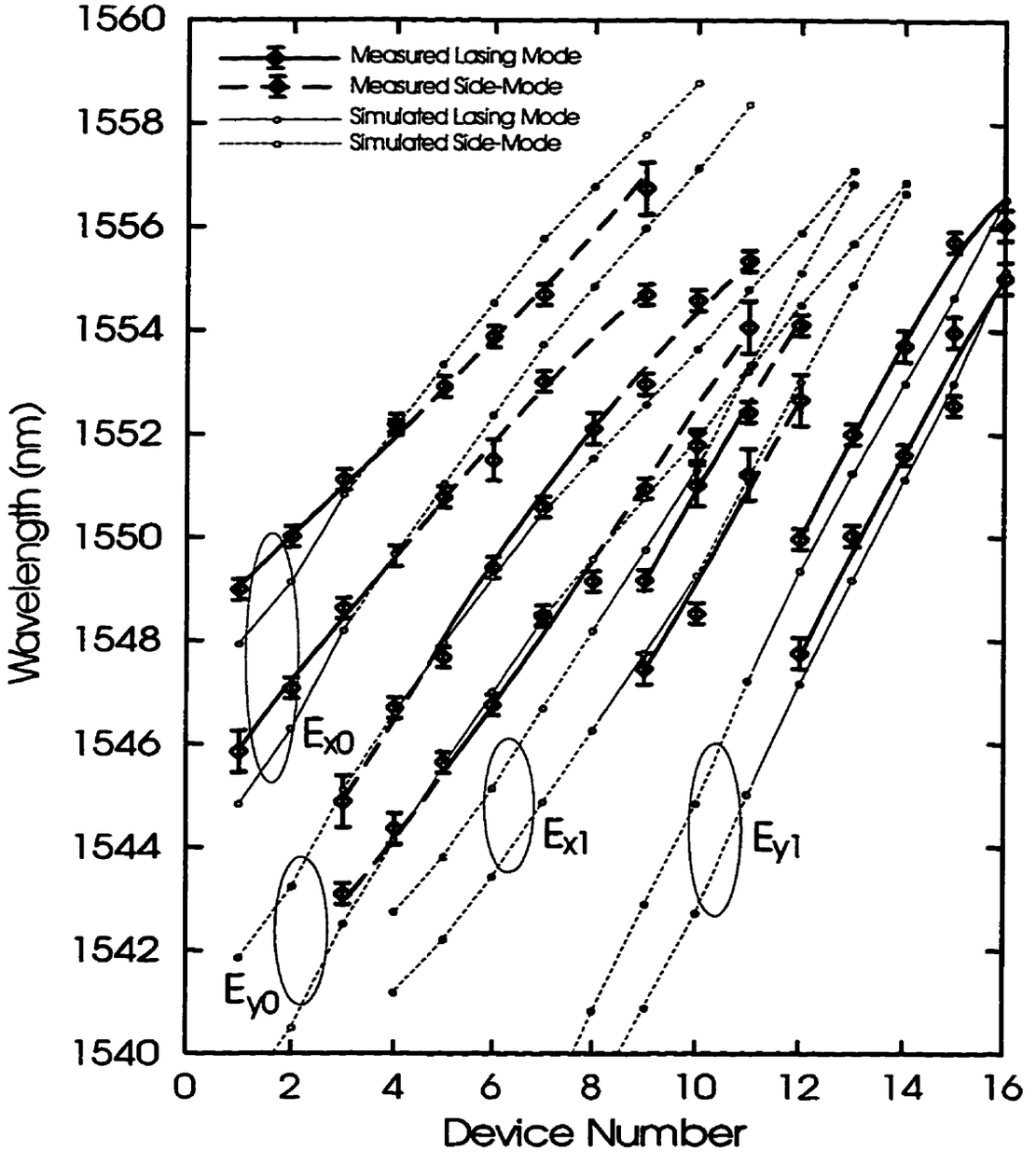

Figure 5.15: Calculated and measured wavelength in the combined ridge width/tilt angle DFB laser array demonstrating the mode jump towards higher order transverse modes.

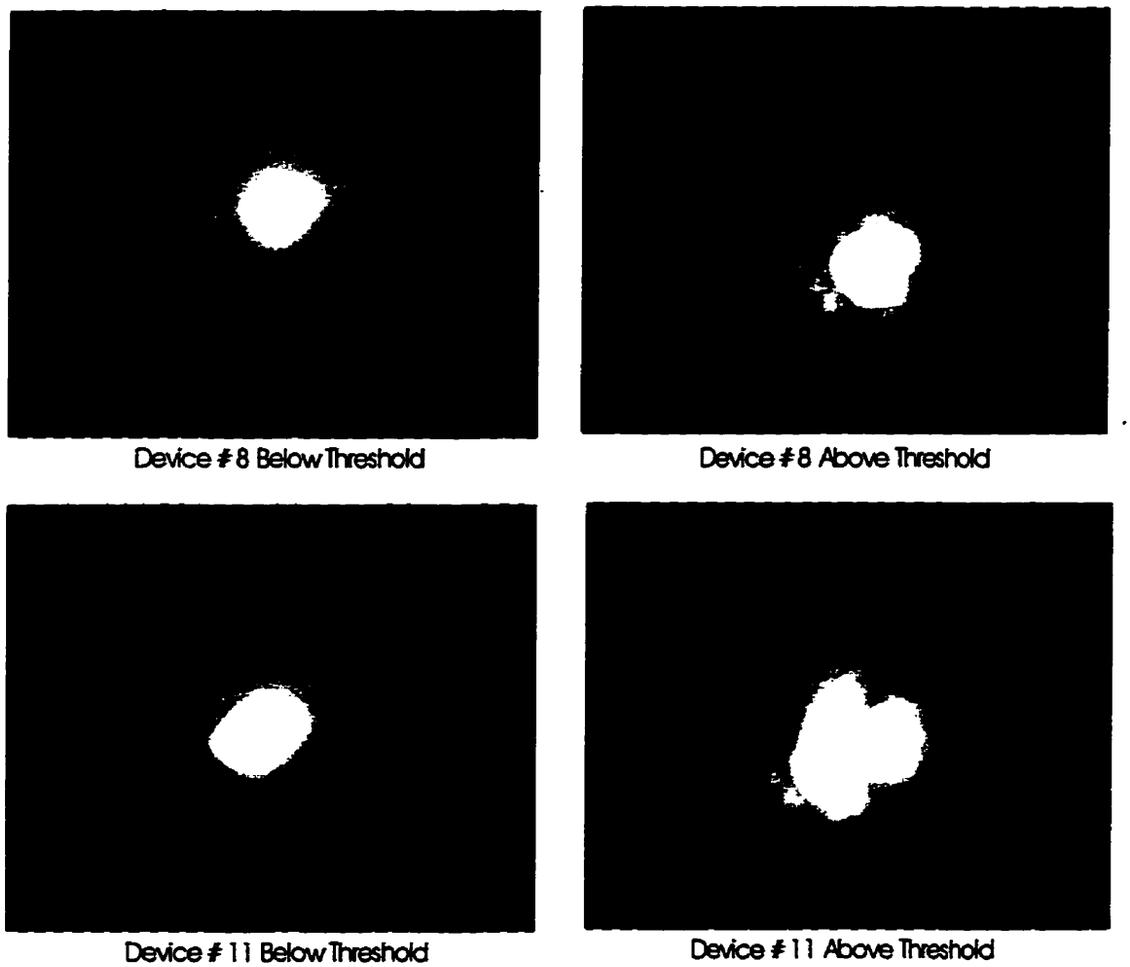

Figure 5.16: Measured near field profiles in the combined ridge width/tilt angle DFB laser array demonstrating the transverse mode jumps.

currents. Slightly below the threshold current all transverse modes will be equally excited by the spontaneous emission in the device because spontaneous emission does not discriminate between the various modes. This results in a more or less circular spot on the near field profile since it is a superposition of all the transverse modes in the waveguide. When pumped slightly above threshold, the transverse mode with the largest κ_{mn} will start to lase while all other transverse modes are suppressed. In device #8 the lasing takes place along the E_{y0} transverse mode. As a result, the near field profile shows an almost circular pattern even above threshold. On the other hand, in device #11 the lasing takes place along the E_{x1} transverse mode. This can be inferred from the coupling coefficients shown on figure 5.13. As a result, the transition from below to above threshold is characterized by the near-field pattern evolving from a circular to a double-lobed profile.

5.6 Conclusions

In this chapter, a description of wavelength control in DFB laser arrays using waveguide tilts was described. Using a full two-dimensional analysis it was shown that the simple of $\lambda \sim 1/\cos\theta$ model most frequently used in the literature is seriously inadequate. In addition to the resonant wavelength λ, the coupling coefficient κ was also found to be a strong function of tilt angle. The result was a significant increase in threshold current with tilt angle, limiting the useful range of the wavelength tuning that can be achieved with this scheme. Further, it was shown that when the waveguide is multi-transverse moded the tilt angle selectively controls which transverse mode will oscillate. As a result, it is possible to design a laser with lasing oscillation at a higher order transverse mode while suppressing the fundamental mode. These findings supplement the results obtained in chapter 4. All of

the above theoretical results were confirmed with experimental measurements from a DFB laser array designed and fabricated with different tilts and ridge widths.

Chapter 6

Conclusions and Recommendations

6.1 Conclusions

The important conclusions from this thesis can be briefly stated as follows:

- A longitudinal below and above threshold DFB laser model in the spectral domain has been theoretically formulated and implemented (chapter 2).
- A full two-dimensional optical model with lateral carrier effects has been incorporated in the above DFB model (chapter 3). This quasi-three-dimensional model enables a more realistic prediction of laser performance with longitudinal spatial hole burning as well as transverse two-dimensional effects.
- A multi-wavelength DFB laser array using the varying ridge width approach has been proposed, theoretically modeled, fabricated and experimentally verified (chapter 4). It was found that single transverse mode oscillation is maintained even for ridge waveguides wide enough to support multiple transverse

modes. This array was used in the demonstrated of a four-wavelength simultaneous operation of a WDM transmitter, a first such demonstration of its kind.

- A multi-wavelength DFB laser array using incremental tilt angle was demonstrated (chapter 5). With the use of the three-dimensional DFB model, previously unknown dependence of critical DFB parameters on tilt angle was discovered. It was found that the selection of which transverse mode oscillates can be predictably controlled with the tilt angle. All of these findings were substantiated with experimental results.

6.2 Recommendations for Future Research

Fiber telecommunications is presently witnessing its highest growth in history. As such, it is not easy, nor will it even be wise, to predict its direction or make specific recommendations that would still hold true a few years from now. Nevertheless, a few immediate follow-up to this Ph.D dissertation can be recommended:

- The dependence of the dynamic performance of the DFB lasers on their geometries has to be assessed. This will be the immediate next step if one were to follow-up on this research. Further, dynamic cross-talk between laser elements is also an important study that could be of value in assessing the use of arrays in practical WDM systems.

- The results from chapter 5 call for a reassessment of S-bend lasers. Although it is clear that the findings of chapter 5 would have a significant impact on the performance these lasers, it is not immediately apparent what characteristics or to what extent these performances will be affected.

Recommendations for future research do not end with the above comments on the technical aspects of the work. I am compelled to make a few general comments aimed at those who are entering the photonics area on the choice of their research topic.

Formal electro-magnetics has been in existence for over a century. Semiconductor electronics, though relatively new, has been in existence for at least half a century. Both are fairly mature areas. On the other hand, photonics is a new, exciting and a fertile research area. The primary reason for this is not a revolutionary advancement in either electro-magnetics or semiconductors. Instead, it is due to the merging of the two areas. Simultaneous expertise in both areas is what makes a research topic in photonics a promising one.

As such, I would hesitate to recommend to a future student entering this area to engage in a detailed fundamental study of one aspect of a problem alone. To the uninitiated, the extent of the knowledge required to carry out a broad research program in photonics can, at first, be overwhelming. However, it has seldom been the case that detailed fundamental studies alone have lead to innovative ideas or revolutionary technologies. As in most fields of engineering research, and device research in particular, it is the novel combination of different disciplines that will inspire innovation and shape its future. The application of knowledge gained from different areas of study and the appreciation for what separates engineering from pure science has been the most rewarding part of this research program.

Appendix A

DFB Reflection and Transmission Coefficients

A.1 Formulation

In a grated structure. the field can be written as

$$\mathbf{E} = \sum_n a_n(z)\,\mathbf{E}_n(x,y)\,e^{-j\beta_n z}. \tag{A.1}$$

Interpreting the components as forward and backward travelling waves, the following solutions can be obtain as detailed in section 2.2:

$$a_1(z) = \left(Bre^{\gamma z} + Ae^{-\gamma z}\right) e^{j\delta z} \tag{A.2}$$

$$a_2(z) = \left(Be^{\gamma z} - Are^{-\gamma z}\right) e^{-j\delta z} \tag{A.3}$$

A.2 Right Reflection Coefficient

The relfection coefficient to the right of a point inside the cavity can be written as

$$r_1(0) = \frac{a_2(0)}{a_1(0)}. \tag{A.4}$$

Using the expressions for $a_2(z)$ and $a_1(z)$ this becomes

$$\begin{aligned} r_1(0) &= \frac{B - Ar}{Br + A} \\ &= \frac{(B/A) - r}{(B/A)r + 1}. \end{aligned} \tag{A.5}$$

Using the boundary condition

$$\begin{aligned} r_1(z) &= \frac{a_2(z)}{a_1(z)} \\ &= \frac{Be^{\gamma z} - Are^{-\gamma z}}{Bre^{\gamma z} + Ae^{-\gamma z}} \\ &= \frac{(B/A)e^{\gamma z} - re^{-\gamma z}}{(B/A)re^{\gamma z} + e^{-\gamma z}}. \end{aligned} \tag{A.6}$$

This results in

$$r_1(0) = \frac{(r + r_1(z))e^{-2\gamma z} + r(r_1(z) - 1)}{r(r + r_1(z))e^{-2\gamma z} + (1 - rr_1(z))} \tag{A.7}$$

A.3 Left Reflection Coefficient

Similarly, the left reflection coefficient can be written as

$$\begin{aligned} r_2(z) &= \frac{a_1(z)}{a_1(z)} \\ &= \frac{(B/A)re^{\gamma z} + e^{-\gamma z}}{(B/A)e^{\gamma z} - re^{-\gamma z}}. \end{aligned} \tag{A.8}$$

The boundary condition is

$$\begin{aligned} r_2(0) &= \frac{a_1(0)}{a_2(0)} \\ &= \frac{(B/A)r+1}{(B/A)-r}. \end{aligned} \tag{A.9}$$

This results in

$$r_2(z) = \frac{r(1+rr_2(0))+(r_2(0)-r)e^{-2\gamma z}}{(1+rr_2(0))+r(r-r_2(0))e^{-2\gamma z}} \tag{A.10}$$

A.4 Right Transmission Coefficient

The transmission coefficient to the right of any point inside the DFB cavity can be written as

$$\begin{aligned} t_1(0) &= \frac{a_1(z)}{a_1(0)} \\ &= \frac{(B/A)re^{\gamma z}+e^{-\gamma z}}{(B/A)+1}. \end{aligned} \tag{A.11}$$

The boundary condition is

$$r_1(z) = \frac{(B/A)e^{\gamma z}-re^{-\gamma z}}{(B/A)re^{\gamma z}+e^{-\gamma z}}. \tag{A.12}$$

This results in

$$t_1(0) = \frac{(r^2+1)e^{-\gamma z}}{(1-rr_1(z))+r(r+r_1(z))e^{-2\gamma z}}. \tag{A.13}$$

A.5 Left Transmission Coefficient

The transmission coefficient to the left of any point inside the DFB cavity can be written as

$$t_2(z) = \frac{a_2(0)}{a_2(z)}$$

$$= \frac{(B/A) - r}{(B/A)\, e^{\gamma z} - r e^{-\gamma z}}. \tag{A.14}$$

The boundary condition is

$$r_2(0) = \frac{(B/A)\, r + 1}{(B/A) - r}. \tag{A.15}$$

This results in

$$t_2(z) = \frac{(1 + r^2)\, e^{-\gamma z}}{(1 + r r_2(0)) + r\,(r - r_2(0))\, e^{-2\gamma z}}. \tag{A.16}$$

Appendix B

Derivation of Photon Rate Equation

For the derivation of the rate equations, two counter propagating waves in opposite directions will be considered. The photon flux density per angular frequency $P_{\omega,1}(z,t)$ for a wave propagating along the forward direction is introduced as:

$$P_{\omega,1} = B_1 a_1 a_1^* \tag{B.1}$$

where the proportionality B_1 is given as

$$B_1 = \left(\frac{\beta_1}{2\mu_o\omega}\right)\left(\frac{1}{\hbar\omega}\right). \tag{B.2}$$

The total photon flux density is the integral of $P_{n,\omega}(z,t)$ over the entire angular frequency range of interest:

$$P_n(z,t) = \int_\omega P_{n,\omega}(z,t)\, d\omega. \tag{B.3}$$

These equations were given earlier as (2.16), (2.17) and (2.18).

Considering only one forward and one backward moving fields, equation (2.11) can be written as:

$$\int_\omega \left[\frac{\partial a_1(z,t)}{\partial z} - \bar{\sigma}_{11} a_1(z,t) - \bar{\kappa}_{12} a_2(z,t) \quad + \quad \chi_{11}\frac{\partial a_1(z,t)}{\partial t} + \chi_{12}\frac{\partial a_2(z,t)}{\partial t}\right] d\omega$$

$$= \int_\omega \zeta_1(z,t)\,d\omega \tag{B.4}$$

$$\int_\omega \left[\frac{\partial a_2(z,t)}{\partial z} - \bar{\sigma}_{22}a_2(z,t) - \bar{\kappa}_{21}a_2(z,t) + \chi_{22}\frac{\partial a_2(z,t)}{\partial t} + \chi_{21}\frac{\partial a_1(z,t)}{\partial t}\right] d\omega$$

$$= \int_\omega \zeta_2(z,t)\,d\omega. \tag{B.5}$$

From the above two equations and their complex conjugates, the following expression can be obtained:

$$\frac{d(P_1(z,t) - P_2(z,t))}{dz} - 2\bar{\sigma}_{11}(P_1(z,t) + P_2(z,t)) + \chi_{11}\frac{d(P_1(z,t) + P_2(z,t))}{dt}$$
$$= |B_1|\,K_{tr}\int_\omega \left[\zeta_1(z,t)\,a_2^*(z,t) + \zeta_2^*(z,t)\,a_1(z,t)\right] d\omega. \tag{B.6}$$

K_{tr} in the above expression is the Petermann factor for the transverse mode. This takes into account the enhanced spontaneous emission that arises as a result of the non-orthogonality of complex transverse modes. This can be written as [103]

$$K_{tr} = \frac{\int_x \int_y E(x,y)\,E^*(x,y)\,dy\,dx}{\int_x \int_y E(x,y)\,E(x,y)\,dy\,dx}. \tag{B.7}$$

The right side of equation (B.6) can be interpreted as the total spontaneous emission power coupled into the transverse mode R_{sp}. The resulting equation (B.8) is the rate equation for photons. This describes the dynamics of photons as a result of their interaction with the carriers, and can also be interpreted as a statement of power conservation. From the current continuity relation, the carrier rate equation (B.9) can be derived by neglecting the drift current term. These are:

$$\frac{1}{v}\frac{d(P_1 - P_2)}{dt} = g(n)(P_1 + P_2) + R_{sp}(n) + \frac{\partial(P_1 - P_2)}{\partial z} \tag{B.8}$$

$$\frac{dn}{dt} = G - R_n(n) - g(n)(P_1 + P_2) + \frac{1}{q}\nabla \cdot J. \tag{B.9}$$

P_1 and P_2 are the photon flux per unit area, n is the carrier density, v is the velocity term. G is the volume injection rate, R_{sp} is the spontaneous emission rate into that transverse mode, R_n is the total recombination rate. J is the current density and $g(n)$ is the optical gain function.

Bibliography

[1] I. Jacobs, "Lightwave Systems Develpoment: Looking Back and Ahead," *Optics and Photonics News*, pp. 19–23, February 1995.

[2] G. P. Agrawal, *Fiber-Optic Communication Systems*. Wiley Series in Microwave and Optical Engineering, John Wiley & Sons, Inc., 1992.

[3] C. A. Brackett, "Dense Wavelength Division Multiplexing Networks: Principles and Applications," *IEEE Journal on Selected Area in Communications*, vol. 8, no. 6, pp. 948–964, 1990.

[4] T. Makino, "Effective-Index Matrix Analysis of Distributed Feedback Semiconductor Lasers," *IEEE Journal of Quantum Electronics*, vol. 28, no. 2, pp. 434–440, 1992.

[5] T. Makino, H. Lu, and G. Li, "Transfer-Matrix Dynamic Model of Partly Gain-Coupled 1.55 μm DFB Lasers with a Strained-Layer MQW Active Grating," *IEEE Journal of Quantum Electronics*, vol. 30, no. 11, pp. 2443–2447, 1994.

[6] T. Makino, "Threshold Condition of DFB Semiconductor Lasers by the Local-Normal-Mode Transfer-Matrix Method: Correspondence to the Coupled-

Wave Method," *IEEE Journal of Lightwave Technology*, vol. 12, no. 12, pp. 2092–2099, 1994.

[7] T. Makino and J. Glinksi. "Transfer-Matrix Analysis of the Amplified Spontaneous Emission of DFB Semiconductor Laser Amplifiers," *IEEE Journal of Quantum Electronics*, vol. 24, no. 8, pp. 1507–1518, 1988.

[8] S. Hansmann, "Transfer Matrix Analysis of the Spectral Properties of Complex Coupled Distributed Feedback Laser Structures," *IEEE Journal of Quantum Electronics*, vol. 28, no. 11, pp. 2589–2595, 1992.

[9] S. Hansmann, H. Walter, H. Hillmer, and H. Burkhard, "Static and Dynamic Properties of InGaAsP-InP Distributed Feedback Lasers - A Detailed Comparison Between Experiment and Theory," *IEEE Journal of Quantum Electronics*, vol. 30, no. 11, pp. 2477–2484, 1994.

[10] H. Soda, Y. Kotaki, H. Sudo, H. Ishikawa, S. Yamakoshi, and H. Imai, "Stability in Single Longitudinal Mode Operation in GaInAsP/InP Phase-Adjusted DFB Lasers," *IEEE Journal of Quantum Electronics*, vol. 23, no. 6, pp. 804–814. 1987.

[11] H. Soda and H. Imai, "Analysis of the Spectrum Behaviour Below the Tthreshold in DFB Lasers," *IEEE Journal of Quantum Electronics*, vol. 22, no. 5, pp. 637–641, 1986.

[12] G. P. Agrawal and A. H. Bobeck, "Modeling of Distributed Feedback Semiconductor Lasers with Axially-Varying Parameters," *IEEE Journal of Quantum Electronics*, vol. 24, no. 12, pp. 2407–2414. 1988.

[13] G. P. Agrawal, "Effect of Gain and Index Nonlinearities on Single-Mode Dynamics in Semiconductor Lasers," *IEEE Journal of Quantum Electronics*, vol. 26, no. 11, pp. 1901–1909, 1990.

[14] G. P. Agrawal, "Gain Nonlinearities in Semiconductor Lasers: Theory and Application to Distributed Feedback Lasers," *IEEE Journal of Quantum Electronics*, vol. 23, no. 6, pp. 860–868, 1987.

[15] J. E. Whiteaway, G. Thompson, A. J. Collar, and C. J. Armistead, "The Design and Assessment of $\lambda/4$ Phase-Shifted DFB Laser Structures," *IEEE Journal of Quantum Electronics*, vol. 25, no. 6, pp. 1261–1279, 1989.

[16] A. Lowery, A. Keating, and C. N. Murtonen, "Modeling the Static and Dynamic Behaviour of Quarter-Wave-Shifted DFB Lasers," *IEEE Journal of Quantum Electronics*, vol. 28, no. 9, pp. 1874–1883, 1992.

[17] P. Vankwikelberge, G. Morthier, and R. Baets, "CLADISS - A Longitudinal Multimode Model for the Analysis of the Static, Dynamic, and Stochastic Behaviour of Diode Lasers with Distributed Feedback," *IEEE Journal of Quantum Electronics*, vol. 26, no. 10, pp. 1728–1741, 1990.

[18] K. David, J. Buus, and R. G. Baets, "Basic Analysis of AR-Coated, Partly Gain-Coupled DFB Lasers: The Standing Wave Effect," *IEEE Journal of Quantum Electronics*, vol. 28, no. 2, pp. 427–433, 1992.

[19] COST 240 Group, "Comparison of different DFB laser models within the European COST 240 collaboration," *IEE Proceedings in Optoelectronics*, vol. 141, no. 2, pp. 82–88, 1994.

[20] L. Zhang and J. E. Carrol, "Large-Signal Dynamic Model of the DFB Laser," *IEEE Journal of Quantum Electronics*, vol. 28, no. 3, pp. 604–611, 1992.

[21] C. Tsang, D. Marcenac, J. Carrol, and L. Zhang, "Comparison between power matrix model and time domain model in modelling large signal responses of DFB lasers," *IEE Proceedings in Optoelectronics*, vol. 141, no. 2, pp. 89–96, 1992.

[22] L. Zhang, J. E. Carrol, and J. Whiteaway, "Dynamics and hole burning in uniform DFB semiconductor lasers," *International Journal of Optoelectronics*, vol. 8, no. 3, pp. 279–291, 1993.

[23] L. Zhang, S. Yu, M. Nowell, D. Marcenac, J. Carrol, and R. Plumb, "Dynamic Analysis of Radiation and Side-Mode Suppression in a Second-Order DFB Laser Using Time-Domain Large-Signal Traveling Wave Model," *IEEE Journal of Quantum Electronics*, vol. 30, no. 6, pp. 1389–1395, 1994.

[24] A. J. Lowery, "Transmission-Line Modelling of Semiconductor Lasers: The Transmission-Line Laser Model," *International Journal of Numerical Modelling*, vol. 2, pp. 249–265, 1989.

[25] A. J. Lowery, "A Two-Port Bilateral Model for Semiconductor Laasers," *IEEE Journal of Quantum Electronics*, vol. 28, no. 1, pp. 82–92, 1992.

[26] A. Lowery, "Dynamic Modelling of Distributed-Feedback Lasers Using Scattering Matrices," *Electronics Letters*, vol. 25, no. 19, pp. 1307–1308, 1989.

[27] A. Lowery, "Comparison between two recent large-signal dynamic DFB laser models," *IEE Proceedings*, vol. 139, no. 6, pp. 402–406, 1992.

[28] B. Jonsson, A. J. Lowery, H. Olesen, and B. Tromborg, "Instabilities and Nonlinear L-I Characteristics in Complex-Coupled DFB Lasers with Antiphase Gain and Index Gratings," *IEEE Journal of Quantum Electronics*, vol. 32, no. 5, pp. 839–850, 1996.

[29] A. J. Lowery and D. Novak, "Performance Comparison of Gain-Coupled and Index-Coupled DFB Semiconductor Lasers," *IEEE Journal of Quantum Electronics*, vol. 30, no. 9, pp. 2051–2063, 1994.

[30] B. Tromborg, H. E. Lassen, and H. Olesen. "Traveling Wave Analysis of Semiconductor Lasers: Modulation Responses. Mode Stability and Quantum Mechanical Treatment of Noise Spectra," *IEEE Journal of Quantum Electronics*. vol. 30, no. 4, pp. 939–956, 1994.

[31] B. Tromborg, H. Olesen, X. Pan, and S. Saito. "Transmission Line Description of Optical Feedback and Injection Locking for Fabry-Perot and DFB Lasers," *IEEE Journal of Quantum Electronics*, vol. 23, no. 11, pp. 1875–1889, 1987.

[32] H. Kogelnik and C. Shank, "Coupled-Wave Theory of Distributed Feedback Lasers," *Journal of Applied Physics*, vol. 43. no. 5, pp. 2327–2335, 1972.

[33] K. Aiki, M. Nakamura, and J. Umeda, "A Frequency-Multiplexing Light Source with Monolithically Integrated Distributed-Feedback Diode Lasers," *IEEE Journal of Quantum Electronics*, vol. QE-13, no. 4, pp. 220–223, 1977.

[34] L. Miller, K. Beernink, J. Hughes, S. Bishop, and J. Coleman, "Four wavelength distributed feedback ridge waveguide quantum-well heterostructure laser array," *Applied Physics Letters*. vol. 61, no. 25, pp. 2964–2966, 1992.

[35] C. Zah, F. Faivre, B. Pathak, R. Bhat, C. Caneau, P. Lin, A.S.Gozdz, N. Andreadakis, M. Koza, and T. Lee, "Monolithic Integration of Multiwavelength Compressive-Strained Multiquantum-Well Distributed-Feedback Laser Array with Star Coupler and Optical Amplifier," *Electronics Letters*, vol. 28, no. 25, pp. 2361–2362. 1992.

[36] J.-M. Verdiell, T. Koch, D. Tennant. K. Feder, R. Gnall, M. Young, B. Miller, U. Koren, M. Newkirk, and B. Tell, "8-Wavelength DBR Laser Array Fabricated with a Single-Step Bragg Grating Printing Technique," *IEEE Photonics Technology Letters*, vol. 5, no. 6, pp. 619–621, 1993.

[37] D. Tennant. K. Feder, K. Dreyer, R. Gnall, T. Koch, U. Koren, and M. Young, "Phase Grating Masks for Photonic Circuits Fabricated by E-Beam Writing and Dry Etching: Challenges to Commercial Applications," *Microelectronic Engineering*, vol. 27, pp. 427–434, 1995.

[38] G. Pakulski, R. Moore, C. Maritan, and F. Shepherd, "Fused silica masks for printing uniform and phase adjusted gratings for distributed feedback lasers," *Applied Physics Letters*, vol. 62, no. 3, pp. 222–224, 1993.

[39] T. Cockerill, R. Lammert, D. Forbes, M. Osowski, and J. Coleman, "Twelve-Channel Strained-Layer InGaAs-GaAs-AlGaAs Buried Heterostructure Quantum Well Laser Array for WDM Applications by Selective-Area MOCVD," *IEEE Photonics Technology Letters*, vol. 6, no. 7, pp. 786–788, 1994.

[40] C. Joyner, M. Zirngibl, and J. Meester. "A Multifrequency Waveguide Grating Laser by Selective Area Epitaxy," *IEEE Photonics Technology Letters*, vol. 6, no. 11, pp. 1277–1279, 1994.

[41] M. Aoki, T. Taniwatari, M. Suzuki, and T. Tsutsui, "Detuning Adjustable Multiwavelength MQW-DFB Laser Array Grown by Effective Index/Quantum Energy Control Selective Area MOVPE," *IEEE Photonics Technology Letters*, vol. 6, no. 7, pp. 789–791, 1994.

[42] M. Nakao, K. Sato, Toshio, Nishida, and T. Tamamura, "Distributed Feedback Laser Arrays Fabricated by Synchronous Orbital Radiation Lithography," *IEEE Journal on Selected Areas in Communications*, vol. 8, no. 6, pp. 1178–1182, 1990.

[43] G. Coudenys, I. Moerman, Y. Zhu, P. V. Daele, and P. Demeester, "Multiwavelength InGaAs/InGaAsP Strained-Layer MQW-Laser Array Using Shadow-Masked Growth," *IEEE Photonics Technology Letters*, vol. 4, no. 6, pp. 524–526, 1992.

[44] B. Ooi, S. Ayling, A. Bryce, and J. Marsh, "Fabrication of Multiple Wavelength Lasers in GaAs-AlGaAs Structures Using a One-Step Spatially Controlled Quantum-Well Intermixing Technique," *IEEE Photonics Technology Letters*, vol. 7, no. 9, pp. 944–946, 1995.

[45] K. R. Poguntke, J. Soole, A. Scherer, H. LeBlanc, C. Caneau, and R. Bhat, "Simultaneous multiple wavelength operation of a multistripe array grating integrated cavity laser," *Applied Physics Letters*, vol. 62, no. 17, pp. 2024–2026, 1993.

[46] J. Soole, K. Poguntke, A. Scherer, H. LeBlanc, and C. Chang-Hasnain, "Wavelength-selectable laser emission from a multistripe array grating integrated cavity laser," *Applied Physics Letters*, vol. 61, no. 23, pp. 2750–2752, 1992.

[47] S. Sakano, T. Tsuchiya, M. Suzuki, S. Kitajima, and N. Chinone, "Tunable DFB Laser with Striped Thin-Film Heater," *IEEE Photonics Technology Letters*, vol. 4, no. 4, pp. 321–323, 1992.

[48] S. Woodward, U. Koren, B. Miller, M. Young, M. Newkirk, and C. Burrus, "A DBR Laser Tunable by Resistive Heating," *IEEE Photonics Technology Letters*, vol. 4, no. 12, pp. 1330–1332, 1992.

[49] W. Tsang, R. Kapre, R. Logan, and T. Tanbun-Ek, "Control of Lasing Wavelength in Distributed Feedback Lasers by Angling the Active Stripe with Respect to the Grating," *IEEE Photonics Technology Letters*, vol. 5, no. 9, pp. 978–980, 1993.

[50] H. Luo and P. Zory, "Distributed Feedback Coupling Coefficient in Diode Lasers with Metallized Gratings," *IEEE Photonics Technology Letters*, vol. 2, no. 9, pp. 614–616, 1990.

[51] A. Rast, T. Johannes, W. Harth, and G. Franz, "New complex-coupled DFB-laser with a contacted surface grating for $\lambda = 1.55\mu$m," *IEE Proceedings in Optoelectronics*, vol. 142, no. 3, pp. 162–164, 1995.

[52] R. Martin, S. Forouhar, S. Keo, R. Lang, R. Hunsperger, R. Tiberio, and P. Chapman, "CW Performance of an InGaAs-GaAs-AlGaAs Laterally-Coupled Distributed Feedback Laser Diode," *IEEE Photonics Technology Letters*, vol. 7, no. 3, pp. 244–246, 1995.

[53] C. Kazmierski, D. Robein, D. Mathoorasing, A. Ougazzaden, and M. Filoche, "1.5-μm DFB Lasers with New Current-Induced Gain Gratings," *IEEE Journal on Selected Topics in Quantum Electronics*, vol. 1, no. 2, pp. 371–374, 1995.

[54] G. Li, T. Makino, and H. Lu, "Simulation and Interpretation of Longitudinal-Mode Behaviour in Partly Gain-Coupled InGaAsP/InP Multiquantum-Well

DFB Lasers," *IEEE Photonics Technology Letters*, vol. 4, no. 4, pp. 386–389, 1993.

[55] G. Li, T. Makino, and C. Wu, "Multi-λ ridge waveguide gain-coupled DFB laser array," *IEEE Journal of Lightwave Technology*, vol. 13, no. 2, pp. 196–199, 1995.

[56] H. Lu, B. Benyon, G. P. Li, and T. Makino, "High-Power and High-Speed Performance of 1.3-μm Strained MQW Gain-Coupled DFB Lasers," *IEEE Journal of Selected Topics in Quantum Electronics*, vol. 1, no. 2, pp. 375–381, 1995.

[57] H. Lu, G. Li, and T. Makino, "High-Speed Performance of Gain-Coupled 1.55-μm Strained-Layer Multiple-Quantum-Well DFB Lasers," *IEEE Photonics Technology Letters*, vol. 5, no. 8, pp. 861–863, 1993.

[58] T. Makino and H. Lu, "Wide temperature-range singlemode operation of MQW gain-coupled DFB lasers," *Electronics Letters*, vol. 30, no. 23, pp. 1948–1950, 1994.

[59] H. Lu, T. Makino, and G. P. Li, "Dynamic Properties of Partly Gain-Coupled 1.55-μm DFB Lasers," *IEEE Journal of Quantum Electronics*, vol. 31, no. 8, pp. 1443–1450, 1995.

[60] H. Lu, C. Blaauw, and T. Makino, "High-Temperature Single-Mode Operation of 1.3-μm Strained MQW Gain-Coupled DFB Lasers," *IEEE Photonics Technology Letters*, vol. 7, no. 6, pp. 611–613, 1995.

[61] A. Sarangan, W. Huang, G. Li, and T. Makino, "A Ridge Waveguide DFB Laser Model Including Transverse Carrier and Optical Effects," *IEEE Journal of Quantum Electronics*, vol. 32, no. 3, pp. 408–416, 1996.

[62] A. Sarangan, C. Xu, W. Huang, G. Li, C. Wu, and T. Makino, "Analysis of Multi-Wavelength DFB Laser Arrays with Different Ridge Widths," *OSA Integrated Photonics Research Conference*, pp. 187–189, 1995.

[63] A. Sarangan, W. Huang, G. Li, and T. Makino, "Three Dimensional Analysis of Multi-Wavelength DFB Laser Arrays," *SPIE Photonics West (Invited Paper)*, 1996.

[64] G. Li, T. Makino, A. Sarangan, and W. Huang, "Multi-Wavelength Gain-Coupled Distributed Feedback Laser Arrays with Fine Tunability," *U.S. Patent No. 5536085*, Northern Telecom Ltd., Issued on July 16 1996.

[65] G. Li, T. Makino, A. Sarangan, and W. Huang, "16-Wavelength Gain-Coupled DFB Laser Array with Fine Tunability," *IEEE Photonics Technology Letters*, vol. 8, no. 1, pp. 22–24, 1996.

[66] A. Sarangan, W. Huang, T. Makino, and G. Li, "Wavelength Control in DFB Laser Arrays by Tilting the Ridge Width Respect to the Gratings," *IEEE Photonics Technology Letters*. To appear in November 1996.

[67] A. Sarangan, W. Huang, T. Makino, and G. Li, "Selection of Transverse Oscillation Modes in Tilted Ridge DFB Lasers," *IEEE Journal of Lightwave Technology*, vol. 14, no. 8, pp. 1853–1858, 1996.

[68] A. Sarangan, W. Huang, T. Makino, and G. Li, "Dynamic Single Transverse Mode Properties of Varying Ridge Width DFB Laser Arrays," *IEEE Photonics Technology Letters*, vol. 8, no. 10, pp. 1305–1307, 1996.

[69] A. Sarangan, W. Huang, T. Makino, and G. Li, "The Effect of Tilt on the Spectral Properties of Ridge Waveguide DFB Lasers," *IEEE Journal of Lightwave Technology*, Submitted in 1996.

[70] D. Marcuse, *Theory of Dielectric Optical Waveguides.* Academic Press, Inc., 1991.

[71] W. Streifer, D. R. Scifres, and R. D. Burnham, "Coupling Coefficients for Distributed Feedback Single- and Double-Heterostructure Diode Lasers," *IEEE Journal of Quantum Electronics*, vol. 11, no. 11, pp. 867–873, 1975.

[72] T. Makino. "Analytical Formulas for the Optical Gain of Quantum Well Lasers," *IEEE Journal of Quantum Electronics*, vol. 32, no. 3, pp. 493–501, 1996.

[73] T. A. DeTemple and C. M. Herzinger, "On the Semiconductor Laser Logarithmic Gain-Current Density Relation," *IEEE Journal of Quantum ELectronics*, vol. 29, no. 5, pp. 1246–1252, 1993.

[74] J. Whiteaway, G. Thompson, P. Greene, and R. Glew, "Logarithmic Gain/Current-Density Characteristic of InGaAs/InGaAlAs/InP Multi-Quantum-Well Separate-Confinement-Heterostructure Lasers," *Electronics Letters*, vol. 27, no. 4, pp. 340–342, 1991.

[75] P. Morton, D. Ackerman, G. Shtengel, R. Kazarinov, M. Hybertsen, T. Tanbun-Ek, R. Logan, and A. Sergent, "Gain Characteristics of 1.55-μm High-Speed Multiple-Quantum-Well Lasers," *IEEE Photonics Technology Letters*, vol. 7, no. 8, pp. 833–835, 1995.

[76] T.-A. Ma, Z.-M. Li, T. Makino, and M. Wartak, "Approximate Optical Gain Formulas for 1.55-μm Strained Quarternary Quantum-Well Lasers," *IEEE Journal of Quantum Electronics*, vol. 31, no. 1, pp. 29–34, 1995.

[77] B. R. Bennett, R. A. Soref, and J. A. D. Alamo, "Carrier-Induced Change in Refractive Index of InP, GaAs and InGaAsP," *IEEE Journal of Quantum Electronics*, vol. 26, no. 1, pp. 113–122, 1990.

[78] B. Broberg and S. Lindgren, "Refractive index of $In_{1-x}Ga_xAs_yP_{1-y}$ layers and InP in the transparent wavelength region," *Journal of Applied Physics*, vol. 55, no. 9, pp. 3376–3381, 1984.

[79] G. Li, T. Makino, R. Moore, and N. Puetz, "1.55μm Index/Gain Coupled DFB Lasers with Strained Layer Multiquantum-Well Active Grating," *Electronics Letters*, vol. 28, no. 18, pp. 1726–1727, 1992.

[80] W. Tsang, M. W. F.S. Choa, Y. Chen, R. Logan, and S. Chu, "Semiconductor distributed feedback lasers with quantum well or superlattice gratings for index or gain-coupled optical feedback," *Applied Physics Letters*, vol. 60, no. 21, pp. 2580–2583, 1992.

[81] E. Kapon, A. Hardy, and A. Katzir. "The Effect of Complex Coupling Coefficients on Distributed Feedback Lasers," *IEEE Journal of Quantum Electronics*, vol. 18, no. 1, pp. 66–71, 1982.

[82] A. Champagne, R. Maciejko, and T. Makino, "Enhanced Carrier Injection Efficiency from Lateral Current Injection in Mulitple-Qauntum-Well DFB Lasers," *IEEE Photonics Technoloyg Letters*, vol. 8, no. 8, pp. 749–751, 1996.

[83] J. Hamasaki and T. Iwashima, "A Single-Wavelength DFB Structure with a Synchronized Gain Profile," *IEEE Journal of Quantum Electronics*, vol. 24, no. 9, pp. 1864–1872, 1988.

[84] D. Adams and T. Makino, "Mechanism for enhanced gain-periodicity in truncated-well gain-coupled DFB lasers," *Electronics Letters*, vol. 31, no. 12, pp. 976–977, 1995.

[85] M. Stern. *Finite Difference Analysis of Planar Optical Waveguides - Methods for Modelling and Simulation of Guided-Wave Optoelectronic Devices*, vol. 10 of *Progress in Electromagnetic Research*. EMW Publishing, 1995.

[86] L. Davis, Y. Lam, D. Nichols, J. Singh, and P. Bhattacharya, "Auger Recombination Rates in Compressively Strained $In_xGa_{1-x}As/InGaAsP/InP$ ($0.53 \leq x \leq 0.73$) Multiquantum Well Lasers," *IEEE Photonics Technology Letters*, vol. 5, no. 2, pp. 120–122, 1995.

[87] A. Haug, "Auger recombination in InGaAsP," *Applied Physics Letters*, vol. 42, no. 6, pp. 512–514, 1983.

[88] A. Sugimura, "Band-to-band Auger recombination in InAsAsP lasers," *Applied Physics Letters*, vol. 39, no. 1, pp. 21–23, 1981.

[89] R. Olshanksy, C. Su, J. Manning, and W. Powazinik, "Measurement of Radiative and Nonradiative Recombination Rates in InGaAsP and AlGaAs Light Sources," *IEEE Journal of Quantum Electronics*, vol. 20, no. 8, pp. 838–854, 1984.

[90] S. Hu, D. Young, A. Gossard, and L. Coldren, "The Effect of Lateral Leakage Current on the Experimental Gain/Current-Density Curve in Quantum-Well Ridge-Waveguide Lasers," *IEEE Journal of Quantum Electronics*, vol. 30, no. 10, pp. 2245–2250, 1994.

[91] J. C. Cartledge and A. F. Elrefaie, "Threshold Gain Difference Requirements for Nearly Single-Longitudinal -Mode Lasers," *IEEE Journal of Lightwave Technology*, vol. 8, no. 5, pp. 704–715, 1990.

[92] J. C. Cartledge, "On the Probabilistic Characterization of Side Mode Fluctutations in Pulse-Modulated Nearly-Single-Mode Semiconductor Lasers," *IEEE Journal of Quantum Electronics*, vol. 26, no. 12, pp. 2046–2051, 1990.

[93] S. Miller, "On the Prediction of the Mode-Partitioning Floor in Injection Lasers with Multiple Side Modes at 2 and 10 gb/s," *IEEE Journal of Quantum Electronics*, vol. 26, no. 2, pp. 242–249, 1990.

[94] Driver circuits were provided courtesy of Communications Research Center, Ottawa, Ontario, Canada.

[95] Custom made from Photonic Integration Research, Inc., Columbus, Ohio, U.S.A.

[96] M. D. Forte, M. Papuchon, C. Puech, P. Lallemand, and D. Ostrowsky, "Tunable Optically Pumped GaAs-GaAlAs Distributed-Feedback Lasers," *IEEE Journal of Quantum Electronics*, vol. 14, no. 9, pp. 560–562, 1978.

[97] W. Streifer and A. Hardy, "Analysis of Two-Dimensional Waveguides with Misaligned or Curved Gratings," *IEEE Journal of Quantum Electronics*, vol. 14, no. 12, pp. 935–943, 1978.

[98] A. Hardy and W. Streifer, "Analysis of waveguided Gaussian beams coupled by misaligned or curved gratings," *Journal of the Optical Society of America*, vol. 69, no. 9, pp. 1235–1242, 1979.

[99] H. Hillmer, K. Magari, and Y. Suzuki, "Chirped Gratings for DFB Laser Diodes Using Bent Waveguides," *IEEE Photonics Technology Letters*, vol. 5, no. 1, pp. 10–12, 1993.

[100] H. Hillmer, A. Grabmaier, S. Hansmann, H.-L. Zhu, H. Burkhard, and K. Magari, "Tailored DFB Laser Properties by Individually Chirped Gratings Using Bent Waveguides," *IEEE Journal on Selected Topics in Quantum Electronics*, vol. 1, no. 2, pp. 356–362, 1995.

[101] H. Hillmer, A. Grabmaier, H.-L. Zhu, S. Hansmann, and H. Burkhard, "Continously Chirped DFB Gratings by Specially Bent Waveguides for Tunable Lasers," *IEEE Journal of Lightwave Technology*, vol. 13, no. 9, pp. 1905–1912, 1995.

[102] T. Schrans and A. Yariv, "Semiconductor lasers with uniform longitudinal intensity distribution," *Applied Physics Letters*, vol. 56, no. 16, pp. 1526–1528, 1990.

[103] K. Petermann, "Calculated Spontaneous Emission Factor for Double-Heterostructure Injection Lasers with Gain-Induced Waveguiding," *IEEE Journal of Quantum Electronics*, vol. 15, no. 7, pp. 566–570, 1979.